Resonant photonic crystal photodetectors for the infrared in silicon

by

Karan K. Mehta

B.S., University of California, Los Angeles (2010)

Submitted to the Department of Electrical Engineering
in partial fulfillment of the requirements for the degree of

Masters of Science in Electrical Engineering

at the

MASSACHUSETTS INSTITUTE OF TECHNOLOGY

September 2012

Author . . . . . .
Department of Electrical Engineering
August 31, 2012

Certified by . . . . . .
Rajeev J. Ram
Professor of Electrical Engineering
Thesis Supervisor

Accepted by . . . . . .
Leslie Kolodziejski
Chairman, Department Committee on Graduate Students

Resonant photonic crystal photodetectors for the infrared in silicon

by

Karan K. Mehta

Submitted to the Department of Electrical Engineering
on August 31, 2012, in partial fulfillment of the
requirements for the degree of
Masters of Science in Electrical Engineering

Abstract

The challenge of overcoming energy efficiency and bandwidth limitations in interconnects between components in computer systems (e.g. between memory and processors) has motivated the development of short-range optical interconnects, which in many approaches require optical devices and waveguides fabricated within the same CMOS environments as the electronics. This thesis centers on developing photodetectors for infrared light within the silicon of commercial CMOS processes; silicon's lack of strong absorption at the wavelengths of interest makes this challenging.

The approach uses defect-state mediated linear absorption and two-photon absorption (TPA) in small mode-volume resonators to generate photocarriers. Such resonators allow efficient linear absorption in short devices despite low absorption coefficients, and a greater TPA rate than in bulk material due to the large energy densities achievable. The devices here are made in the polysilicon layer of a commercial DRAM process, and characterization of this material, different from crystalline Si in both its linear and nonlinear absorption, forms a starting point. The design, fabrication, and testing of electrically addressable photonic crystal resonators subject to the constraints associated with working in a CMOS process are then presented.

The best resonators made were able to reach Qs of 70,000, limited by linear loss in the polysilicon. Linear absorption is dominant in the devices made to date, and allowed quantum efficiencies of a few tens of percent on resonance. However, high biases of around -20 V were required to achieve these QEs, and the bandwidth of the devices was limited to only approximately 500 MHz. Improvements to the electrical structure of the devices are likely to improve these characteristics. The ability to fabricate high-Q photonic crystal resonators within full CMOS flows, and the QEs allowed by defect-assisted absorption in the devices measured, indicate promise for this approach to photodetection in integrated CMOS photonic systems.

Thesis Supervisor: Rajeev J. Ram
Title: Professor of Electrical Engineering

Acknowledgments

A great thanks to Rajeev Ram for giving me the opportunity to do this work, and encouraging me to think about different directions freely. His generosity with his time and knowledge have been a huge help to me, and the sum of all I've learned from conversations with him over the last two years is tremendous.

Jason Orcutt helped me begin in the group and I'm fortunate to have been able to learn many aspects of device testing and design from him, not to mention all the conversations that benefit from his knowledge and understanding of many things (which it turns out include optics and electronics). This work would have been impossible without what he did as a graduate student. From Parthiban Santhanam I've learned a lot about science, life in general, and much else. Our office would be a far duller place without his enthusiasm and willingness to sound out and bounce around ideas (and also every variety of irrelevancy). All of the friends I've been fortunate to make since coming to Boston, including many other members of the group, have livened these good past two years.

My mother and father's love and support are endlessly meaningful, and I feel a huge gratitude towards them. My brother Kunal is a friend I am truly lucky to have.

Contents

List of Figures

Chapter 1

Introduction

The field of integrated optics has seen dramatic progress in the decades since its inception in the 1960s; what began as a field in which the observation of a guided mode in a slab could comprise the bulk of a doctoral dissertation [Yar84] has advanced to the point that it seems one now has to do more to graduate. From most points of view this is a good thing.

This thesis concerns a particular class of devices in a platform for on-chip manipulation of light in a manner that can be intimately integrated with silicon electronics in scaled CMOS processes. In particular, here we attempt to develop photodetectors that absorb photons and generate electron-hole pairs, thus converting an optical signal into an electrical one, purely in silicon itself. Due to silicon's transparency at the wavelengths of interest, this presents a challenge, as the photons are of lower energy than the bandgap. In this work we study devices aiming to use both defect-assisted linear absorption and nonlinear two-photon absorption (TPA) to produce free photocarriers. TPA occurs increasingly efficiently for increasing light intensity, and so the devices developed here make use of small, low-loss resonators in photonic crystals to achieve high energy densities for low input powers.

This chapter presents first a short history and overview of the field, followed by some more specific discussion of the kind of devices considered here, previous work done of a similar kind, and the relevant physical background.

1.1 Some history of integrated optics

The idea of integrating optical functionalities with semiconductor devices took root in early investigations of GaAs lasers in the early 60s at Bell Laboratories, when the p-n junctions in the laser diodes were observed to give rise to a guided optical slab mode [BCLY63]. Much of the initial work in the next few years focused on waveguiding in thin films [Hal70], but the understanding of the potential for optical guiding, modulation [HYG70], and gain in materials in which electronic devices could be made in close proximity quickly led to a number of studies integrating lasers, transistors, detectors, and control electronics; the term "integrated optics" already referred to a rich field by the early 1970s [Tie71].

This early work focused primarily on III-V semiconductors like GaAs and InP; only later did silicon attract interest in integrated optics. The primary reasons to ignore silicon for integrated optics early on were that its indirect bandgap precludes optical gain, and the inversion symmetry of its crystal structure leads to a vanishing second-order nonlinearity and thus no opportunity for electro-optic modulation based on the Pockels effect, as was employed in $LiNbO_3$ and III-V semiconductor-based modulators at the time. But the rapidly growing sophistication of silicon processing and its dominance in electronics by the 80s gave incentive to try to work around these issues. Guiding of light in crystalline silicon was reported in the mid-80s by Soref [SL85], who also was the first to study free carrier-induced plasma dispersion as a potential mechanism for electro-optic modulation [SL86, SB87]; the potential uses of chips capable of modulating, routing and detecting light even in the absence of gain motivated much work developing this basic concept for modulation, and through the 90s various device geometries were devised to achieve this. Such devices in this period used carrier injection into straight waveguides, and for adequate phase shifts tended to require millimeter device lengths [TRWR94, CISZ97].

A path to reducing the size of these devices grew out of work in the late 90s, when Brent Little and colleagues at MIT studied devices based on microring resonators and proposed to use them as compact building blocks for integrated photonic

systems, initially as filters for wavelength division multiplexing (WDM) applications [LCH+97]. From one perspective their compactness and simplicity of design and analysis made them an appealing universal building block for large-scale optical systems [LC00]. These resonator designs, with their Qs of many tens to hundreds of thousands, provided electro-optic dispersions orders of magnitude larger per unit length than straight waveguides; their combination with active modulator geometries was a significant step forward in the last decade, resulting in drastically more compact modulators [XSPL05]. The last few years have seen much further refinement of the design of both modulators and detectors (to be discussed in more detail below), along with significant efforts to move beyond research on individual devices and towards system-scale testbeds and implementations in scaled CMOS processes [OR10], [OKH+11], [BJO+09].

A variety of insights and inventions, along with the continued development of silicon foundry capabilities, has brought integrated optics to the point where sophisticated silicon chips with thousands of resonators, low-loss waveguides, modulators, and detectors have become possible. In the last decade or so, the development of small-scale, high-Q resonators in silicon has been an important driving force towards more efficient and compact devices. These have been ring resonators, most commonly; development of photonic crystal resonators, which can achieve still smaller volumes, began approximately contemporaneously with that of microrings, but continued work and refinement of designs for photonic crystal resonators have made them increasingly attractive since. The work leading to them as a technology potentially relevant to silicon photonics systems is reviewed in the next section.

1.2 Photonic crystal devices and resonators

Periodic structures have long been employed in integrated optics [YN77], most commonly to achieve distributed-feedback mirrors for filters and lasers, along with gratings to couple light from free-space propagating to guided modes; photonic crystal ideas applied to integrated optics can thus be seen as a generalization of an old trend.

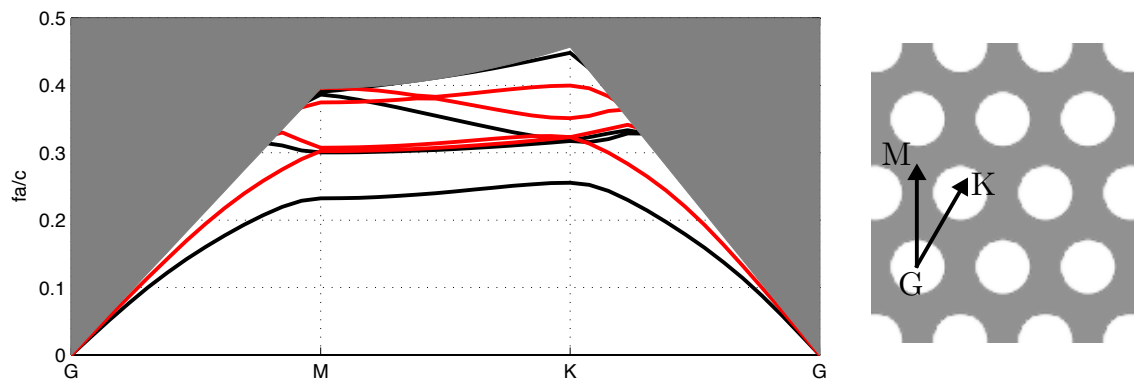

Figure 1-1: Example bandstructure of a silicon slab ($n = 3.5$) with an oxide cladding ($n = 1.46$), with holes with radius $0.3a$ arranged in a 2D triangular lattice, and a slab thickness of $0.5a$; TE-like bands are shown in black and TM-like in red. A bandgap exists for TE-like modes between normalized frequencies of 0.25 and 0.3. Points above the lightline of the oxide cladding corresponding to leaky modes are shaded in gray. A view of the triangular lattice is shown on the right, with the directions of the relevant points in k-space suaperposed.

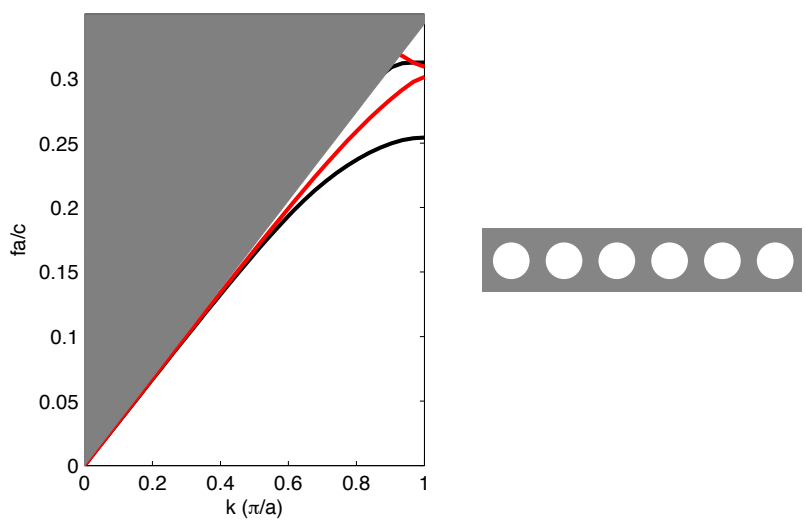

Figure 1-2: Example bandstructure of a silicon strip waveguide with a linear array of holes, as shown on the right. Here the hole radius was $0.3a$, the slab thickness $0.5a$ the waveguide width a; TE-like bands are shown in black and TM-like in red.

Photonic crystals are periodic arrangements of dielectric media, such that in analogy with electron wavefunctions in atomic lattices, the optical modes' electric fields are given by Bloch functions, each of which is associated with a particular oscillation frequency ω and wavevector $\mathbf{k}$. In the context of photonic crystals, these functions

would describe the electric field:

$$\mathbf{E}(\omega, \mathbf{k}) = \mathbf{u}(\mathbf{r})_{\omega,\mathbf{k}} e^{i(\mathbf{k}\cdot\mathbf{r}-\omega t)}; \tag{1.1}$$

here, the field is a product of some function $\mathbf{u}(\mathbf{r})_{\omega,\mathbf{k}}$ that shares the periodicities of the lattice, and an exponential corresponding to propagation in the direction of the wavevector.

The dispersions of these modes, plotted in a single Brillouin zone of the lattice, have similarities to the electronic bandstructures of crystals; for example, with sufficiently high index contrast and appropriate geometry, a photonic band gap (a range of frequencies for which no modes exist) can exist for light with λ/n, n being the index of the core, approximately equal to the periodicity. This effect is the origin of many of these crystals' useful properties, and can occur for crystals with periodicity in one, two, or three dimensions; due to the practicality of planar fabrication, most work so far has been on one and two dimensional crystals. Example band structures of 2 and 1 dimensional crystals of silicon clad in oxide, are shown in Figs. 1-1 and 1-2.

Many of the interesting properties of these structures arise from the properties of defects in crystals that, with the aid of numerical electromagnetic calculations, can be carefully tailored. Point defects can create states localized in real space at frequences within the bandgap, which in the language of optics correspond to resonances; high-Q resonances can be obtained in structures by perturbing only a few wavelength-scale lattice sites, resulting in mode volumes on the order of $(\lambda/n)^3$, and the highest Q/V resonators so far made [KNM+06, NKT08a]. Such cavities have been useful in a wide variety of experiments; some example uses include very low-threshold lasers, solid-state implementations of cavity QED ideas, devices with nonlinear responses at low powers, optical buffers and delay lines [NKT08b], among many others.

Optimization of the quality factor of resonator designs form a significant component of this thesis, so an explanation of the mechanisms that limit the quality factor of photonic crystal cavities is necessary. I focus on the coupling between the resonant

mode and the continuum modes of the cladding material; this determines the radiative loss rate, which can be minimized by design. In a simple Fabry-Pérot cavity with metal mirrors, this outcoupling occurs only at the mirrors and is described simply in terms of the mirror reflectivity; for a distributed feedback structure in which two discrete mirrors are not well-defined, it becomes useful to consider the resonant mode in wavevector-space.

That is, the resonant mode can be decomposed into plane-wave components, via a Fourier transformation:

$$E(\mathbf{k}) = \frac{1}{\sqrt{2\pi}} \int d^3\mathbf{k} E(\mathbf{r}) e^{i\mathbf{k}\cdot\mathbf{r}}. \tag{1.2}$$

We are interested in coupling between the plane-wave components of the resonant mode and modes that propagate away from the slab with some amount of wavevector component $\mathbf{k}_\perp$ perpendicular to the plane of the crystal slab. For a crystal that only weakly breaks the (discrete) translational symmetry of the lattice, this coupling cannot alter the wave-vector component $\mathbf{k}_\parallel$ in the plane of the slab. Thus only those components $E(\mathbf{k})$ with a wavevector such that $\left|\mathbf{k}_\parallel\right| < |\mathbf{k}_{\text{clad}}(\omega)|$ where on the right side is the wavevector magnitude (at the resonant frequency) in the cladding material, can couple to propagating modes; modes with larger $\left|\mathbf{k}_\parallel\right|$ simply have a larger magnitude than any modes in the cladding, and modes with smaller $\left|\mathbf{k}_\parallel\right|$ couple to modes of the cladding such that $|\mathbf{k}_{\text{clad}}(\omega)| = \sqrt{|\mathbf{k}_\perp|^2 + \left|\mathbf{k}_\parallel\right|^2}$. This is schematically shown in Fig. 1-3; here the red area shows the k-distribution of some resonant mode at a single frequency, some of whose spatial components lie above the lightline of the cladding and hence contribute to radiative loss. For defects that strongly break the crystal's translational symmetry, further plane-wave components will contribute due to the momentum exchange made possible by the defect. However, just considering the former components gives some valuable simple intuition.

To illustrate, Fig. 1-4 shows some toy 1D mode profiles and their Fourier transforms. Consider the fields drawn as being confined to a core of index n, which is surrounded by vacuum. The spatial frequency of the carrier has been set to 1, so

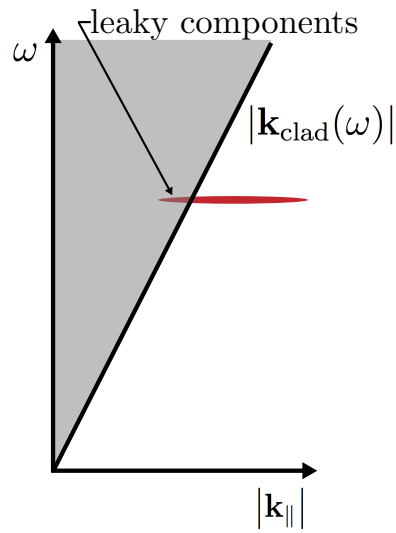

Figure 1-3: Illustration of in-plane wavevectors $|\mathbf{k}_{\parallel}|$ composing some resonant mode at a single frequency (represented by the red ellipse), with some spatial components lying above the cladding lightline and thus contributing to radiative loss.

any wavevector component with $|\mathbf{k}| < 1/n$ will couple to modes of the surrounding cladding. The top two plots show mode profiles for cavities with perfectly reflecting boundaries, i.e. truncated sinusoids, or sinusoids modulated by box envelope functions; the abrupt termination results in some high-frequency components in the envelope function's FT, which when shifted by the spatial sine frequency result in significant DC components around 0 wavevector. The bottom two plots show the same information for two modes which now have gradual DBR, such that the mode has a gaussian envelope function. Now, the FT of the envelope is narrowly confined around 0 wavevector, resulting in very low DC component after the shift by the carrier frequency.

These toy profiles illustrate a few points; for a given cavity design, large index contrast between the core and cladding will allow for lower radiative loss, because the range of wavevectors contributing to loss becomes smaller. But, for a given index contrast, designs that allow for gradual, rather than abrupt modulation of the mode envelope function decrease the DC spatial components, resulting in lower radiative loss [AASN03]. And for both abrupt and gradual envelopes, decreasing the length of the cavity to just a few wavelengths increases the energy in the DC components,

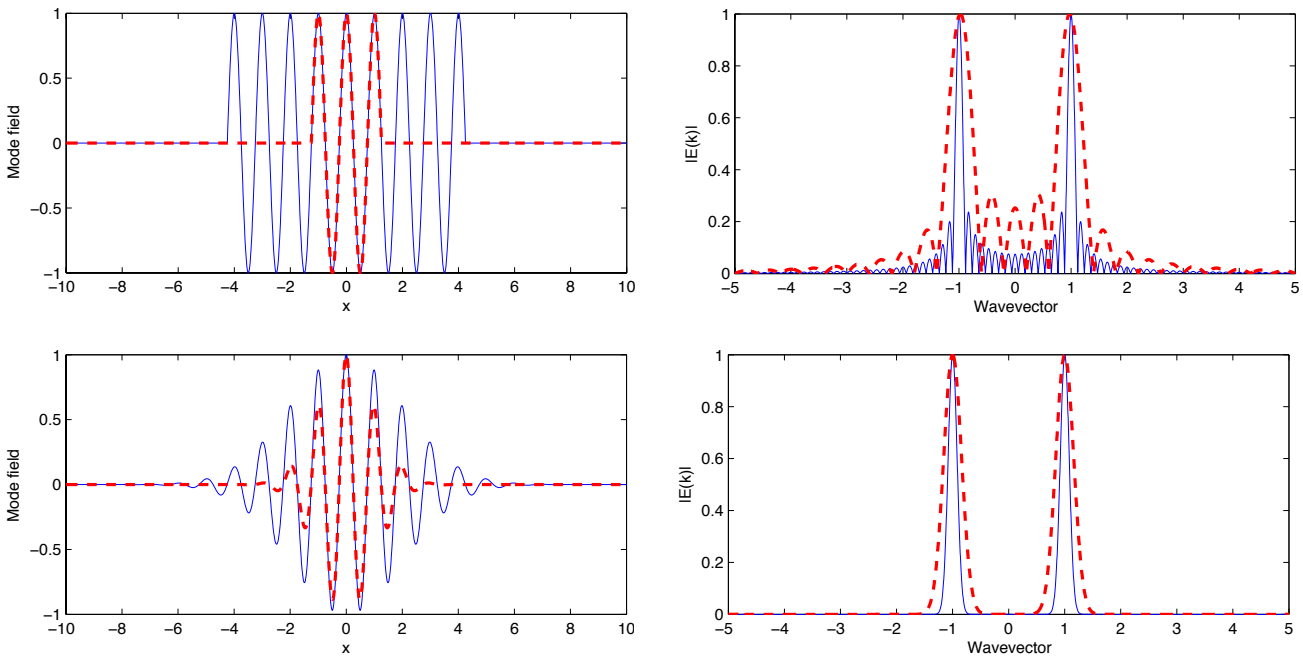

Figure 1-4: Different mode amplitudes (left) and corresponding Fourier transforms. The top plots correspond to cases with perfectly reflecting mirrors around a cavity 2 and 8 wavelengths long (red dotted and blue lines, respectively), and the bottom plots correspond to mode functions with gaussian envelopes. Wavevector components such that $|\mathbf{k}| < 1/n$, n being the resonator core index, contribute to radiative loss.

illustrating the challenge in maintaining Q as the cavity length approaches just a few wavelengths.

The important qualitative points relating to cavity design have thus been summarized, and particulars of a few different designs developed here will be discussed more in the chapter on cavity simulation and design. A number of other structures can be engineered with photonic crystals, which I do not discuss in detail; but, for example, extending a point defect in a 2D slab into a "line defect", for example one row of holes filled, can form a waveguide, useful of course for coupling to and between resonators. But additionally, these waveguides' dispersions are relatively flat within the bandgap, and can have very large group indices [VOHM05], providing another route to slow light and strong nonlinearities.

In the present context of silicon photonics, the small Q/V resonators offered by photonic crystal approaches are of immediate interest. Though their design is more involved than that of ring resonators, for a given material platform they can offer mode volumes smaller by over an order of magnitude than rings of comparable Q; they might thus be seen as continuing a trend begun by ring resonators [LC00]. Successful development of low mode-volume photonic crystal resonators in scalable platforms for silicon photonics could lead, for example, to more compact filters, more energy efficient-modulators with smaller junction capacitances, and devices that exploit a nonlinear response to light and which therefore benefit from the concentration of optical energy into a small volume. Though the photonic crystal structures developed below could have a number of uses, the primary focus of this thesis is one such nonlinear device implemented in scalable platforms, namely a resonant photodetector employing two-photon absorption. Existing approaches to photodetection in silicon are reviewed below.

1.3 Si photodetectors for infrared light

Designing integrated detectors that are compatible with standard CMOS electronics fabrication presents a significant challenge, due to the limited set of materials available

to work with; silicon (used for the waveguide cores) itself is of course transparent at wavelengths of interest, so simple band-to-band linear absorption cannot be used for detection as it can at higher photon energies. This challenge also presents an opportunity to explore a variety of different designs and physical mechanisms for detection, which I briefly review below.

1.3.1 Ge-based detectors

Germanium sits directly below silicon on the periodic table, and its crystals have the same zincblende structure. Its lattice constant differs from that of silicon by about 4%, which has led to alloys of silicon and germanium (SiGe), typically with Germanium fractions around 30%, being used in some CMOS processes as a strain layer, serving to increase the lattice constant of adjacent Si and thereby the electron mobility.

Ge has a lower absorption edge than Si (its bandgap is 0.67 eV, compared to silicon's 1.11 eV), so SiGe (whose bandgap lies somewhere between depending on the Ge fraction) can conveniently be used as an absorbing layer for detectors in CMOS flows. Detectors using pure Ge have achieved low dark currents and high responsivities on the order of 1 A/W out to 1550 nm light [AHL+07, LMG+05] in waveguide structures on the order of 10 μm long; significant avalanche gain has also been observed in appropriately designed Ge-on-Si structures [AXV10, KLM+09].

Practical issues limit Ge's utility in CMOS, however; the thermal stability of germanium and SiGe alloys results in a limitation on thermal processing following the SiGe deposition, and prevents integration of pure Ge or high mole-fraction SiGe. Photodetector performance in devices using the lower Ge-fraction SiGe available in CMOS processes is also significantly lower quality than with pure Ge; lower absorption coefficients result in devices with lower quantum efficiency, particularly at long wavelengths. Nevertheless, where a reliable SiGe process is available, it is likely to be a promising avenue, at least for wavelengths around 1300 nm. However, as photonic integration is a major goal in a number of processes in which Ge has no current use whatsoever (DRAM processes are an example), in these environments the material

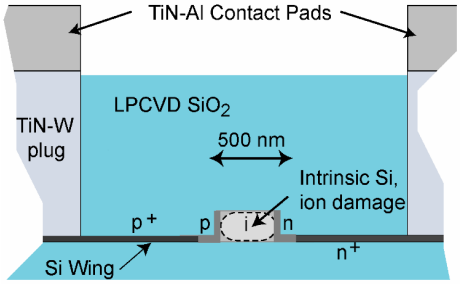

Figure 1-5: Cross section of Lincoln Labs defect-state absorption photodetector waveguide, with defect states created by ion implantation; copied from [GSG+07a].

requirement can be problematic.

1.3.2 Defect state photodetectors

Mid-gap localized electronic states at crystal defects produced by neutron or electron bombardment have been known to allow absorption of sub-bandgap light and generation of photocurrent in silicon for many years [FR59], but only a few groups in the last decade have reported detector devices using such absorption. The Knights group at McMaster University observed that both proton and silicon ion implantation into an SOI waveguide were observed to produce a photocurrent with rather low efficiency [BJK05, KBG06], and later enhanced somewhat for a given waveguide length by embedding the defected waveguide in a resonator [DJK10].

A Lincoln Labs group observed significantly higher detection efficiencies in similar structures having undergone silicon ion implantation [GSG+07b], along with some interesting properties of thermal and electronic "activation" of the defect absorbers and avalanche gain [GSG+07a]. It is unclear why these higher efficiencies were not reproduced by the Knights group; the difficulty in reproducing the behavior of bombarded samples is one of the major drawbacks with this approach.

It has also been pointed out that simply taking advantage of the defect states arising at the Si/SiO_2 boundary at the waveguide edges, and the large mode overlap with this region in small cross-section geometries, allows photodetection [BJHS08], albeit in rather long structures.

Most aligned with what is attempted in this work, the Lipson group observed

efficiencies of 0.15 A/W via linear absorption in polycrystalline ring resonators (of 50 μm radius, with quality factors of 10,000) [PLZL11], attributed to defect states naturally present in polysilicon, in a similar contact geometry to that of the Lincoln Labs photodetector. The quoted efficiency was achieved at 13 V reverse bias across the diode, for low optical input powers; the authors observed a decrease in efficiency with increasing power, for reasons that are unclear from the paper but show that TPA was not a dominant process in their device.

1.3.3 Two-photon absorption photodetectors

Pure Si can absorb sub-bandgap photons weakly via two-photon absorption. The efficiency of this nonlinear absorption increases with intensity, I (absorbed power goes as the I^2), and thus what would be a very weak effect in a simple waveguide can be enhanced by orders of magnitude in a structure that concentrates light energy, such as a low group velocity mode or a microresonator. Use of photonic crystal resonators to enhance nonlinear absorption was proposed and analyzed numerically in [BAIS09]; an illustration of a structure they consider is copied in Fig. 1-6.

The basic reason for the enhancement is explained by some simple scaling relations. The quality factor of a resonator governs its photon decay rate via $Q = \omega\tau$, and since the stored cavity energy is given by $\dot{W} = P_{\text{in}} - W/\tau$, the steady state $W = P_{\text{in}}Q/\omega$, and hence the average energy density $U = \frac{P_{\text{in}}Q}{\omega V}$. The two-photon absorption coefficient is defined such that, for some propagating intensity I, $\frac{dI}{dz} = -\beta I^2$, and hence that $\frac{dI}{dt} = -\beta I^2 \frac{c}{n_g}$. $I = U\frac{c}{n_g}$, so the time rate of change of energy density can be written $\dot{U} = -\beta U^2 \frac{c^2}{n_g^2}$. Thus, for a given input power, the total optical power absorbed per unit time over the resonator volume is $\dot{W} = V\dot{U} \propto Q^2/V$.

This effect has been observed, using crystalline silicon's β of about 1 cm/GW, in microdisk resonators [CP10] of radius 5μm and quality factors of 10^5, where efficiencies of about 0.5% were observed. In [TST+10], (device schematic copied in Fig.1-7, a similar Q, but a much smaller volume allowed for TPA photocurrent at much smaller powers and a maximum efficiency of 10%. An SOI crystal of a similar structure, but with lower Q due to the bottom oxide was developed in [HCH+10], in which a

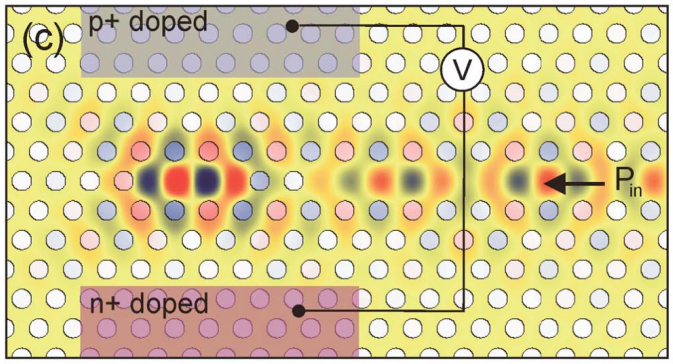

Figure 1-6: Nonlinear PC detector considered in [BAIS09], with a photonic crystal microcavity formed in the intrinsic region of a PIN diode, coupled to a feeding waveguide.

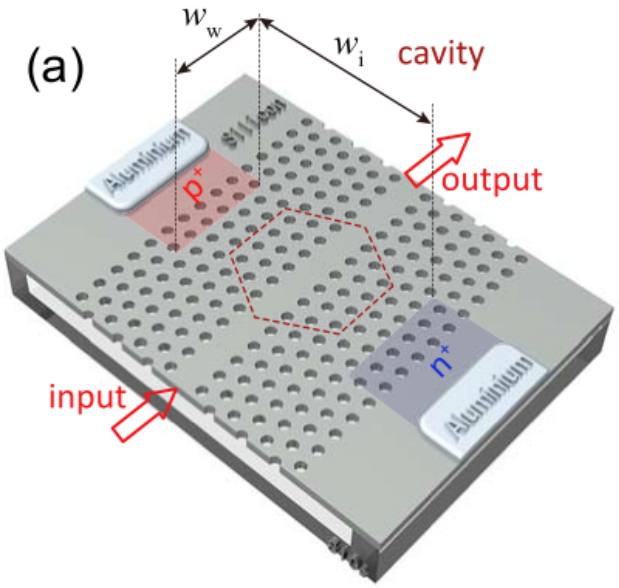

Figure 1-7: Nonlinear PC detector experimentally realized in [TST+10], based on a gradually confining PC cavity formed in a waveguide.

maximum efficiency of about 2% was achieved.

1.3.4 Overview of this work

This thesis aims to use the photonic crystal approach to produce detectors with the highest possible Q with wavelength-scale Vs, within the dielectric environment of a full CMOS flow. The TPA contribution to the photocurrent increases with small volume resonators, whereas the defect-mediated linear absorption contribution will contribute strongly as long as this absorption, and not radiative loss from the cavity, forms the dominant loss mechanism.

The dielectric environments in the processes used here pose a challenge, in that the presence of higher index claddings than air (as is used in the highest Q crystals published), such as oxide or silicon nitride, increase radiative loss from the cavity, to an extent depending on the cavity design. Furthermore, the devices studied here will be made in the polycrystalline silicon layer of a DRAM process, in which waveguide losses are substantially higher than crystalline silicon; this will limit the maximum achievable Q, and it is not obvious initially what the impact of the hole boundaries will be in terms of modal absorption and loss in polysilicon. Due to the constraints of the photolithographic process, as well, designs had to abide by certain minimum feature sizes, which are different from the constraints on e-beam fabricated devices (these will be discussed in Ch. 3).

Quantum efficiency (QE) and bandwidth are the two essential metrics of a photodetector in a photonic link. In a typical link, modulators, and not the detectors, are the bottlenecks in terms of bandwidth per wavelength; in silicon devices, these can respond to 10 GHz signals, which therefore serves as a target for the photodetector bandwidth, though with the caveat that optimal receiver architectures may rely on slower circuitry (and hence slower detectors operating in parallel). QE essentially sets the required power input to the photodetector, for a given receiver sensitivity. A reasonable estimate for sensitivity is approximately 10μA; a system would ideally not require more than 100 μW reaching the detector, which requires a QE of around 10%. Of course, a higher QE linearly scales the required optical power, resulting in

significant gains in terms of total energy required.

The physics relevant to designing photonic crystal resonators to be used for these devices was already described briefly above, but one last part relevant to these devices remains, namely the coupling of light into such resonators. The next section describes this.

1.4 Coupled mode equations for lossy resonator loading

The devices discussed in this thesis aim to absorb light in a resonator, which demands some understanding of the how light is coupled in from a feeding waveguide. This model, which follows the coupled-mode formalism in [Hau84], informs the design and is worth reviewing here.

Both configurations drawn in Fig. 1-8 can be analyzed with a simple coupled mode formalism. In the top case, two mirrors of finite reflectivity couple an incident wave (with amplitude $\tilde{s}$, normalized such that $|\tilde{s}|^2$ corresponds to power) couples to a resonator (with mode amplitude $\tilde{a}$ such that $|\tilde{a}|^2$ gives energy). The reflected and transmitted components have amplitudes r and t.

The modal amplitude $\tilde{a}$ oscillates at its natural angular frequency ω_0, and in the absence of loss, $\tilde{a} \propto e^{j\omega_0 t}$. We assume a decay due both to coupling out of the mirrors (external loss), and to loss intrinsic to the material filling the resonator, with rates defined as $2/\tau_e$ and $1/\tau_0$ ($1/\tau_e$ corresponds to the rate out of a single mirror). Here these decay rates are defined for the amplitudes, so the corresponding quality factors are:

$$Q_0 = \frac{\omega_0 \tau_0}{2}, \tag{1.3}$$

$$Q_e = \frac{\omega_0 \tau_e}{4}, \tag{1.4}$$

$$\frac{1}{Q_l} = \frac{1}{Q_0} + \frac{1}{Q_e}, \tag{1.5}$$

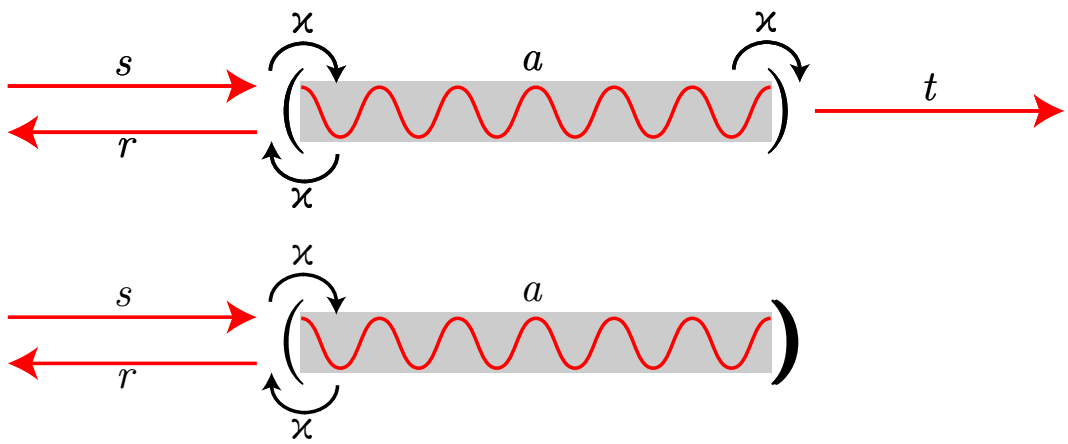

Figure 1-8: Schematic of cavity input amplitude (s), reflected (r) and transmitted (t); the coupling coefficient κ between these and the resonant mode amplitude are assumed to be the same for both mirrors. The top arrangement has two mirrors of equal reflectivity, the bottom one mirror that couples to a feed waveguide and one perfectly reflecting mirror.

where Q_0 corresponds to the quality factor in the limit of no coupling to feeding waveguide modes, Q_e describes only the loss rate of this coupling (τ_e is defined for a single mirror, so this Q_e corresponds to the case with two lossy mirrors), and Q_l is the total quality factor of the loaded cavity.

If these decay rates are small compared to the oscillation frequency, they can simply be added to the equation governing $\tilde{a}$, including a source wave with time-varying amplitude $\tilde{s}$:

$$\frac{d\tilde{a}}{dt} = j\omega_0\tilde{a} - \left(\frac{1}{\tau_0} + \frac{2}{\tau_e}\right)\tilde{a} + \kappa\tilde{s}; \tag{1.6}$$

κ describes coupling between the incident mode and the resonator, and is thus closely related to the τ_e that describes the decay out of the resonator mode into this mode. A time-reversal symmetry argument shows that $\kappa = \sqrt{2/\tau_e}$.

Assuming an approximately single frequency input with a slowly-varying amplitude s such that $\tilde{s} = se^{j\omega t}$, and making the transformation $\tilde{a} = ae^{j\omega t}$ (this a is now a slowly varying amplitude, so its steady state can be found by setting its derivative to 0) the equation becomes

$$\frac{da}{dt} = j(\omega_0 - \omega)a - \left(\frac{1}{\tau_0} + \frac{2}{\tau_e}\right)a + \sqrt{\frac{2}{\tau_e}}s. \tag{1.7}$$

The steady state energy in the cavity is solved for by setting $\frac{d|a|^2}{dt} = 0$, which results in the condition that

$$U = |a|^2 = \frac{\frac{2}{\tau_e}P_{in}}{(\omega - \omega_0)^2 + \left(\frac{1}{\tau_0} + \frac{2}{\tau_e}\right)^2}, \tag{1.8}$$

which translates into a transmission coefficient:

$$T = \frac{|\kappa|^2 U}{|s|^2} = \frac{\frac{4}{\tau_e^2}}{\left(\frac{1}{\tau_0} + \frac{2}{\tau_e}\right)^2 + (\omega - \omega_0)^2}. \tag{1.9}$$

The reflected amplitude involves interference of the directly reflected component of the input amplitude s and that leaked out by the cavity. Applying to this the constraint that the power in must equal the sum of the power reflected and the power lost from the cavity results in the expression $r = -s + \kappa a$; importantly, the two contributions to r are π out of phase. From this,

$$\left|\frac{r}{s}\right|^2 = R = \frac{\frac{1}{\tau_0^2} + (\omega - \omega_0)^2}{\left(\frac{1}{\tau_0} + \frac{2}{\tau_e}\right)^2 + (\omega - \omega_0)^2}. \tag{1.10}$$

To adopt these equations to the case of a single feeding waveguide (bottom in Fig. 1-8, we only need to change the total cavity loss rate from $\frac{1}{\tau_0} + \frac{2}{\tau_e}$ to $\frac{1}{\tau_0} + \frac{1}{\tau_e}$ (also, $Q_e \to \frac{\omega_0 \tau_e}{2}$). There no longer is any transmitted component, and the reflection coefficient,

$$R = \frac{\left(\frac{1}{\tau_e} - \frac{1}{\tau_0}\right)^2 + (\omega_0 - \omega)^2}{\left(\frac{1}{\tau_e} + \frac{1}{\tau_0}\right)^2 + (\omega_0 - \omega)^2}, \tag{1.11}$$

now can equal 0 on resonance as long as $Q_e = Q_0$, i.e. the intrinsic loss rate equals the loss rate into the feed waveguide mode. This condition is known as the critical coupling condition and results in complete power transfer into the resonant mode;

tuning the coupling between the bus and the resonator will have a significant impact on detection efficiency.

1.5 Summary

This chapter presented an overview of integrated optics and put the present work into context within silicon photonics. The uses of photonic crystals within such a platform were discussed, along with the factors that come into play in designing high-Q, small volume resonators in different dielectric environments. The rationale for the general approach to nonlinear photodetection was described, and the critical coupling condition was developed from a coupled mode analysis. The next chapters will present a more detailed analysis of resonant TPA in a microresonator, and its physics in polycrystalline silicon, and then proceed to the design and fabrication of these devices in current CMOS foundries, and finally their testing.

Chapter 2

TPA in Si microresonators

The behavior of the resonant detectors explored in this work is determined by both the absorptive characteristics of the silicon and the properties of the optical resonator fabricated. Most of the devices discussed in this thesis are actually formed in polycrystalline silicon, in which TPA could conceivably occur differently (and, as discussed below, more strongly) than in single crystal silicon. This chapter discusses the physics of TPA in single crystal and polycrystalline silicon, measurements of this nonlinear absorption, and finally presents a simple model to predict the efficiency of a resonant TPA photodetector in the steady state.

2.1 Physics of TPA in single crystal silicon

Silicon has an indirect bandgap of 1.11 eV, and a direct gap of approximately 3.5 eV. Light around 1550 nm, corresponding to a photon energy of $h\nu \approx 0.8$ eV, results in no one-photon interband transitions, and two-photon absorption must occur as a phonon-assisted process to satisfy momentum conservation. Since the process involves two photons and one phonon, its rate is described by a third-order Fermi's Golden Rule; a theoretical calculation of the rate based on this is presented in [Din03], and Fig. 2-1 shows two possible transition sequences that would appear in a rate calculation – arrows 1 and 2 represent transitions to intermediate "virtual" states, through a phonon (dotted lines) or photon (solid lines) interaction that does not conserve energy;

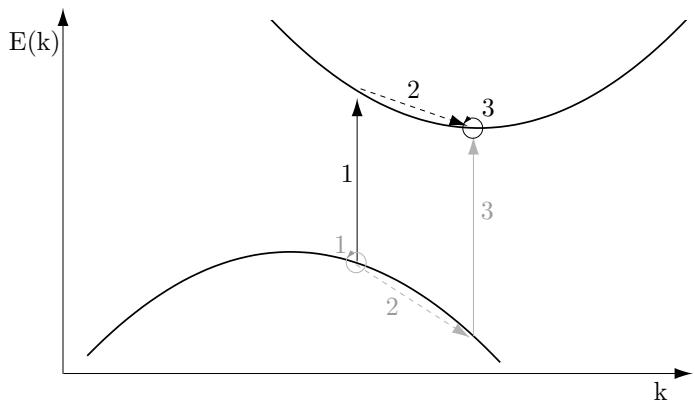

Figure 2-1: Schematic of two possible realizations (labeled in black and grey) of a phonon-assisted TPA process between the valence band and and indirect valley in crystalline silicon; dotted lines represent phonon transitions, solid photon transitions.

the greater the energy difference in these transitions, the weaker the process.

The strength of the TPA process is defined in terms of an intensity-dependent contribution to the total intensity attenuation coefficient, α, where, for a beam propagating along z with intensity $I(z)$,

$$\frac{dI}{dz} = -\alpha(I)I(z), \tag{2.1}$$

and

$$\alpha(I) = \alpha_L + \beta I. \tag{2.2}$$

Here α_L is some constant, linear loss, and the coefficient β, in units of length/power, characterizes the TPA process. In crystalline silicon, various published measurements put β around approximately 0.5 to 0.8 cm/GW [BRvD07, MNK+12, LPA07].

2.2 Linear and nonlinear absorption in polycrystalline silicon

The optical properties of polysilicon can be significantly different than those of crystalline silicon; in particular, scattering at grain boundaries, as well as absorption due

to transitions involving localized electrons arising at grain boundaries, contribute additional sources of loss. In the context of work towards a resonant TPA photodetector, a large α_L limits resonator Qs, but a larger β could be beneficial. This motivates an understanding of the role of the grain boundaries in absorption. Previous work has fit linear absorption spectra in pSi with a simple model for energy distribution of mid-gap states; this section discusses applying a similar model to absorption spectra measured in our pSi waveguides, and then discusses qualitatively how such states may be expected to contribute to TPA.

2.2.1 Defect-state linear absorption model

The mid-gap states localized at silicon grain boundaries have been posited to arise from dangling bonds, which result in a series of states clustered around a particular energy within the gap [Sea85]. In [JJB83], the authors observe that their measured absorption spectra, as well as previous electronic measurements on Fermi Level pinning, are consistent with a peak in the density of states at approximately 0.35 eV above the valence band edge at the defects. This density of states, with a Fermi level pinned at approximately the energy of maximum defect state density, is shown in Fig. 2-2. The references cited indicate that similar Fermi level pinning behavior had been observed in a variety of different polysilicon samples, indicating that this dangling bond behavior may be fairly universal. The work in this section is insufficient to claim that this model is accurate for our poly, but aims to confirm that this model for the DOS at least is consistent with linear absorption measured in our poly waveguides.

Linear absorption is calculated using Fermi's golden rule for first order processes,

$$R = \frac{2\pi}{\hbar}\frac{1}{V}\sum_{\alpha,\gamma}\left|\langle\gamma|H'|\alpha\rangle\right|^2\delta(E_\gamma - E_\alpha - \hbar\omega); \tag{2.3}$$

Here, α and γ correspond to initial and final electronic states, and the δ-function selects only transitions conserving energy for photons of a given frequency. $H' =$

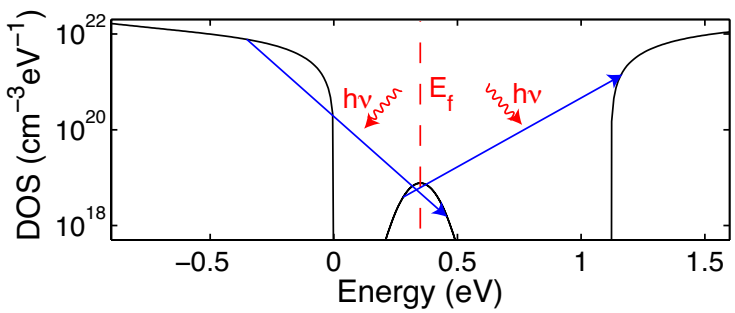

Figure 2-2: Model DOS for pSi linear loss calculation, with mid-gap states centered around 0.35 eV, with a fermi level pinned at the peak density. Optical transitions as illustrated couple occupied to empty states.

$\frac{e}{m}\mathbf{A}\cdot\mathbf{p}$ is the interaction Hamiltonian, and the matrix element,

$$\langle\gamma|H'|\alpha\rangle = \frac{ie}{m\omega}EP_{\alpha,\gamma}, \tag{2.4}$$

where $P_{\alpha,\gamma}$ is the momentum matrix element linking the initial and final states. The dominant transitions have localized grain states as either initial or final states, and so, unlike for transitions between extended Bloch-states, k-vector conservation is not required and we assume the process occurs without involving phonons.

The strength of the transition is typically expressed in terms of the oscillator strength, defined as:

$$f_{\alpha,\gamma} = \frac{2\left|P_{i,f}\right|^2}{m\hbar\omega}; \tag{2.5}$$

we assume that a constant, average oscillator strength f_0 characterizes all transitions involving band states and the defect states. After converting the sums into into an integral over initial states, the total absorption rate per unit volume can be written as:

$$R = \pi\left(\frac{eE}{m\omega}\right)^2 m\omega f_0 \int \mathrm{d}E_\alpha \left[\rho_\gamma(E_\alpha+\hbar\omega)\rho_\alpha(E_\alpha)\left[1-f(E_\alpha+\hbar\omega)\right]f(E_\alpha)\right], \tag{2.6}$$

where the ρs represent densities of initial and final states separated by the correct photon energy, and the Fermi distributions f guarantee transitions only between occupied initial states and unoccupied final states.

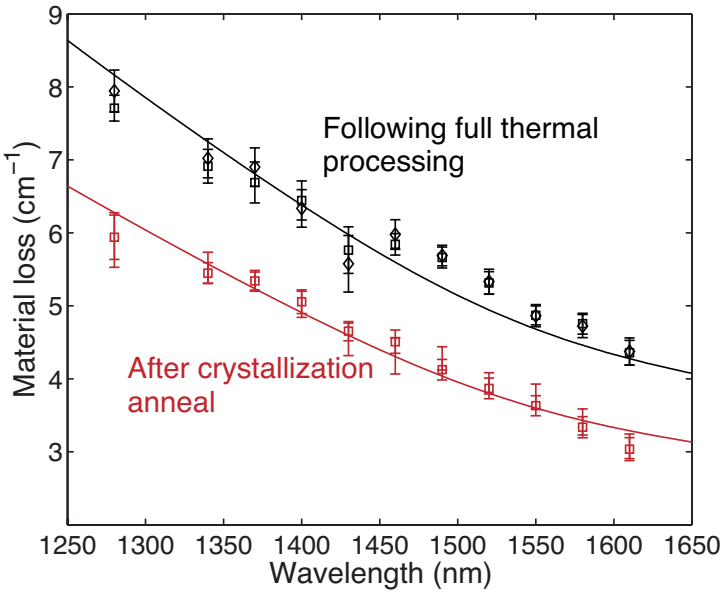

Figure 2-3: Linear loss fits to waveguide loss measured by Jason Orcutt. The two data sets correspond to samples having undergone different anneals; the higher loss sample underwent further high temperature anneals than the lower.

In my calculation, the densities of the conduction and valence bands were fit to the results of IBM's DAMOCLES calculation for silicon, and the mid-gap states were matched to [JJB83] as described above. The density and strength of these transitions was unknown, however, and so the oscillator strength was used as the only fitting parameter; it serves only to scale the magnitude of the curve, and not the shape. Keeping this strength constant and tuning the peak density of defect states is equivalent.

As shown in Fig. 2-3, this model produces a reasonable fit to the measured waveguide loss. Hydrogenation of the dangling bonds is known to passivate the defect, and since the sample that underwent further high temperature anneals gave larger loss (fit simply by increasing the peak density of defect states), it is reasonable to speculate that the effect of the anneal was to outgas some of the hydrogen atoms, resulting in more mid-gap electronic states and uniformly higher loss.

The loss measurements above were obtained in waveguides, and so this analysis of course neglects another possible source of loss, which is scattering from the waveguide

boundaries. The fact that the measured waveguide loss was observed to scale with the fraction of the mode energy in the core for different waveguide dimensions rules this out as a dominant contributor to loss [OTK+12].

2.2.2 Possible role of defect states in TPA in pSi

One would also expect the mid-gap grain boundary states to contribute, as intermediate states, to band-to-band two-photon transitions. The localization of the grain boundary states in real space implies delocalization in k-space and thus a state that does not have a well-defined crystal momentum; thus, the momentum conservation requirement, that in crystalline silicon resulted in the dominant process being phonon-assisted, can be expected to be relaxed in pSi.

In addition to this relaxation of the requirement of phonon involvement, depending on their position within the gap, the defect states can form intermediate states nearly resonant with the incoming photons, resulting potentially in a resonant enhancement of the TPA process. Such an effect has been observed, for example in atomic gases, to result in a large enhancement in TPA when an intermediate state, separated by near the energies of the photons involved, lies in between the initial and final atomic states [BL74].

These two different possible contributors to enhancement can be seen, first by writing the second order Fermi's Golden Rule (for a process now not requiring a phonon):

$$R = \frac{2\pi}{\hbar V} \sum_{c,v} \left| \sum_{m} \frac{\langle c|H'|m\rangle\langle m|H'|v\rangle}{E_m - E_v - \hbar\omega} \right|^2 \delta(E_c - E_v - 2\hbar\omega), \tag{2.7}$$

and noting that the the denominator is the quantity minimized having near-resonant intermediate states. Such an enhancement has been observed in amorphous silicon, in which a z-scan measurement (discussed below) indicated a β of 120 cm/GW [ISF07]; a few observations of enhanced TPA in porous silicon samples due to the large density of surface states have also been reported. That a similar effect would be possible in pSi motivated the measurements that follow, which aimed to measure whether the mechanisms speculated above in fact result in enhancement of TPA in pSi.

2.3 Measurements of nonlinear absorption in polysilicon

Motivated by the argument for the potential enhancement of TPA in pSi over crystalline Si, we attempted to measure β through a few different methods. As of now a conclusive answer has not been reached (primarily due to the difficulty of isolating free-carrier from TPA effects except in ultrafast measurements, as discussed more below), but this section describes measurements done so far nevertheless.

2.3.1 Lock-in ring Q measurements

The nonlinear loss can be characterized by observing the decrease in quality factor of a resonator as stored energy increases; this quality factor can be measured by fitting a transmission profile to a Lorentzian, but at high powers, resonance pulling due to the thermo-optic effect results in asymmetric transmission profiles, complicating this fitting in a simple single-beam arrangement. Using a weakly modulated probe beam in addition to the strong pump, however, and measuring only the transmitted light at the modulation frequency with a lock-in technique, avoids this. The strong beam sets the cavity Q, and since the probe beam is too weak to significantly alter it, the response of the cavity to the probe beam is linear, resulting in a clean Lorentzian.

From a fit quality factor, the additional intensity-dependent waveguide loss $\Delta\alpha_{\mathrm{wg}}(P)$ can be calculated simply, because $Q_{\mathrm{tot}}^{-1} = Q_{\mathrm{lin}}^{-1} + Q_{\mathrm{nl}}^{-1}$, where Q_{lin} is due to the loss rate at low intensities and $Q_{\mathrm{nl}} = \omega_0/\gamma_{\mathrm{nl}} = \frac{\omega_0 n_g}{\Delta\alpha_{\mathrm{wg}} c}$, and

$$\alpha_{\mathrm{wg}}(P) = \alpha_L + \Delta\alpha_{\mathrm{wg}}(P) = \alpha_L + \beta I_{\mathrm{eff}}^{(2)} + \sigma(N_1 + N_2); \tag{2.8}$$

here, $I_{\mathrm{eff}} = P/A_{\mathrm{eff}}^{(2)}$, where A_{eff} is the effective mode area for second order processes, and

$$N_1 = \Gamma_l \frac{\alpha_L \tau_r}{h\nu} \frac{P}{A_{\mathrm{eff}}^{(2)}} \tag{2.9}$$

is the linear-absorption produced free carrier density, and

$$N_2 = \frac{\beta \tau_r}{2h\nu} \frac{P^2}{A_{\text{eff}}^{(2)} A_{\text{eff}}^{(3)}} \tag{2.10}$$

is the TPA-generated free carrier density [MNK+12]. Here, Γ_l is the fraction of linearly absorbed photons that produces an electron-hole pair (some transitions in the poly are expected instead to transfer an electron to a defect state) and τ_r is the recombination time.

The total waveguide loss thus includes a component α_L that is independent of the power guided, a component $\alpha^{(1)}$ linear in the power guided:

$$\alpha^{(1)} = \frac{\beta}{A_{\text{eff}}^{(2)}} + \Gamma_l \frac{\alpha_L \sigma \tau_r}{h\nu A_{\text{eff}}^{(2)}}; \tag{2.11}$$

and a further quadratic term arising from the FCA from TPA-excited photocarriers. As discussed below, isolating this quadratic term proved challenging, and so I focus here on the linear term. The relevant effective area, then, accurate for the high index contrast here, is [KJP+07]:

$$A_{\text{eff}}^{(2)} = \frac{\mu_0}{\epsilon_{\text{pSi}}} \frac{\left| \int\int_{\infty} \text{Re}\left(\mathbf{E} \times \mathbf{H}^*\right) \cdot \hat{\mathbf{z}} \mathrm{d}A \right|^2}{\int\int_{\text{pSi}} |\mathbf{E}|^4 \, \mathrm{d}A}, \tag{2.12}$$

where the different domains of the integrations account for the incomplete confinement of the mode in the pSi core, and the group index of the guided mode is included in the integration of the Poynting vector; this area was calculated in COMSOL to be $0.085\mu\text{m}^2$ for the waveguide dimensions (575×120 nm^2, pSi clad by oxide) used in the measurement. The group index was found to be $n_g = 3.77$ at 1550 nm.

Fig. 2-4 shows five lock-in traces corresponding to drop port signals on a 10μm ring, near critically coupled, with 5 different pump laser output powers. The oscillations with respect to the Lorentzian fits, most clear to the red of the peak in the blue trace, are due to reflections from the grating couplers.

In the measurement, the input power is measured at a power tap right before

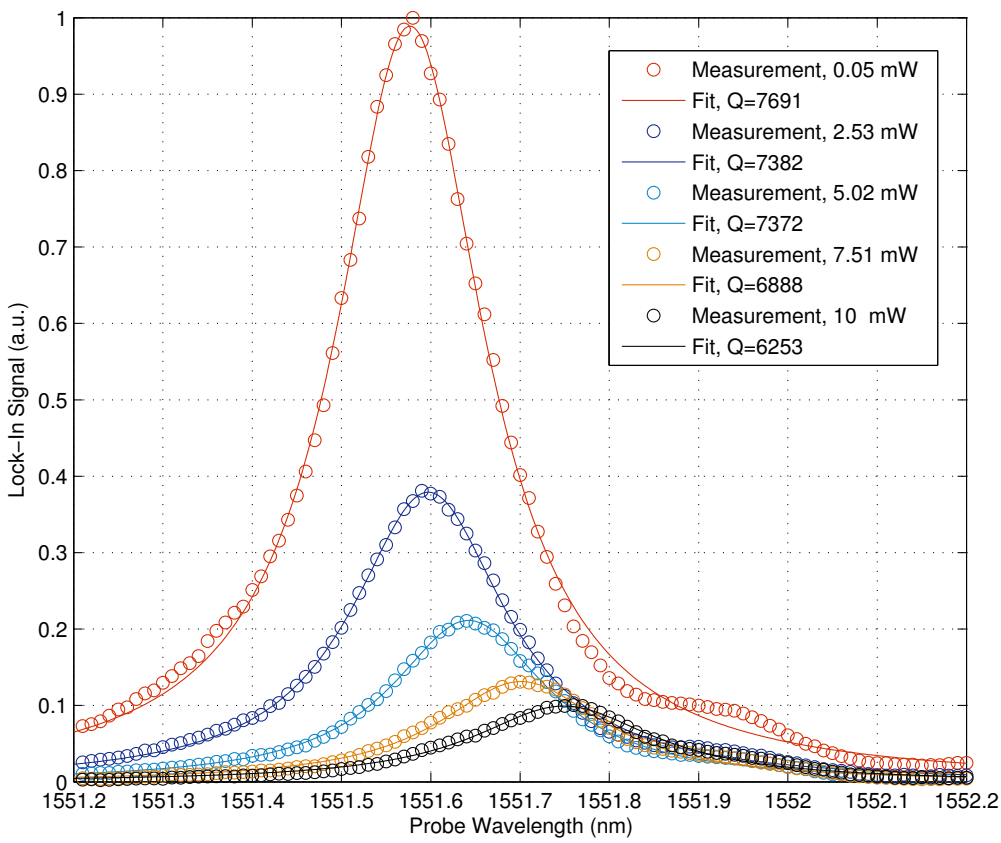

Figure 2-4: Measured lock-in signal, corresponding to probe transmission, through a 10 μm radius pSi ring resonator at various input pump powers. Pump powers labeled are directly out of the laser, and do not account for coupling loss into the ring. Fitted Qs are labeled in the legend.

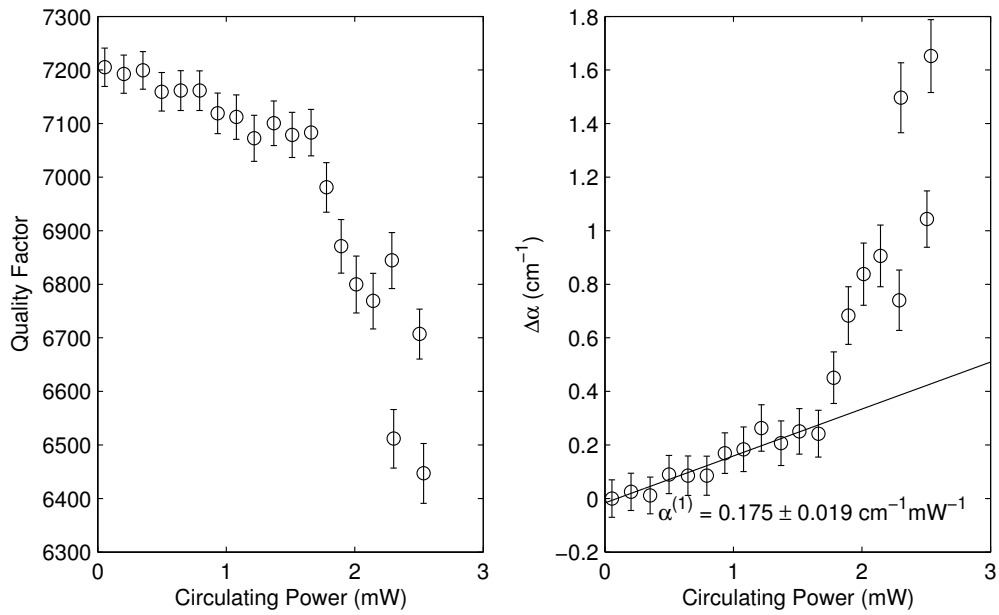

Figure 2-5: Measured quality factors (left) and nonlinear waveguide loss (right) as a function of resonator circulating power, along with a linear fit to the waveguide loss for the low powers. Error bars on measured points and quoted $\alpha^{(1)}$ correspond to 68% confidence intervals in the Lorentzian and linear fits, respectively.

the waveguide grating coupler; combined with the coupler loss (estimated to be 7 dB based on through-port measurements off resonance), this allows an estimate of the in-waveguide power. The power circulating in the ring is this value, multiplied by the ring's intensity enhancement factor $\mathcal{F}/\pi$, where $\mathcal{F}$ is the cavity finesse; this is easily determined at each pump power, since the FSR of the cavity is measured, and the finesse at each power is simply the ratio of this to the resonance width.

Fig. 2-5 makes use of this to show the fit Qs and calculated $\Delta\alpha$s as a function of the circulating power in the resonator. Past about 1.6 mW, the waveguide loss seems to clearly depart from the linear trend. Ideally, this would be due to FCA from TPA, giving rise to a quadratic term in α; however, this does not describe the data well, which suffers from the additional complication of the transmission oscillations associated with grating coupler reflection which caused an artificial decrease in peak amplitude as power increased, due to the resonance shift. Fits to the high-power data thus indicated differences in Q larger than can be attributed truly to nonlinear loss.

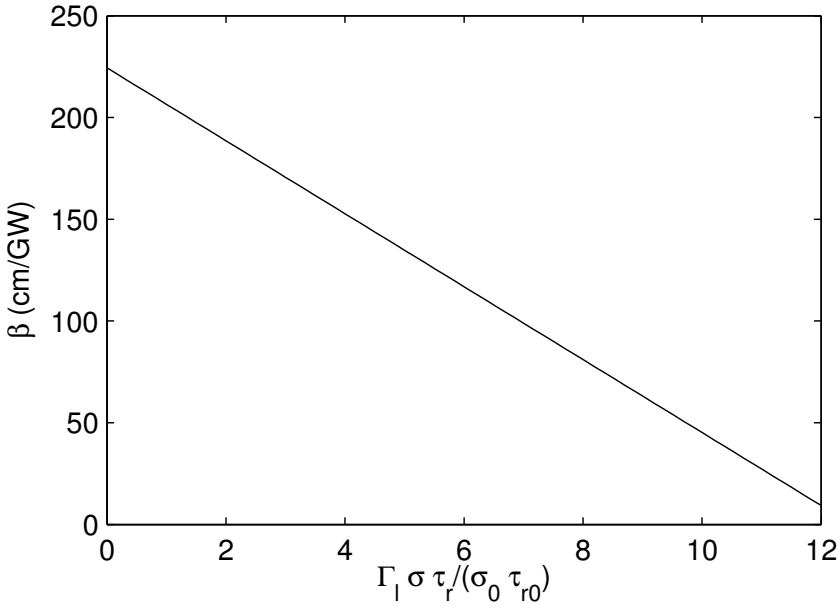

Figure 2-6: Inferred βs versus FCA strength from linear absorption-generated carriers, from lock-in quality factor measurements. The x-axis shows the product of the three uncertain quantities relevant to free-carrier absorption that appear in Eq. 2.11, normalized to the values $\sigma_0 = 0.73 \times 10^{-17}$ cm^2 and $\tau_{r0} = 100$ ps, and $\Gamma_l = 1$. If no linearly absorbed photons contributed to FCA, a β of 225 cm/GW would be inferred.

This makes it difficult to attempt to fit both the linear and quadratic component of the loss, and below I focus only on the linear component.

The measurement of $\alpha^{(1)}$ from the fit in Fig. 2-5, if all free-carrier absorption parameters were known, should give an accurate value for β. However, the relevant parameters Γ_l, σ, and τ_r were not measured in our polysilicon. Fig. 2-6 therefore plots the β calculated from Eq. 2.11 as a function of the product of the uncertain FCA parameters, $\Gamma_l \sigma \tau_r$, that appears in the second term of the equation. α_L was previously measured in these waveguides to be 3.2 cm^{-1}. The defect model for pSi means that considerations of free-carrier absorption from linear absorbed photons must consider electrons and holes separately, rather than electron-hole pairs. In [LPA07], a free-carrier loss coefficient $\alpha_{\text{fca}} = N_{eh}\sigma_a$ ($\sigma_a \approx 1.45 \times 10^{-17}$ cm^2) is used, where N_{eh} is the electron-hole pair density, and σ_a is the effective cross section counting both the (approximately equal – the relative contributions of electrons to holes is 8.5/6.0) contributions of the electron and hole. The linear absorption events in poly are expected to produce not a free electron-hole pair, but *either* a free electron or hole. thus, the $N^{(1)}$ of Eq. 2.9 (calculated by considering the number of photons absorbed per unit volume) refers not to the electron-hole pair density, but to the sum of the free electron and hole densities; therefore I take as my estimate for σ one-half the literature value for e-h pairs.

The x-axis is thus normalized to $\Gamma_l = 1$ (all linear absorption generates either a free electron or a free hole), reasonable assumptions of $\sigma = 0.5\sigma_a = 0.73 \times 10^{-17}$ cm^2, and $\tau_r = 100$ ps, approximately as reported for polysilicon waveguides. N_1, the sum of the free electron and hole densities produced by linear absorption, is calculated from Eq. 2.9.

Normally, analysis of crystalline silicon waveguides would assume no free carrier population to linearly absorbed light ($\Gamma_l = 0$), and the measured TPA coefficient would be about 225 cm/GW. However, under my assumption that each linearly absorbed photon produces either a free electron or hole, ($\Gamma_l = 1$), the plot indicates that a significantly enhanced β is expected unless $\sigma\tau_r$ is greater than about 12$\times$ the assumed value.

One might hope to separate the FCA and TPA contributions by conducting a double-chopped experiment, in which the pump is modulated at f_{pump} as well. If $f_{\text{pump}} \gg \tau_r^{-1}$, the carrier population does not track the pump and only TPA from the pump will result in AC modulation of the probe. Conversely, both contribute to modulation of a probe when f_{pump} is small; hence, comparing the magnitudes of a sum frequency as f_{pump} is changed could allow these two effects to be separated. In measurements in resonators, though, the additional timescale of the cavity decay time also smooths out the pump intensity. To exceed the carrier lifetime of 100 ps requires $f_{\text{pump}} \gg 10$ GHz, whereas a cavity Q of 10,000 corresponds to a pump modulation bandwidth of 20 GHz. The intracavity power thus cannot be modulated fast enough at these Qs to allow an averaging out of the FCA.

2.3.2 Single beam ring transmission measurements

The initial measurements attempted to basically measure the peak through extinction of various rings as a function of power input; though the profiles were not Lorentzians, the peak transmissions could still be fit to a simple model assuming some intensity-dependent loss in the resonator. As the power circulating in the ring increased, the loss increased due to its nonlinear component, resulting in a decrease in the peak extinction.

The theory predicting the peak extinction on resonance is summarized in the transmission matrix description of the ring resonator, relating the input field amplitudes E_{in} to the field within the ring (E_{r1} is at the input coupler, including the transmitted component of the circulating ring power – see Fig. 2-7 – and E_{r2} at the output coupler), and hence to the fields at the through (E_{t}) and drop E_{dr} ports:

$$\begin{bmatrix} E_t \\ E_{r1} \end{bmatrix} = \begin{bmatrix} t & \kappa \\ -\kappa^* & t^* \end{bmatrix} \begin{bmatrix} E_{in} \\ E_{r2} e^{-\frac{\alpha}{2}\pi R} e^{i\frac{\theta}{2}} \end{bmatrix} \tag{2.13}$$

$$\begin{bmatrix} E_{r2} \\ E_{dr} \end{bmatrix} = \begin{bmatrix} t^* & -\kappa^* \\ \kappa & t \end{bmatrix} \begin{bmatrix} E_{r1} e^{-\frac{\alpha}{2}\pi R} e^{i\frac{\theta}{2}} \\ E_{add} = 0 \end{bmatrix} \tag{2.14}$$

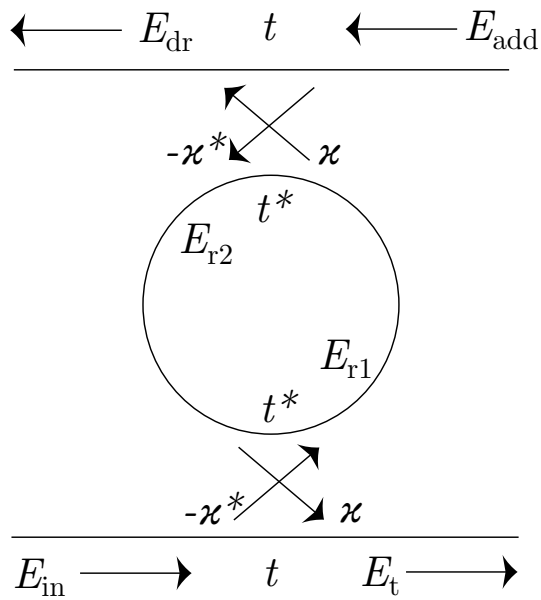

Figure 2-7: Schematic of ring resonator couplings to bus and drop waveguides as used in nonlinearity measurements.

Here α is again the intensity-dependent loss, as in the previous section, assumed to be constant over the ring, and $\theta = \frac{n_{\mathrm{eff}}\omega}{c}$ is the round-trip phase shift through one passage around the ring, defining the resonance condition. With the input and through powers proportional to $|E_{\mathrm{in}}|^2$ and $|E_{\mathrm{t}}|^2$, solving this nonlinear system allows calculation of the peak extinction on resonance. The peak extinctions were measured by scanning a tunable laser input, amplified with an EDFA (aproximately 10 mW maximum before the input grating coupler), and the input power was tuned with a voltage-controlled optical attenuator.

Example through-port transmissions measured are shown in Fig. 2-8. The extinction is measured relative to the off-resonance transmission, and the fact that the refractive index changes and shifts the resonance frequency is accounted for by always measuring the extinction on resonance. Fits to the extinctions obtained from such data as a function of power are shown in Fig. 2-9, for various couplings (set by the coupling gap g between the bus and ring waveguides, which in these devices were equal at both ports) to 20 and 40 μm radius rings. The fits in these calculations assumed no contribution from FCA, and thus can be compared to the y-intercept

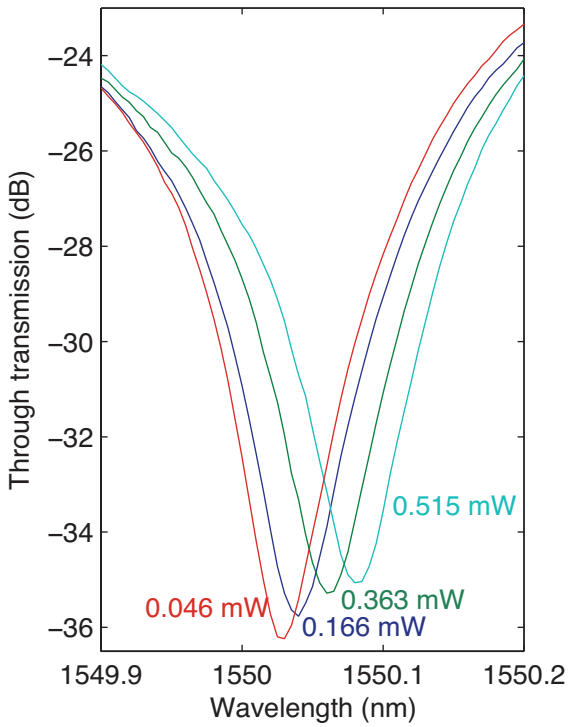

Figure 2-8: Example through transmissions of a ring resonator at various input powers, showing change in resonance extinction.

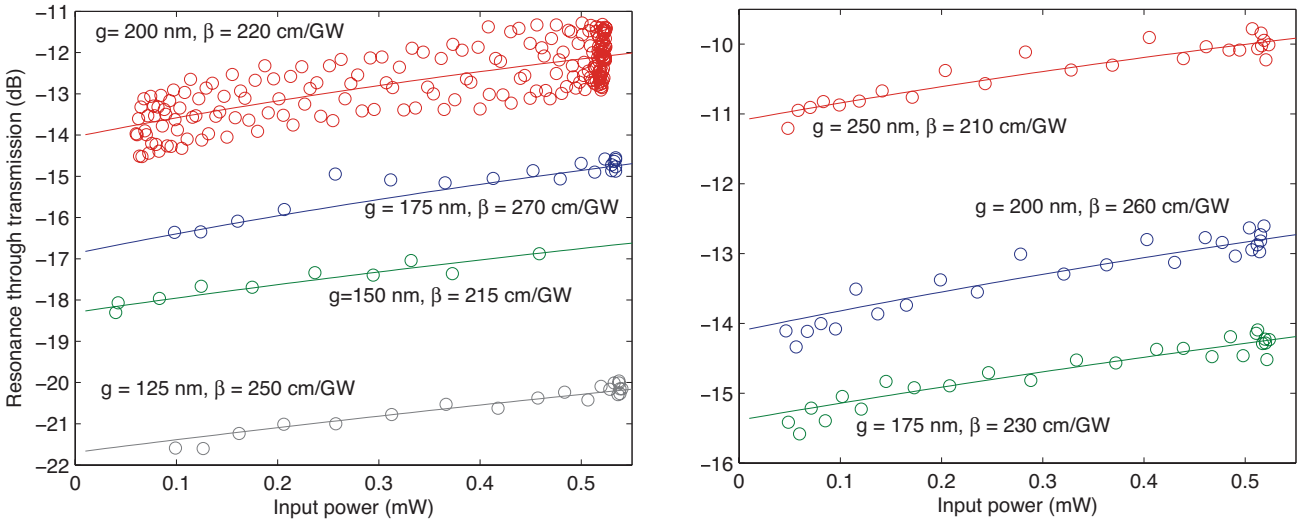

Figure 2-9: Summary of single beam through transmission ring measurements, showing measured extinctions and fits to transmission matrix theory.

in Fig. 2-6. The values are roughly consistent, with these measurements indicating a beta of between 210 and 270 cm/GW. This measurement was presented also in [MOR11], but in that paper the effective area used was that appropriate for linear absorption, which was 30% larger than that for TPA as in the previous section. This correction scales the fitted βs by 77%, and these corrected values are the ones shown here.

This measurement suffers from the same limitation as the lock-in measurement, namely that the inability to separate out FCA from the linear absorption carriers (that were assumed not to be present in this fit, but would yield the same dependence as discussed in the previous section), makes the results difficult to interpret. Nevertheless these results are at least consistent with the lock-in measurements on a ring from the same chip.

2.3.3 Free-space z-scan measurements

A way to reduce the role of FCA with respect to TPA is with ultrafast measurements, using pulses significantly shorter than the free-carrier lifetime (which also sets the time it takes to generate the steady-state free-carrier population), and with repetition rates low enough to prevent build-up of the steady state population. With sufficiently short pulses and low enough peak powers, the role of FCA from TPA photocarriers ($\propto P^3$) can be made much smaller than that from TPA ($\propto P^2$). Free-carrier lifetimes in polysilicon are typically on the order of 100 ps, so their contribution to attenuation of a 100 femtosecond pulse with peak power P_{pk} is roughly a thousandth that compared to CW P_{pk}.

A standard technique to measure the nonlinear absorption with ultrafast pulses relies on focusing the output of a mode-locked laser, and measuring the transmission of the beam as the sample is scanned through the focus in space [SBSW04]. If only linear absorption were present, no change in transmission would be observed; in the case of nonlinear absorption, loss will peak and transmission will dip when the intensity in the sample is highest, at the focus.

In a thin sample such that $L < z_0$, z_0 being the Rayleigh range of the focused

gaussian beam, the intensity is assumed to be constant throughout the sample. Then the transmission of the femtosecond pulse with a gaussian temporal profile, focused down to some minimum beam waist w_0 and $z_0 = \pi\lambda^2/w_0$, through the sample as a position of the sample position z can be simply written as [DQG03]:

$$T = 1 - \frac{1}{2\sqrt{2}} \frac{\beta I_0 L}{1 + \left(\frac{z}{z_0}\right)^2}; \tag{2.15}$$

here $I_0 = P_{\text{pk}}/2\pi w_0^2$ is the on-axis peak intensity at the beam's focus, the $1 + \left(\frac{z}{z_0}\right)^2$ accounts for the change of this peak intensity in the sample as a function of sample position, and the $1/2\sqrt{2}$ prefactor accounts for the approximately gaussian spatial and temporal profile. The transmission here is normalized to the low-power transmission, and the effect of multiple reflections within the sample is neglected.

The measurements here used a commercial mode-locked fiber laser around 1550 nm (by Menlo Systems) which output pulses with lengths of approximately 170 fs at a 200 MHz repetition rate. The average power measured out of the laser on a calibrated HP power head was 145 mW, which, for sech^2 pulses, translates to a peak power of approximately $P_{\text{pk}} = 0.88E_{\text{pulse}}/\tau_{\text{pulse}} = 3.6$ kW (E_{pulse} is the pulse energy, τ the pulse time). The reflection coefficient between silicon and air for normal incidence is $\left(\frac{n_{\text{Si}}-1}{n_{\text{Si}}+1}\right)^2 \approx 0.3$, meaning that the peak power in the sample is about 2.6 kW. However, the higher group index of the sample also increases the peak power over that in air proportional to $n_g = 3.5$ for Si; thus, the peak power in the sample is calculated to be 9.1 kW for a silicon slab.

One of a few measurements on crystalline samples are first shown in Fig. 2-10, to establish the setup. This measurement was performed with an 18.4 mm focal length aspheric lens. As aperturing of the collected light was not desired, a collecting lens was usually placed between the receiving power head and the sample on the other side, to allow the bulky detector to sit at a distance from the sample; in this case the collecting lens was a 25 mm spherical lens. The output of the laser was somewhat divergent and not exactly known at the entrance to the focusing lens, but the 9μm

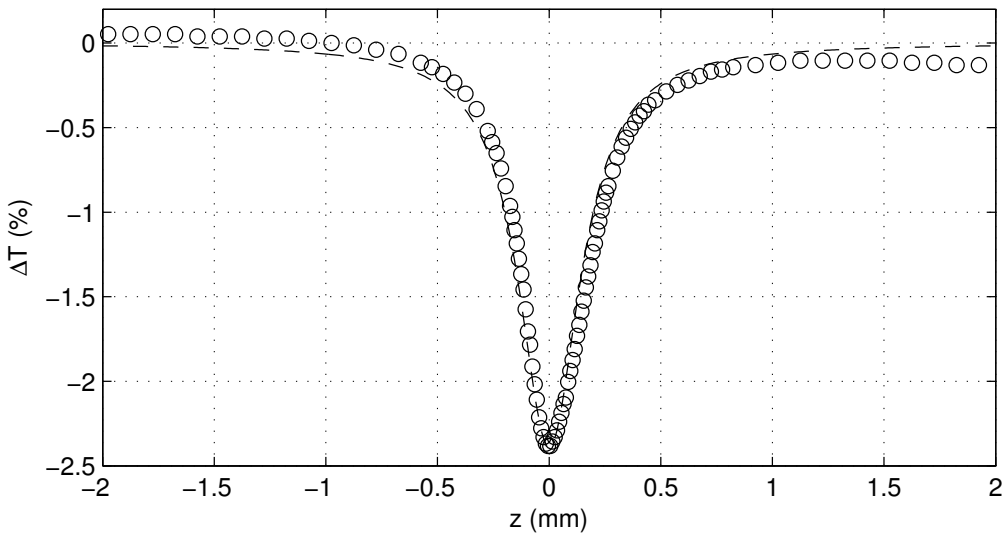

Figure 2-10: Example z-scan measurement performed on a double-side polished crystalline silicon substrate, showing fractional change in transmission through the beam focus at $z = 0$, and fit; the sample thickness was 250 μm, $w_0 = 9\mu$m, and the fitted $\beta = 1.57$ cm/GW.

w_0 used to fit the data is consistent with a beam diameter at the lens, based on $w_0 = \frac{\lambda F}{D}$, of 3.2 mm, which is in the expected range. In measurements taken with lenses of different focal lengths, the beam waist was expected to scale approximately as expected with the focal length.

The β from the fit is around twice that of the literature value; this is most likely due to the uncertainty in the laser's peak power, and also likely due to dispersion through the focusing lens, which was not characterized in this measurement. Similar fitted βs were also obtained for a thicker sample of around 750 μm.

The polycrystalline samples were substantially thinner, at only around 120 nm (for the early sample, as used in the ring measurements of the previous sections), and about 200 nm for later samples from Micron. This meant that much lower focal lengths were used (around 3 mm) to achieve a stronger signal. Fig. 2-11 shows the first measurement on this sample, using a 2.97 mm focal length lens. The data exhibits an asymmetry around the main dip, which is similar to that observed in measurements in which the transmitted light is sent through an aperture [SBSW04]. For this preliminary data, this apparent unintentional aperturing was ignored and

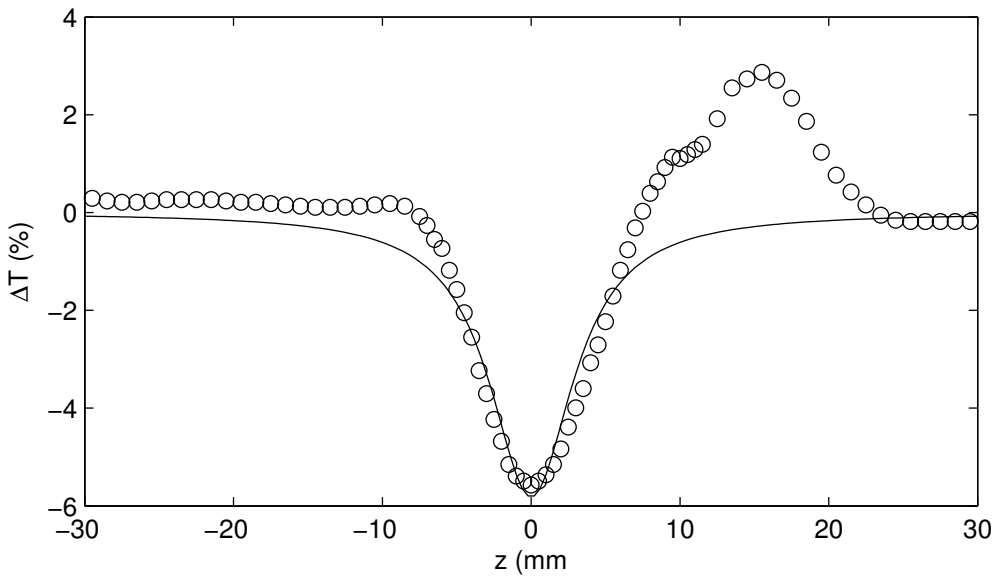

Figure 2-11: Original z-scan measurement on 120 nm-thick polysilicon film of same deposition as used in the ring measurements above. The fit used $\beta = 160$ cm/GW, although it is possible this feature arose from damage to the sample, as discussed in the text.

the fit to the dip indicated a β of around 160 cm/GW, which roughly agreed with the ring measurements.

However, when later trying to reproduce this measurement, black spots that appeared in microscope images of the samples after the measurement made it clear that powers being used from the laser were capable of damaging this thin film, which would result in transmission dips of comparable size being observed even when the laser power was attenuated. That is, once the sample was damaged by high power pulses, as might occur just in the first attempt at a scan, subsequent scans through the same point on the sample might only measure the scattering or linear absorption, which is largest at the focus since here the most light passes through the damaged region. The power being used in Fig. 2-11 was not far above the damage threshold, for later measurements showed that attenuating the laser with a 0.5 ND filter, or using a 4.5 instead of a 2.97 mm focal length lens, reliably stopped damage from occurring. Based on this it is likely, but not completely clear, that damage of some kind was responsible for the feature in Fig. 2-11; in later measurements, when the sample was

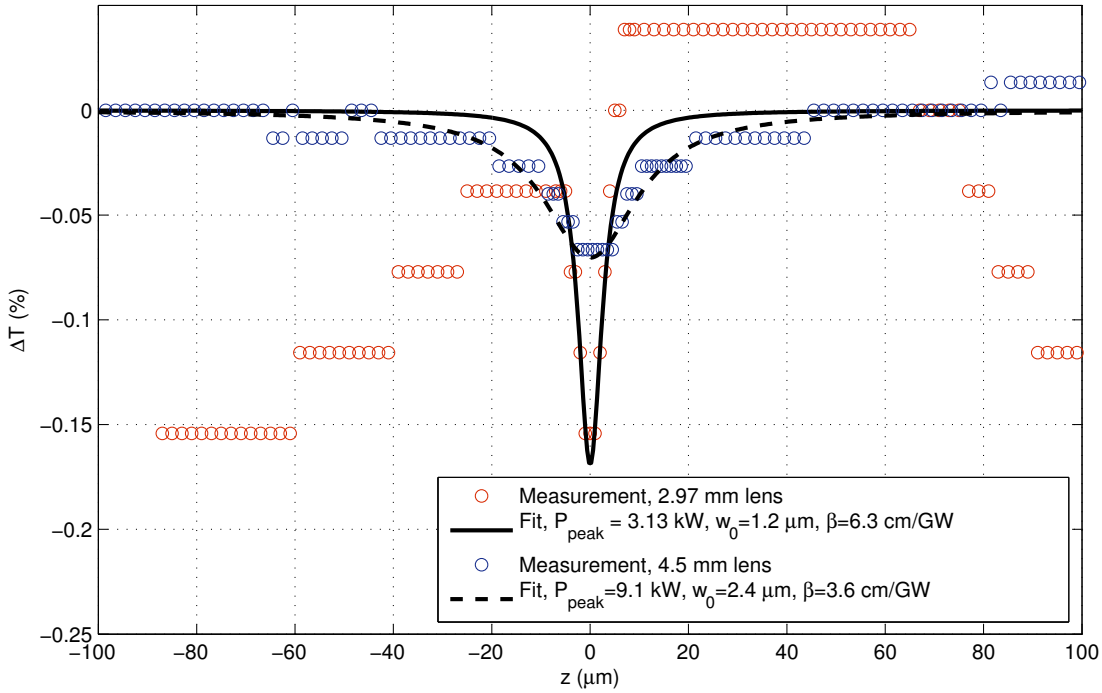

Figure 2-12: D0 z-scan measurements with two different focal length lenses, and fits; the different peak powers assumed are due to the fact that with the shorter focal length lens, a 0.5 ND filter was used to prevent sample damage.

scanned laterally through the laser's focus, almost the entire sample was damaged and further measurements were impossible. These samples required a substrate etch, which was performed only on one of each material sample.

What can be said is that, even if the original material did have a TPA coefficient on the order of 100 cm/GW, later depositions did not; Fig. 2-12 shows data from two films from a later Micron deposition (D0), which showed weaker transmission dips. Here, to avoid damage when using the 2.97 mm focal length lens, a 0.5 ND filter was inserted before the sample. These measurements indicate a β not larger than a few cm/GW. However, a small amount of third-harmonic, visible green light was observed in the transmitted light, which for TPA dips this small could contribute to the dip, and makes measurement of TPA in samples this thin and with a low β difficult. One green photon produces only one e-h pair in the detector, whereas the infrared photons would have produced three, which results in a lower photocurrent, and hence inferred

power for a given amount of green power as opposed to infrared. Indeed, the fact that the different measurements gave substantially different βs indicates this played a role. If the films were thicker, weaker and less tightly-focused beams could be used, which, due to the different scalings of third-harmonic generation and TPA, would allow an increase of the relative importance of TPA. However, this was not possible for such thin samples with βs not substantially larger than cSi's. I further note that a rough calculation indicates that the contribution of TPA to absorption of this pulse should be about 10× that of FCA, though uncertainty in the FCA again makes these measurements upper bounds.

The optimal way to conduct these measurements, given the film thicknesses, would be an ultrafast measurement of the nonlinearity within long waveguides, as in [MNK+12]. Such measurements have not been attempted as of the time of this writing but are expected to yield a more definite answer as to the strength of the TPA process in these pSi samples.

2.4 Steady-state model for detection efficiency in a resonator

So far, this chapter has dealt with the material properties of the absorbing region. This section presents a model for the detection efficiency of a resonant two-photon absorption detector, for a few different values of β.

To predict the detection efficiency in more detail than provided by the basic scalings discussed in the previous chapter, a simple rate equation model for the photon and electron density in the resonator is used; the same approach is taken in [TST+10] (although they approximate the mode volumes relevant to the different order processes as the same). With u representing the energy in the resonator, and N the volume-density of electon-hole pairs, their time evolution with some input power P_{in}

is described by two coupled rate equations:

$$\frac{du}{dt} = P_{in} - \frac{\omega}{Q_l}u - \frac{c^2\beta}{n^2V_2}u^2 - \sigma\frac{c}{n}Nu \tag{2.16}$$

$$\frac{dN}{dt} = \frac{2c\beta\lambda}{hn^2V_3^2}u^2 + \frac{\alpha_l\lambda}{hnV_2}u - \frac{N}{\tau_r} - \frac{I}{eV_2}. \tag{2.17}$$

Here the terms in the equation for $\dot{u}$ correspond to power dropped into the cavity, power lost by all the cavity's linear loss mechanisms (Q_l), loss from two-photon absorption, and free-carrier absorption from photo-generated carriers. Here β the TPA coefficient, in units of length over power. $\dot{N}$ is the sum of terms corresponding to excitation by TPA, linear absorption (OPA) characterized by an absorption coefficient α_l, recombination with lifetime τ_r, and removal through the current generated by an applied voltage. Factors of c/n, appear in the conversion of coefficients describing bulk silicon's loss rates per unit *length* to loss rates per unit *time* – e.g., the FCA loss coefficient per unit length, $\sigma N \rightarrow \sigma N\frac{c}{n}$, and $\beta I = \beta u\frac{c}{n} \rightarrow \beta u\frac{c^2}{n^2}$, and thus n represents bulk Silicon's group index (taken to be 3.5 at 1550 nm). $I = \frac{eA\mu\phi}{d}N$ represents the photocurrent, with A the cross-sectional area of the absorbing region, μ the carrier mobility, d the distance between electrodes, and ϕ the applied voltage.

The effective volumes relevant in the rate equations are given by:

$$V_2 = \frac{\left(\int \mathrm{d}V\epsilon\mathbf{E}^2\right)^2}{\int \mathrm{d}V\epsilon^2\mathbf{E}^4}. \tag{2.18}$$

$$V_3^2 = \frac{\left(\int \mathrm{d}V\epsilon\mathbf{E}^2\right)^3}{\int \mathrm{d}V\epsilon^3\mathbf{E}^6}; \tag{2.19}$$

The first serves to describe two-photon absorption and FCA from carriers excited by linear absorption (both of whose rates go as u^2), and the second describes FCA from TPA-excited carriers (whose rate goes as u^3) [BSP05]. For a oxide-clad silicon three-hole cavity (to be described in the next chapter), these values are found to be, in units of $(\lambda/n)^3$, approximately 2.2 and 1.4, found from FDTD simulation.

Below, I solve these equations in steady state and plot the fraction of input power absorbed via TPA over total input power (i.e. the TPA absorption efficiency) vs. the

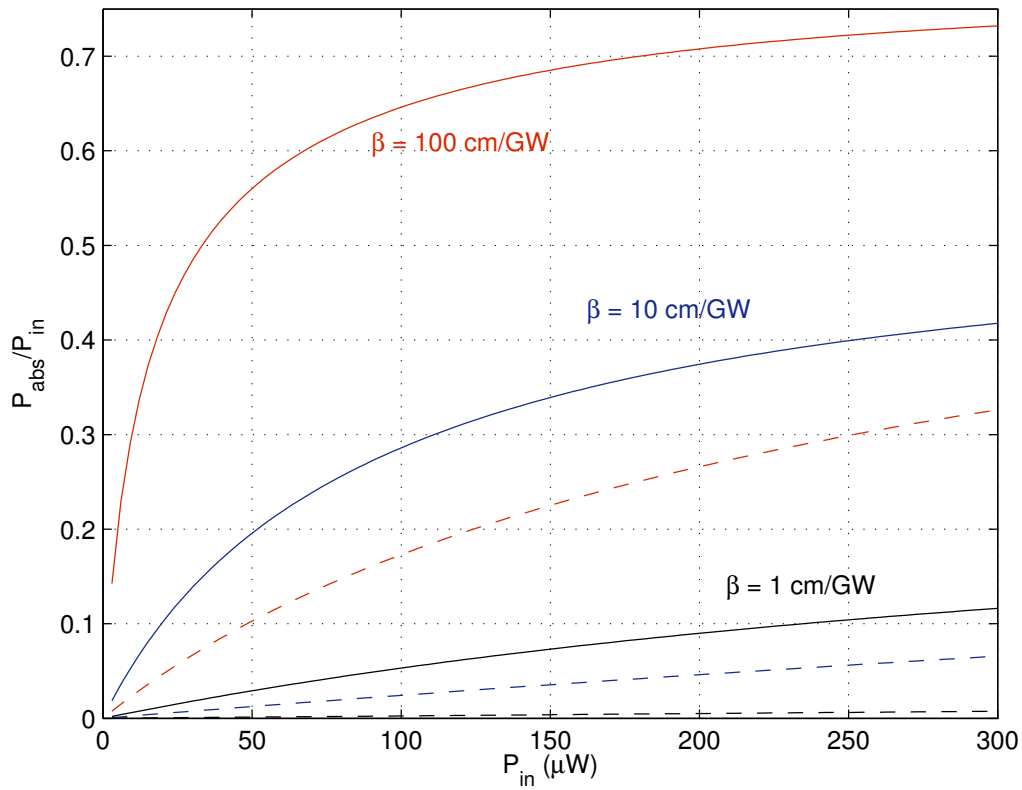

Figure 2-13: Predicted energy efficiency of TPA in a pSi microresonator vs. input power; colors represent three different values of β as labeled, and the dotted lines assume a cavity Q of 10,000, and the solid lines assume 50,000. The model and other parameters used are described in the text.

input power, for different values of the resonator Q, as well as the TPA coefficient β, assuming the following parameters: $\tau_r = 100$ ps, $\phi = 1$ V, $A = 2$ μm^2, and $d = 3$ μm. A linear absorption loss coefficient $\alpha = 5$ dB/cm was assumed, along with a mobility one order of magnitude lower than cSi's as a conservative estimate for good polycrystalline silicon.

These efficiencies at low powers (so that the efficiency is linear in P_{in}) are proportional to $1/V$; other resonator designs can enable mode volumes of approximately a third of the three-hole design with similar or comparable Qs.

The estimate of $Q = 50,000$ is reasonably ambitious for a cavity in a CMOS process, and hence these curves show that, for 100 μW input, with Si's TPA coefficient, TPA efficiencies of greater than 5% are likely to be quite challenging, though with

enhanced TPA significantly higher efficiencies can be possible. Any free carriers from linear absorption were left out in these curves, and in polysilicon these could also contribute a significant photocurrent; essentially, if the material absorption forms a large fraction of the total cavity decay rate, one would expect an appreciable photocurrent from linear absorption itself. These considerations together motivate study of small mode-volume resonators as detectors in this environment.

2.5 Conclusion and summary

This chapter discussed the basic physics of TPA in crystalline Si, a model for linear absorption in pSi, and reasons for possible enhancement. Measurements of the nonlinear absorption in pSi waveguide devices were discussed, with the β required to explain the results given a range of assumptions about FCA. The rate equation model presented finally gives an estimate for the TPA contribution to resonant photodetector performance for a range of parameters; the next section will discuss design and measurements of the resonators.

Chapter 3

CMOS Photonic Crystal Devices

This chapter presents the work done to design photonic crystal resonators in standard CMOS flows, primarily focusing on Micron's DRAM process, and optical characterization of fabricated devices. Here, design consists of simulation and optimization of a few different resonator types with the dielectric layer structure appropriate for the process flows used, appropriate design of couplers between the cavity and waveguides, as well as provisions for electrical contact to the resonator.

The first part of this chapter presents a short qualitative overview of the different types of resonators designed and created in this thesis, and a comparison of their advantages and disadvantages. The simulation results that guided design, and optical measurements on cavities fabricated through the course of this work are presented afterwards.

3.1 Photonic crystal defect designs

A variety of photonic crystal resonator designs have been invented and optimized in the last few decades. All such designs have in common the utilization of the photonic bandgap effect to create a localized state at a defect.

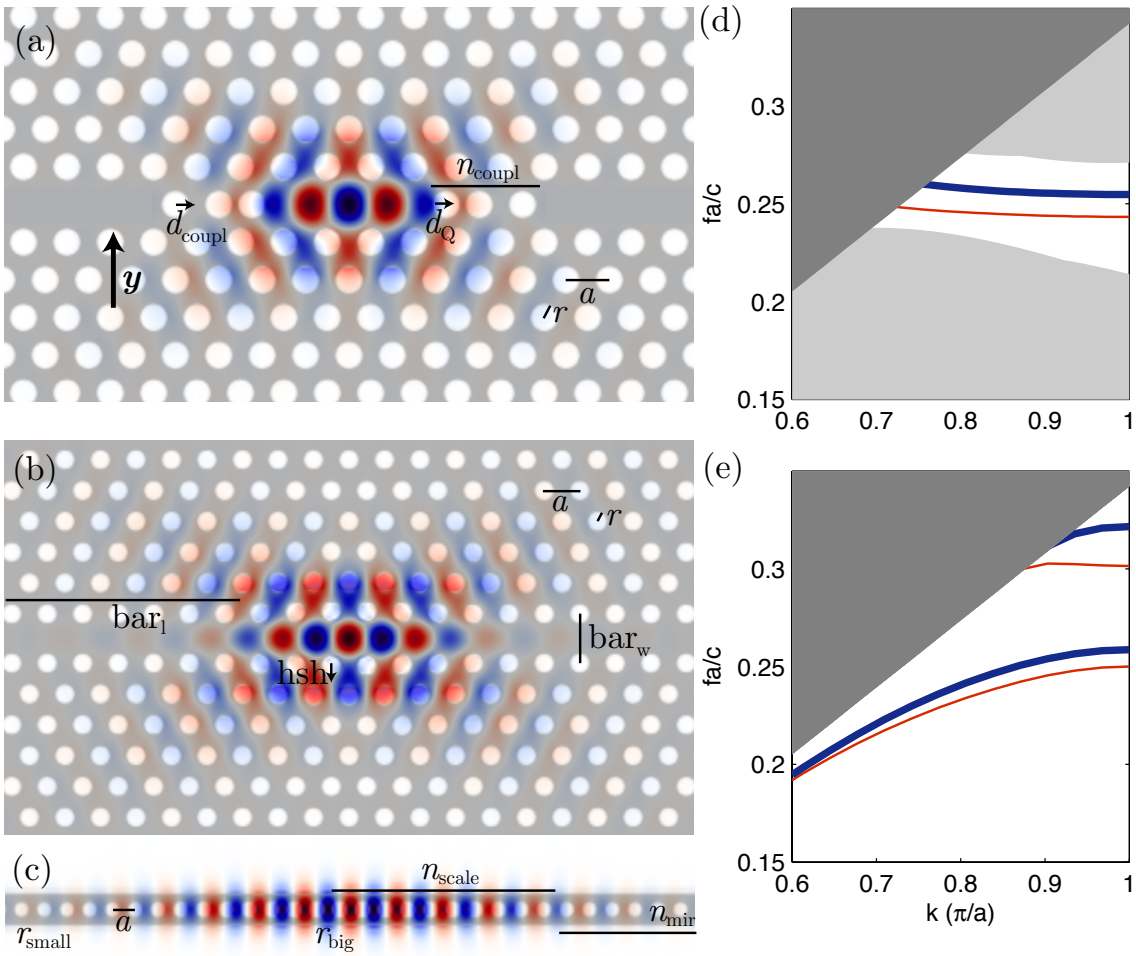

Figure 3-1: Three different photonic crystal designs considered in this work. (a)-(c) show the y-components (direction labeled in (a)) of the electric field of the resonant modes of a 3 hole (a), bulged line defect (b) and tapered 1D resonator (c). (d) shows the dispersion for the fundamental guided mode of line-defect waveguides of to widths. The thick line shows the dispersion for the narrower waveguide, and the thin line for the wider. The region above the lightline is shaded in dark grey, and modes corresponding to bulk modes of the 2D slab are shaded in light grey. The cavity resonance (b) exists near the bottom of the red band of frequencies. Similarly, in (e), the dispersions for 1D photonic crystals of two different hole sizes are shown (larger holes in blue); the highest-Q resonance exists near the upper edge of the lowest blue band.

3.1.1 n-hole defect cavities

The simplest defects are made by simply filling in n holes in a 2D photonic crystal slab; this results in a localized state within the bandgap of the bulk slab. The field profile of such a mode is shown in Fig. 3-1(a). Of the three designs, this allows for the least control over the mode profile, which has relatively abrupt features at the edges of the defect. By the intuition reviewed in Ch. 1, this is understood to limit the radiative Q, which, of the varieties considered here, is the lowest in this type of cavity. This Q can be slightly improved by tuning the parameters of the holes in the immediate vicinity; for example, shifting the holes immediately to the left and right of the cavity outwards from the cavity mode allows for a more gentle envelope function to the mode, and has been shown to substantially increase the Q [AASN03]. This approach is taken here as well.

In devices formed in silicon, clad by air, Qs of tens of thousands have been achieved with 3-hole cavities [AASN03, GPB+09]

3.1.2 Width-modulated line-defect cavities

A more subtle scheme to achieving confinement results from gradual transitions between PC WG modes with different parameters. The bulged line-defect [KNM+06] is one such cavity; Fig. 3-1(d) shows the relevant bandstructure. Here the thick and thin curves show the dispersions of the fundamental modes of PC line-defect waveguides of two different widths (the wider in the thin line); as one gradually transitions from a wide to narrow waveguide, light at a given frequency in the wide waveguide approaches cutoff at $k = \pi/a$, where it can couple neither to the cladding modes, the 2D slab modes, or the guided mode of the narrow waveguide, and is therefore nearly perfectly reflected in a sufficiently gradual transition. This method allows for much more gradual mode profiles than the n-hole defects, and thus higher radiative Qs.

In silicon/air cavities, these designs allow for Qs far exceeding those of 3-hole cavities, reaching over 1 million [TNK+06] in the best devices made, albeit with somewhat higher modal volumes. In both cases, electrical contacting is straightfor-

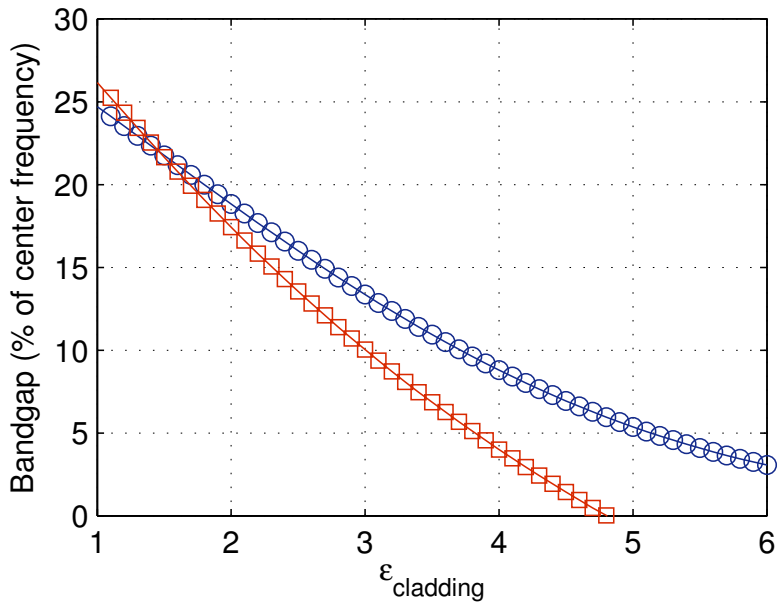

Figure 3-2: Si-core ($\epsilon = 12.25$) photonic crystal bandgaps plotted as a function of cladding index, for a 2D triangular lattice with $r = 0.3$a and a slab thickness of 0.5a (squares), and for a 1D crystal with the same radius and thickness, and a waveguide width of $1.5a$ (circles)

ward, as dopants can be introduced into the patterned region above and below the cavity mode.

3.1.3 1D tapered hole cavities

For materials with low index contrast, bandgaps in a 2D crystal decrease faster than for a 1D array of holes (as shown in Fig. 3-2, and hence cavities utilizing PBG confinement in 1 dimension only (and TIR in the other two) are advantageous, particularly with these material constraints. A few different methods of producing a gradual defect have been explored – tuning the lattice constant, hole radii, or waveguide width, though conceptually these are all the same. I consider tuning the hole radius and [CECP09].

The relevant dispersion is shown in Fig. 3-1(e); the dispersion of 1D waveguides with two different hole radii (larger in blue) are shown; the lower band corresponds to modes localized primarily in the core, and the upper band with more field in the holes.

Resonant modes based on band modes farthest from the lightline yield the highest Qs, so the lowest band is used. Similarly to above, as one transitions gradually from the large to small holes, light at the upper edge of the large hole region's dispersion reaches cutoff at $k = \pi/a$ and is reflected. A linear taper in the hole radius over a few periods gives rise to an almost Gaussian envelope function, giving rise to very low radiative loss [QL11]. The resulting mode profile is shown in (c).

1D cavities have the advantage of allowing Qs of many hundreds of thousands in relatively low index-contrast platforms, and with comparable mode volumes. The only significant downside is that contacting such a cavity is less straightforward than with the 2D cavities.

3.2 Micron D0 crystals

Two designs were drawn for fabrication at Micron over the course of this work, on chips that were termed (as per the colorful and illuminating parlance of the larger project) D0 and D1S. The two chips were separated in time by about a year. Important facts about the fabrication were learned from the first chip (D0), which allowed for significantly higher quality devices when applied to designs on D1S.

This section describes the considerations that went into the design of 3 and 5 hole cavities and line-defect resonators on D0, and then what was learned from the fabricated devices.

3.2.1 Simulation, design

The geometries considered were simulated in MEEP [ORI+10], by exciting the cavity with a broadband pulse from a point dipole, allowing the fields to decay until the resonant mode is the primary remaining field, and determining the resonant frequency and Q from the oscillations and decay of the field via the harminv routine, developed by Steven Johnson and based on the algorithm in [MT97].

For 3 and 5 hole defect cavities, the design consists of a choice of a, r, d_Q, coupling holes, and d_{coupl} (labeled in Fig. 3-1), for the purposes of ensuring cavities existed near

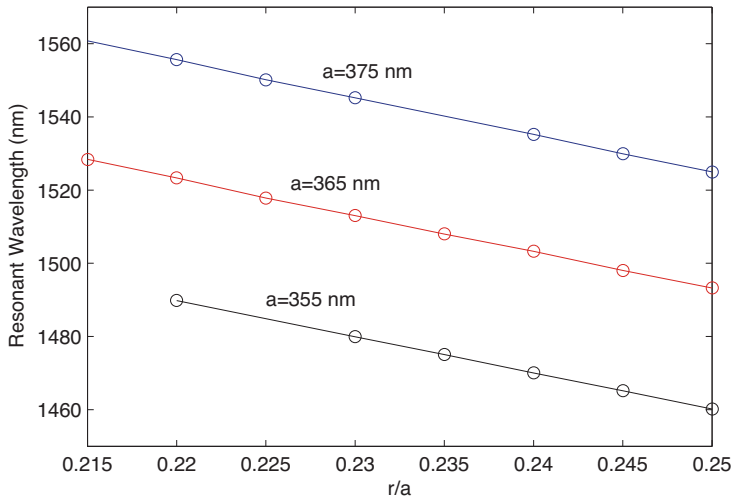

Figure 3-3: Dependence on lattice constant and radius of oxide-clad 3 hole resonators.

the desired wavelengths, broadly over the range of 1400-1570 nm, and for maximizing Qs. For the preliminary D0 cavities, these simulations were done assuming an oxide cladding; the full dielectric stackup in this new process was not known at the time of these designs.

The lattice constant a has the strongest influence over the resonant frequency of the cavities; fig. 3-3 shows the resonant frequency as a function of r (as a fraction of a) for a few different as for 3-hole cavities, with a pSi slab thickness of 220 nm. Variants of devices with a between 335 and 395 nm were thus included to assure some devices in the desired frequency range.

The value of hole radius is important in setting the Q for a given lattice constant. As r decreases, the bandgap and hence the strength of the PBG reflection goes down, slightly reducing the confinement and increasing the Q. At some point, the bandgap no longer exists, and the Q starts to drop drastically, which happened below approximately $r/a = 0.22$. Here, resonant intrinsic Qs of around 25,000 were possible at maximum; the Q drops off to about 10,000 at $r/a = 0.25$. For the three-hole cavities, a large range of rs was specified in the designs, between 0.22 and 0.28. However, for the 5-hole and line defect cavities, only variants with radii at the lower end of this range were included.

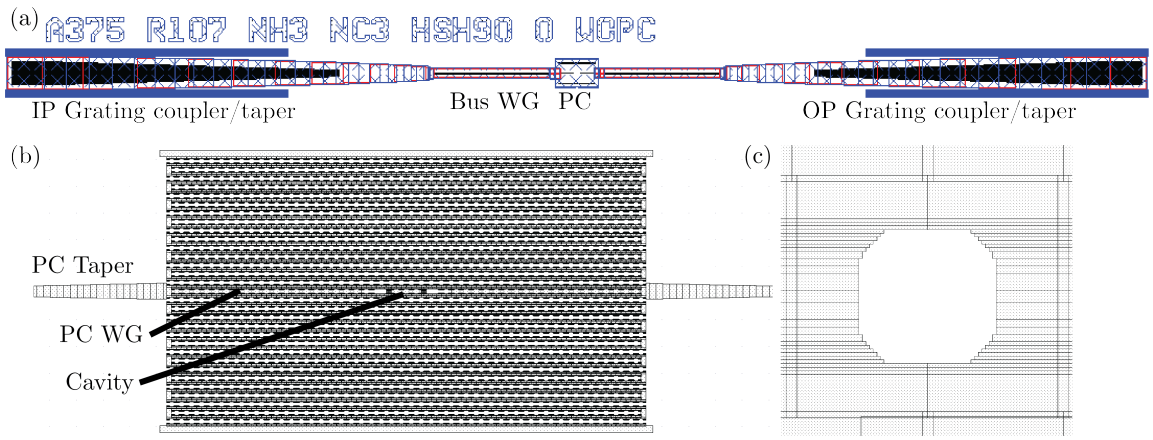

Figure 3-4: Images of mask designs for a single device, showing (a) full view of inputs and outputs, with the PC in the center; (b), a close-up of the PC region, showing taper connecting the bus WG to the PC WG, and the cavity symmetrically coupled to the PC WGs; and (c), showing a single hole, with edges filled to accommodate OPC algorithms.

The goal of the coupling was to achieve detector variants (with loading only from the input side) with a loaded Q of around $Q_0/2$; this was generally observed to happen in the 3-hole cavities for $n_{\text{coupl}} = 3$, though for the 5 hole cavities it was closer to $n_{\text{coupl}} = 2$. Variants with both were included for both types.

The considerations were of course the same for the line-defect cavities, except the achievable Qs were higher (up to about 100,000 with the oxide cladding). However, like in the 5-hole defect cavities, the variants did not include hole sizes with the upper end of those on the 3-hole cavities, which led to poorly performing devices, due to the process bias in the holes.

Fig. 3-4 shows the mask layout for a typical device; grating couplers on either side couple light in and out vertically from bus waveguides (simple rectangular Si geometries) through a taper. These bus waveguides are connected to the PC WGs via tapers, visible in (b), which expand to a width of $1.6a$ (roughly the width between the centers of the holes surrounding the PCWG) and have been shown to allow for low insertion losses around 1dB [MB03, MMV03].

In CMOS processes the mask is drawn as a series of rectangles, so each hole is discretized accordingly. Micron's process involves an optical proximity correction (OPC) procedure. One of the requirements of the algorithm was that no poly rectan-

gles would be separated by less than 80 nm; thus, at the tops and sides of the holes, where these spacings were less than 80 nm, the rectangles were extended, slightly "clipping" the holes (to extents not likely to change the circularity of the fabricated features), as shown in Fig. 3-4(c).

3.2.2 Fabrication of holes

The devices were patterened by Photolithography in a commercial DRAM process at Micron, using 193 nm illumination from an ArF laser and a 0.68 numerical aperture. Since this was the first time fabricating approximately 100 nm radius holes by photolithography in this process, a major part of what was learned from this run was simply the relation between the fabricated hole size and the specified one. 3 hole resonator variants with lattice constants ranging between 335 and 395 nm in increments of 10 nm were included, with seven different radii at each lattice constant; this allowed for a thorough characterization of hole sizes by SEM, including potential effects of different lattice constants.

Fig. 3-5 shows a wide-field SEM of some device variants (text labels show a and r, in nm). Fig. 3-6 shows a close-up of two patterned regions. Almost all the variants showed the expected pattern, as in the left image; only the device with the smallest hole radius specified resulted in holes that failed to form, presumably due to incomplete development etching of the photoresist for very fine features. The specified radius here was 75 nm, and the measured physical average hole radius was about 53 nm, which should correspond to a lower bound of what is possible in this process. All viable designs required significantly larger holes, so this never resulted in a real constraint.

The holes in a number of images like Fig. 3-5 were fit by MATLAB's circle-finding algorithm. Fig. 3-7 summarizes the results; each color of points corresponds to one lattice constant, and the different hole radii included at that lattice constant are plotted on the x-axis, vs. the average measured radius, with error bars given by the standard deviation of the physical holes. An approximately linear trend was observed relating the fabricated and specified radius, and no dependence on the lattice constant

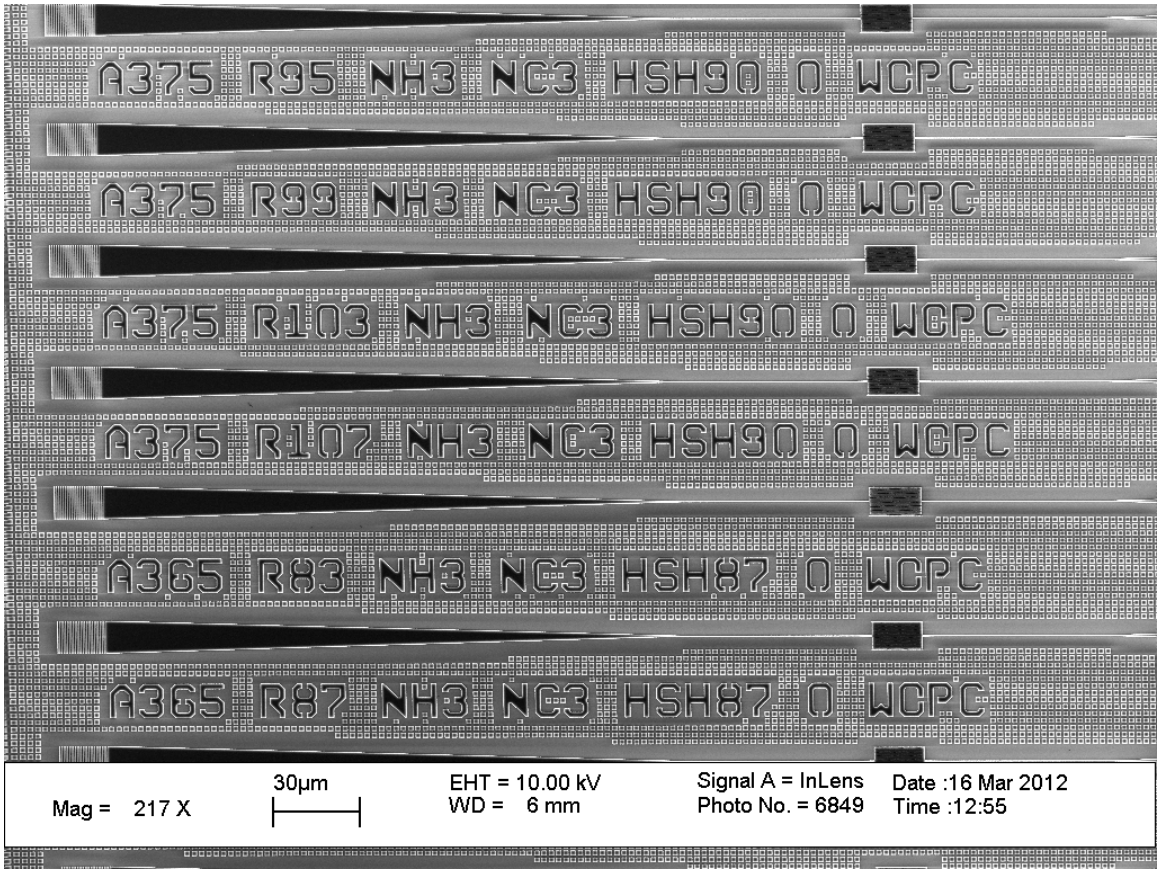

Figure 3-5: SEMs of 3-hole resonator variants included in D0, showing grating couplers for light coupling, bus waveguide coupling to the photonic crystal region.

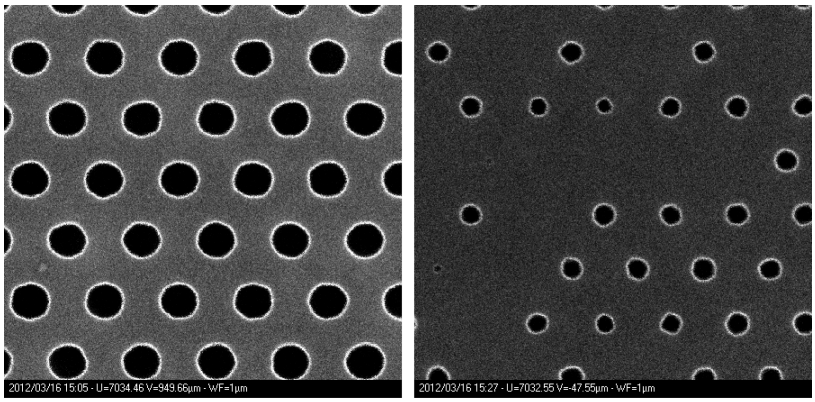

Figure 3-6: SEMs of photonic crystal regions near 3-hole resonators. On the right is a typical example (a=375 nm, specified r = 107 nm); this kind of uniformity was seen in all devices, except for the devices with the smallest hole radius specified (75 nm). Here, as shown on the left, many of the holes did not form.

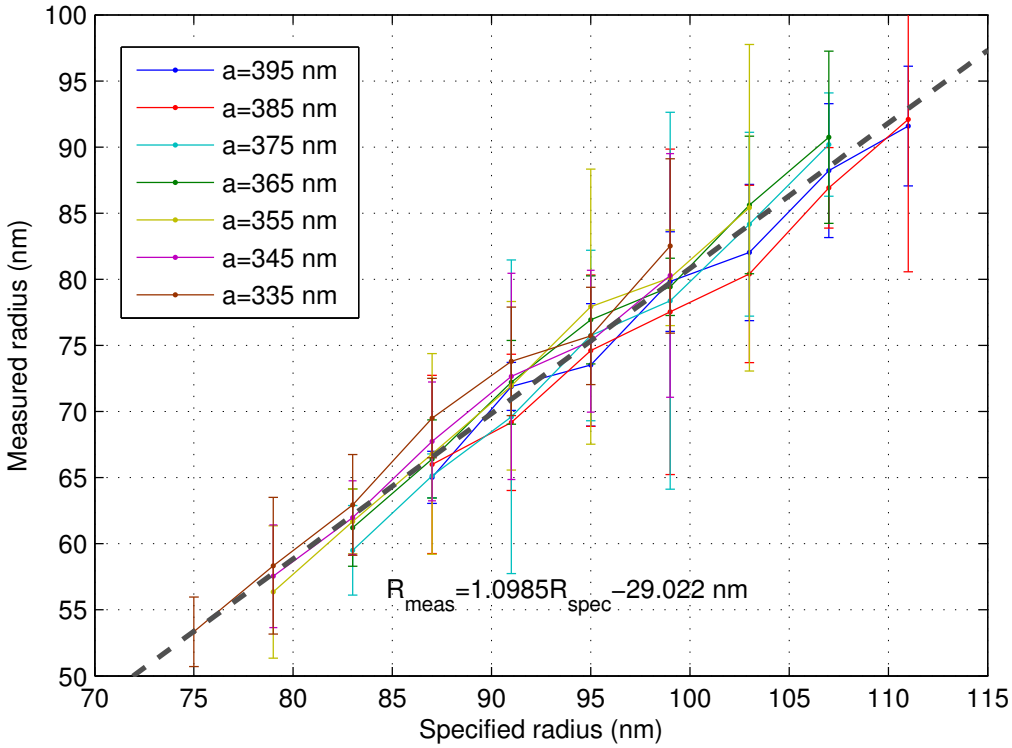

Figure 3-7: Expected hole radius from lithographic contour simulations following application of optical proximity correction to the designs sent to Micron, along with measured radii from SEM. The linear fits were used in subsequent designs.

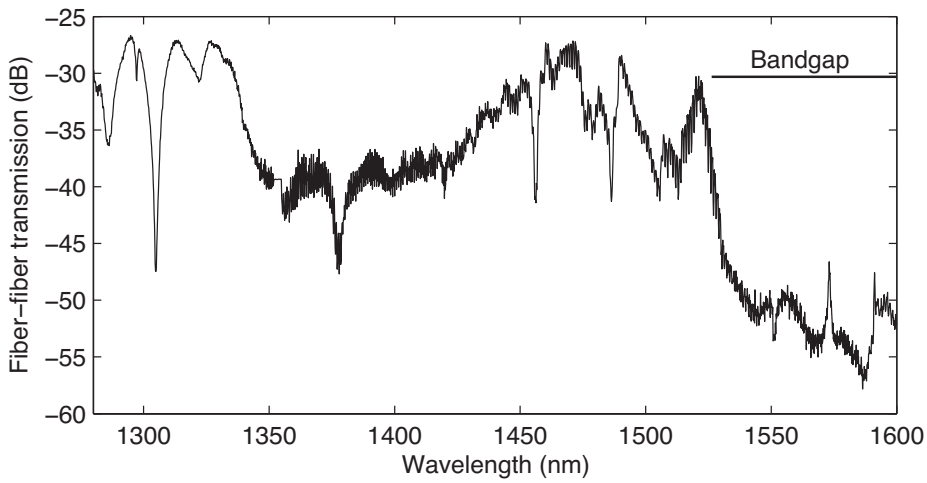

Figure 3-8: Broad transmission scan through a 3-hole device from D0 ($a = 375$ nm, $r_{\text{spec}} = 95$ nm. The high-frequency edge of the bandgap is around 1525 nm, and the transmission peak at 1570 corresponds to the 3-hole resonance.

was observed; this gave a simple way to compensate for these offsets in future runs (D1S, below).

However, for D0, the fact that the hole sizes emerged to significantly smaller (approximately 20-25% on average), significantly limited what was observable in the fabricated resonators.

3.2.3 pSi three-hole resonators

Broad wavelength scans were done at first to identify the cavity resonance frequencies. Fig. 3-8 shows one example; in this device, the high-frequency edge of the bandgap lies at around 1525 nm, and the cavity resonance appears as a transmission peak near 1570 nm. This scan was taken with a Santec tunable laser module, which actually consists of four independent lasers whose polarizations are not matched; here, polarization is approximately TE between 1480 and 1580 nm, but for other wavelengths other modules were used with potentially different polarizations. The polarization had to be adjusted to be TE to be able to see the resonances, which was done in these samples by minimizing transmission in the bandgap.

The largest hole size variations were included for the 3-hole resonators, and hence

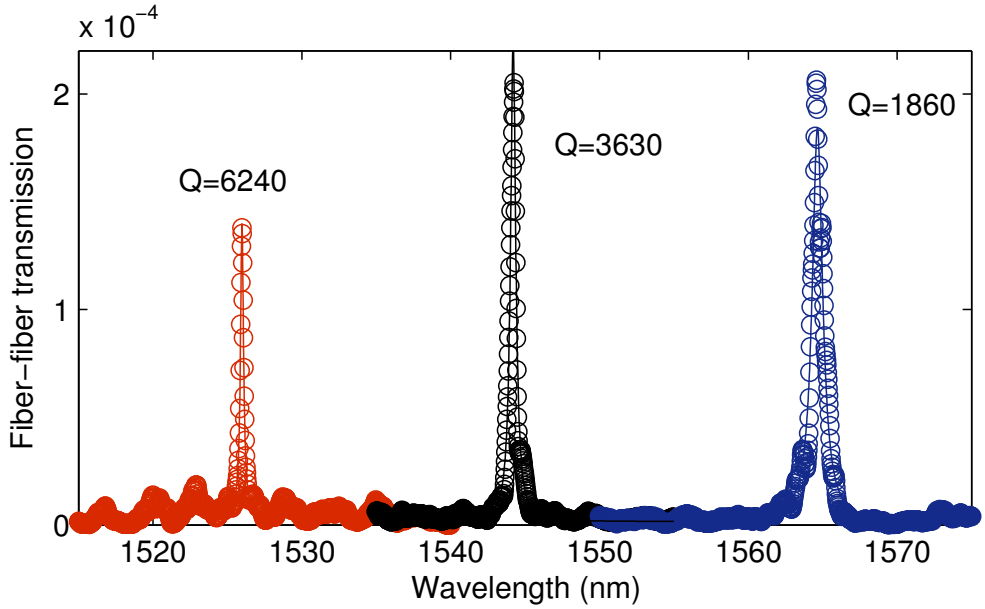

Figure 3-9: Transmissions through three-hole pSi resonators of three different radii (107, 103 and 99 nm, from low to high λ) in oxide cladding, from the short flow wafers of D0; lattice constant is 375 nm.

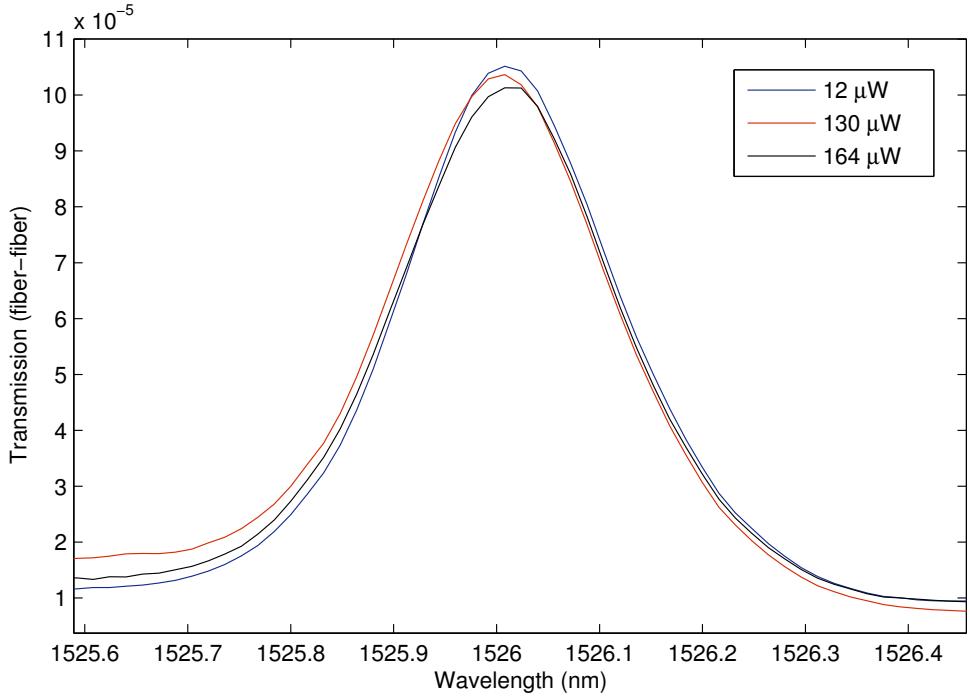

Figure 3-10: Power-dependence of transmission through the $a = 375$ nm, $r = 85$ nm 3-hole cavity in D0. Intensities in waveguide after the input grating coupler are labeled. A weak blue shift of the resonance, attributed to free-carrier dispersion, followed by a thermal red-shift are visible.

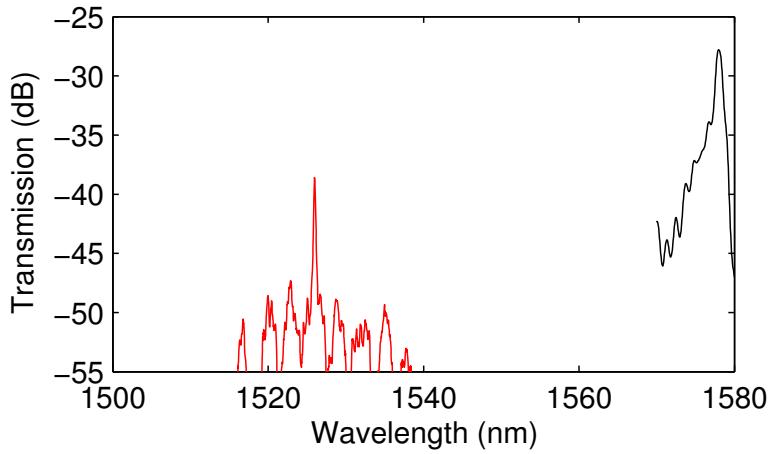

Figure 3-11: Transmission scans on the same resonator geometry as above, compared for the oxide-only wafers and the full-flow wafers including the nitride of the full dielectric stack. Both the resonance redshift, and the significantly reduced Q, are explained by the additional high index SiN near the crystal.

in this run only these resonators yielded Qs over 1000. Fig. 3-9 shows the transmissions measured through three resonators with different radii, all from a "short-flow" wafer which included only the patterned poly, clad in oxide. The highest Q measured near 1550 nm is 6240 (from a Lorentzian fit of the transmission function), which occurred in the device with lattice constant of $a = 375$ nm and a physical hole radius of 85 nm.

These devices exhibited only a weak optical nonlinearity (Fig. 3-10), due to the relatively low Q as well as the limited power we could couple into the devices.

The fully processed devices (with the fabrication steps needed for doping implants and contacts) had, in addition to the oxide cladding, a nitride layer which both filled the holes and top of the waveguide; the top nitride was very thick, at 170 nm. The impact of this was to substantially decrease the cavity Qs due to the further reduced index contrast, and was observed here to reduce the cavity with Q=6240 to only approximately 1000, as measured in transmission (Fig. 3-11).

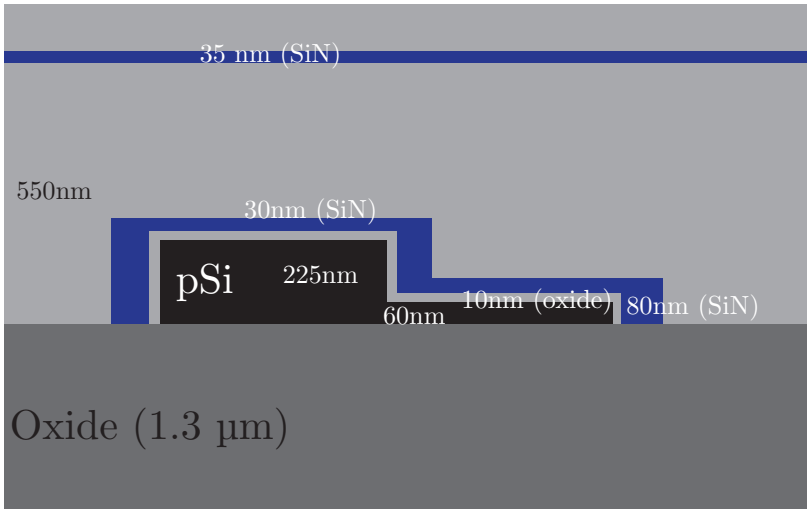

Figure 3-12: Dielectric layers near the polysilicon in the D1S chip; the bottom oxide sits on a silicon substrate.

3.3 Micron D1S crystals

D0 successfully allowed calibration of the process offsets affecting realized hole sizes, which was accounted for in the subsequent set of designs to Micron (D1S). Additionally, understanding the effect of the inclusion of layers like SiN near the silicon, additional designs for one-dimensional resonators were developed and included, which as was discussed above are more amenable to low-index contrast environments.

3.3.1 Simulation, design

Designs for this run were done with the full dielectric stackup in mind. This is shown in Fig. 3-12, including the 60 nm wings around the thick 225 nm polysilicon core, resulting from an added partial poly etch step, which allows for contacts to optical devices like the 1D cavities designed for this run. These resonators were designed for this run again because they are known to allow better performance in low-index contrast environments. These designs are theoretically capable of Qs over many hundreds of thousands, but in polysilicon the material ultimately limits the Q; the loss rate per unit time corresponding to a material loss coefficient of α (cm^{-1}) is $\gamma = \frac{\alpha c}{n}$, which for 3 dB/cm, the lowest loss measured in D0, corresponds to about

110,000. This was expected to be an approximate bound on Qs possible in real devices.

The designs for such cavities began by simulating the band structure of the 1D slabs (Fig. 3-1(e)) for the approximate hole-sizes used and waveguide widths; the resonant frequency of the cavity is near the upper band edge of the lower band. Here the resonant frequency can be tuned strongly by both the lattice constant and the waveguide width.

The cavity design is based on linearly scaling n_{scale} holes down in radius from the center of the cavity (where the holes have radius r_{big} outward, and then terminating with n_{mir} holes, each with r_{small}. As n_{scale} increases, radiative Q increase, and the the mode volume increases weakly as well [QL11]; here, n_{scale} was set to be 10 across all designs, although this was a rough choice, and lower values will likely allow for smaller volumes without compromising the (material-limited) Q.

These designs were observed to be robust to a variety of hole size combinations; hole size combinations of $\frac{r_{\text{big}}/a}{r_{\text{small}}/a} = 0.35/0.3, 0.33/0.28, 0.31/0.28$ were all observed to allow for intrinsic Qs of over 100,000 with these materials.

Electrical contacts to these cavities required some thought, since the cavity structure itself doesn't allow for a continuous body of silicon laterally along the cavity in which to implant dopants as in the 2D cavities. The partial-etched wings were used to create this body. The 60 nm slab is thick enough to support a mode with an effective index that can be comparable to that of the PCWG mode in the patterned region, and can as a result introduce a significant amount of radiative leakage. Early in the design, the expected stackup actually called for 100 nm of SiN above the pSi, which increased the effective index of the slab mode enough to almost eliminate the resonances.

Patterning the pSi in the slab region with a 2D triangular lattice maintains the continuous electrical path, but shifts the dispersions of the slab modes up in frequency, closer towards the cladding lightline. For simplicity, the lattice constant of the slab region was kept the same as that in the cavity region. Though the PBG of this thin slab exists at higher frequencies, this dispersion shift was enough to significantly

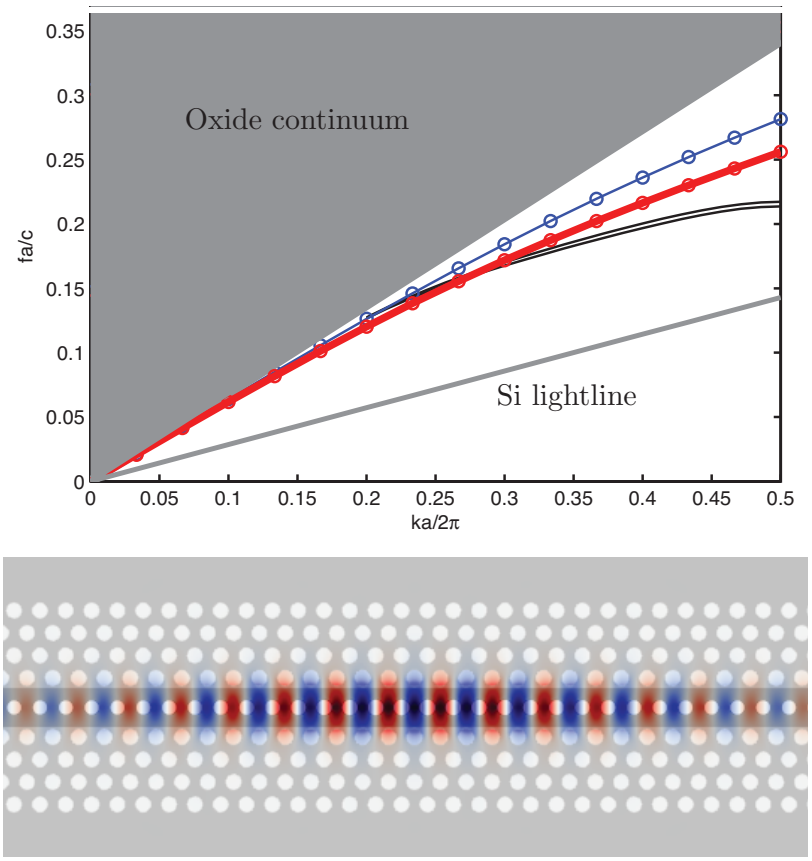

Figure 3-13: The top shows the dispersions of the PCWGs forming the 1D cavity (black lines), with the contact slab modes without holes (lower points, thick line) and patterned with holes (upper points, thin line) of the same wave-vector magnitude.

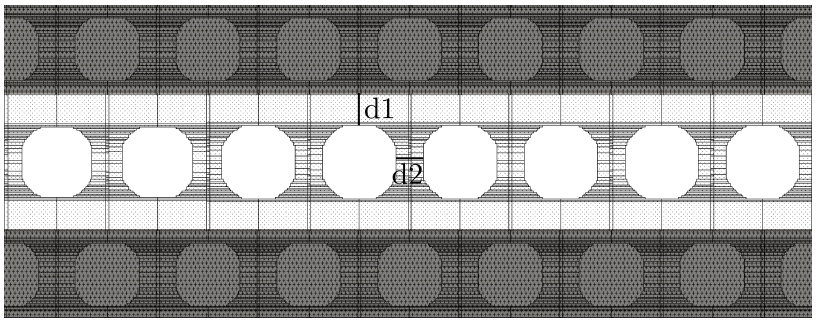

Figure 3-14: Illustration of pSi mask layout near 1D resonator center; the gray shaded regions correspond to the partial-etched contacts.

increase cavity Qs. For the thicker nitride, the effect was drastic, with an order of magnitude or more increase in Q with respect to unpatterned contacts.

The case in the final stackup, with the 30 nm top nitride, is illustrated in Fig. 3-13, the top of which shows the relevant dispersions. The black lines correspond to the dispersions of the big/small 1D PCWGs, and the points with thin and thick lines correspond to the slab modes with the same wavevector magnitudes, without and with patterning in the slabs. Indeed, the unpatterned slab mode is already above the PCWG dispersion, meaning phase-matched coupling should be limited; however, pushing it farther up by patterning the contacts with $r = 0.3a$ holes was observed to increase contacted cavity Qs from roughly 100,000 to 200,000-300,00 (again by the reasoning in Fig. 1-3). Hence, almost all the designs included this patterning. The mode and dielectric profile are represented in the lower part of Fig. 3-13, where the dark gray region is the thick poly core, the light gray the partial-etched contact wing.

The main feature size constraint for the process here, relevant to the optical design, were related to the minimum pSi line width of 100 nm, affecting d1 and d2 in Fig. 3-14. This consideration for D1S meant that the waveguide widths were constrained to be larger than $2r + 200$ nm; increasing waveguide width decreases the resonant frequency (and is actually desirable from the perspective of keeping modes far from the lightline), but meant that the lattice constants to target 1550 were around 320 nm (variants between 300 and 340 were included on the run). Leaving at least this much also was reasonable from the perspective of the ≈ 20 nm misalignment tolerance between the poly patterning and partial etch masks. As a result of this, the as in

these devices were almost all lower than the lattice constants on which the hole size calibration from D0 were based; however, the hole sizes of .3-.35 were also larger, putting the desired radii in the same range. The lattice constant-independence in Fig. 3-7 suggested that the smaller lattice constants would not cause problems with hole formation.

Values for n_{mir} between 8 and 24 were observed to allow variations of loaded Q between about 10^4 and 10^6, symmetrically coupled cavity without contact wings or top SiN; five variants for optical measurements were included between these values for each intrinsic resonator design to allow for a range of couplings around the expected values of up to 100,000, and variants with 6,12, and 18 for the singly coupled detectors variants.

3.3.2 Optical characterization of fabricated cavities

Optical characterization focused on the 1D resonators, which were the main focus of the design in this run. The first section below discusses the Qs observed in different variants, some unexpected but interesting interference expects observed in the 1D resonators. The next discusses the 2D crystals and an analysis of the transmissions through cavities with different coupling strengths.

For these designs as well, both "short-flow" wafers and wafers with contacts formed were tested. In this case the dielectric environment around the poly was the same between the two, and the purely optical testing presented in this chapter used the short-flow samples. The waveguide loss varied significantly across different wafers, and has not been characterized extensively at 1550 nm; the lowest loss observed near 1300 nm, though, was 12 dB/cm, and as in Fig. 2-3, loss around 1550 can be expected to be approximately half this. 6 dB/cm would correspond to a Q of 55,000 for a full confined mode, and serves as a very rough bound on the Qs achievable.

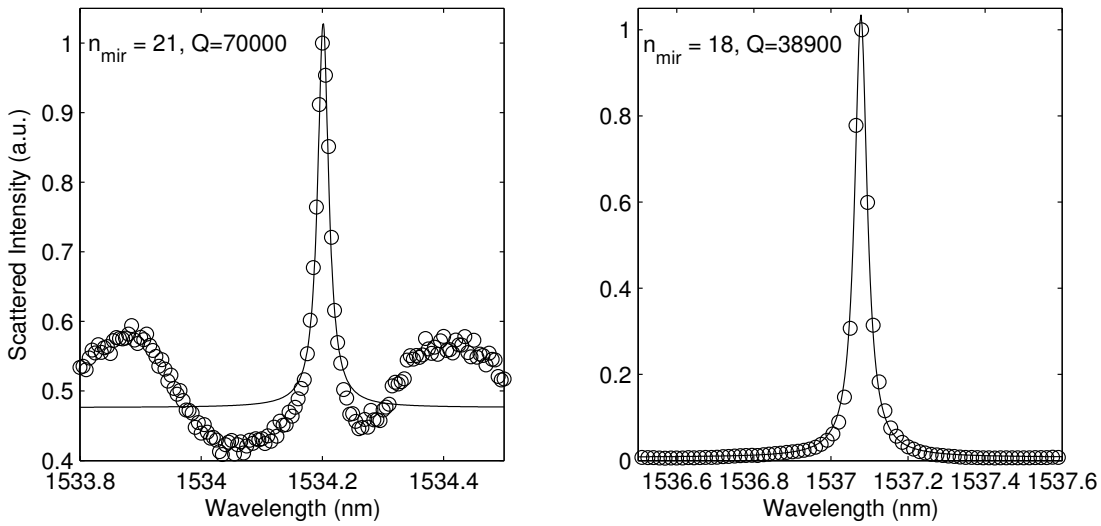

Figure 3-15: Two resonances measured in 1D designs with $a = 330$ nm, $r = 0.33a/0.28a$, wgw= 450 nm, for two of the strongest mirror strengths included. The 70000 resonance (deduced from a Lorentzian fit) is the highest observed.

1D resonators

Fortunately, the graded hole 1D cavities, new to this run, formed well; most of the intrinsic design variants gave Qs of a few tens of thousands (these optical measurements were done on the symmetrically coupled resonators). Some of the measurements on the 1D cavities were done by, instead of measuring transmission at the output grating cavity, placing the output fiber over the resonator itself and measuring the scattered light intensity; this signal strength was often comparable. Fig. 3-15 shows, for example, scattered light traces for two cavities of the same intrinsic design, with two of the highest mirror strengths (18 and 21 mirror periods). A variant with 24 mirror periods was also included, but coupling of light into it was too weak to observe; that the scattered intensity on resonance in the $n_{\text{mir}} = 21$ device is only twice that of background scattering suggests the measured value of 70,000 is close to the intrinsic Q.

These resonators did include partially etched wings patterned with holes; for each intrinsic design, a variant with $n_{\text{mir}} = 12$ was included both with and without the wings, for comparison. In the same intrinsic cavity as in Fig. 3-15, the device without

any contact wings had a $\lambda_0 = 1526.78$ nm and $Q = 38,000$, whereas with contact wings $\lambda_0 = 1535.90$ nm and $Q = 33,000$; the 9 nm redshift indicates a somewhat larger modal overlap with silicon.

The effect of patterning the contact wings was also measured by comparing two cavities, with the same hole design ($a = 320$ nm, $r = 0.33/.33a$, $wgw = 450$ nm), one of which had the contact wings patterned with a triangular lattice of $r = .3a$ holes (and which had a resonant wavelength λ_0 of around 1505 nm), and one with continuous contact wings ($\lambda_0 \approx 1551$ nm). The measured Qs as a function of n_{mir} are shown in Fig. 3-16. The higher Qs in the patterned devices are due partly to decreased leakage into slab modes of the contact wings; but, interpretation of this result is complicated by the fact that the mode in the unpatterned contact device may see a lesser effect mirror strength, since more of the mode overlaps with the silicon outside the region with the graded hole sizes. Nevertheless, the Q's rate of increase for the unpatterened device is levelling off at $n_{\text{mir}} = 24$ at around 30,000, whereas the patterned device has already exceeded this at $n_{\text{mir}} = 18$, suggesting that the intrinsic Q of the patterned device is higher to some extent, though not substantially for this wing thickness.

The overall transmission through these devices was as expected, and was close to unity for strongly coupled cavities. Fig. 3-17 shows the transmission measured from a straight waveguide (serving as a measurement of the input/output grating coupler loss), along with that through a strongly coupled 1D PC cavity, whose peak transmission is only 2 dB below that of the grating couplers.

Observation of Fano resonances

In the course of the measurements on the 1D cavities, it was found that, depending on the position of the input and output fibers, the lineshapes of the resonances would not be Lorentzians, but would be somewhat asymmetric or even exhibit dips, rather than peaks, at the resonance frequency. An example is shown in Fig. 3-18.

This kind of lineshape, which could be fit by a Fano profile, arises from the interference of waves whose transmission is governed by a state at a single frequency

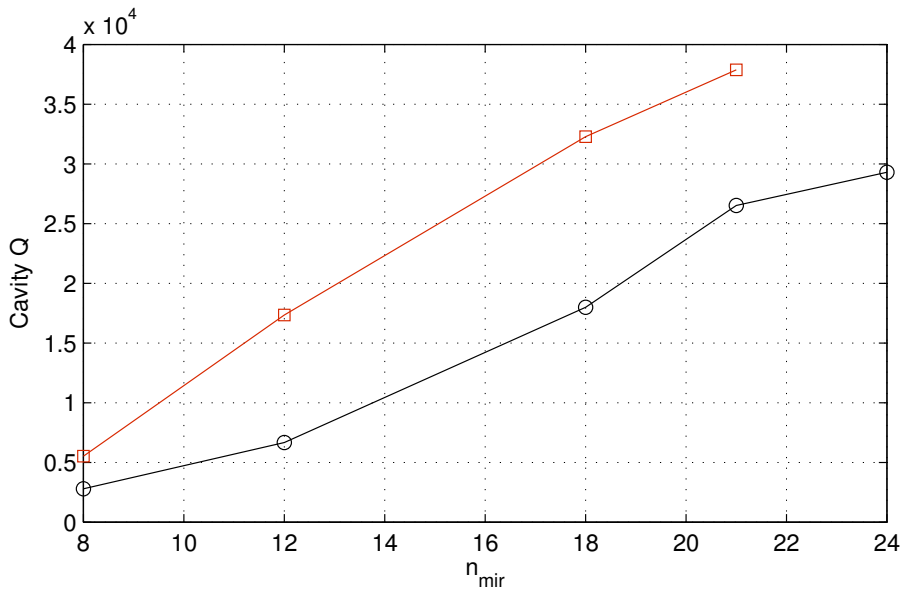

Figure 3-16: Measured Qs for 1D resonators with (squares) and without (circles) holes patterned in the contact wings, as a function of the number of mirror holes on either side of the cavity. The devices were on different chips, however, and the waveguide loss may have been different.

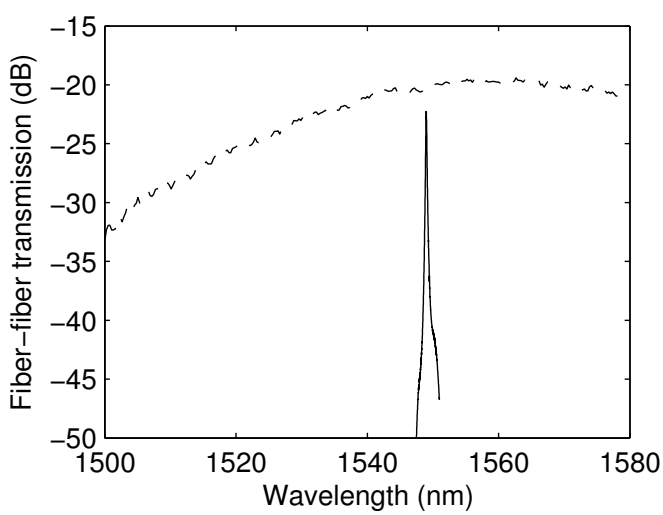

Figure 3-17: The dotted line shows the transmission through a short straight waveguide, which serves as a measurement of the loss due to input and output through the grating couplers. The solid shows transmission through a strongly coupled 1D cavity, which is only 2 dB below the coupling loss on resonance.

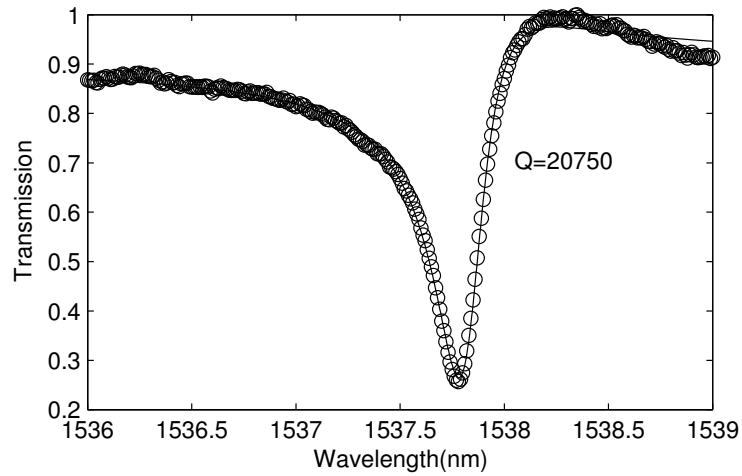

Figure 3-18: Transmission as measured through a 1D cavity with $a = 330$ nm, wgw=450 nm, $r = 0.33/0.28a$, $n_{\text{mir}} = 12$, along with a line corresponding to a theoretical Fano lineshape.

(the resonant mode in this case, which couples to the fundamental TE mode of the bus waveguide), and waves with a relatively continuous transmission spectrum [MFK10]. In these devices, some higher order mode of the bus waveguides could be expected to form the continuum states. The 450×220 nm^2 bus waveguides, as well as the photonic crystal region, supports a TM mode; some mixing of TM and TE modes at the grating coupler may then have been expected to explain the Fano lineshape, but the effect was observed even when polarizations were carefully optimized to be TE.

The bus waveguides also support a second order guided mode, antisymmetric about the waveguide center. It is not guided in the photonic crystal region, but proved to be only weakly leaky. That this mode was responsible for the interference was verified by scanning the input single mode optical fiber down along the input grating coupler, and measuring the transmission at different points. If the fiber is exactly at center, only the fundamental mode of the waveguide is excited; above center, some mixture of the fundamental mode and second order mode propagate; and below center, the same mixture, except with the opposite relative phase of the first and second order modes (due to the second mode's antisymmetry), is excited. The asymmetry in the Fano lineshape arises from the fact that the resonant mode has opposite phase on either side of the resonance, whereas the continuum modes' phase

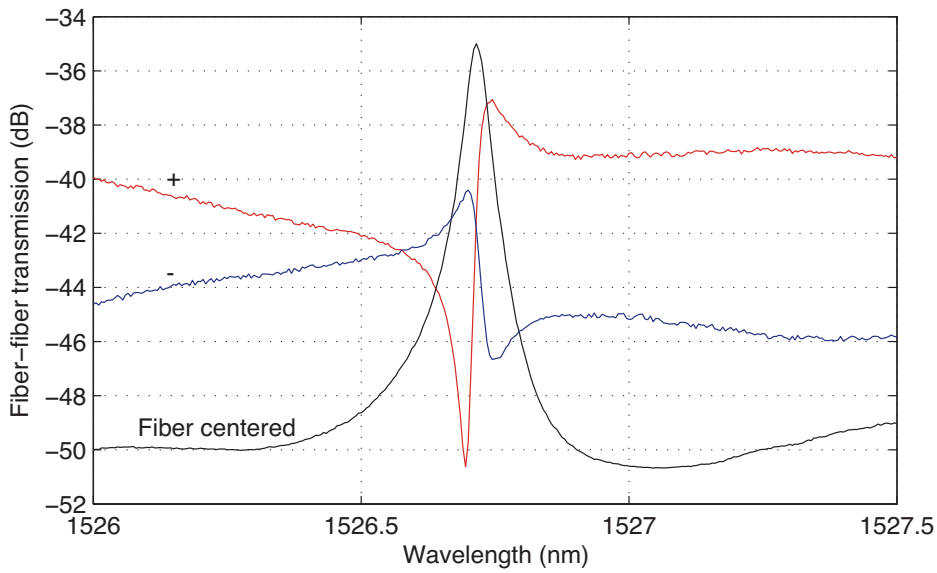

Figure 3-19: Transmissions through a 1D cavity (a = 330 nm, wgw=450 nm, $r = 0.33/0.28a$, $n_{\text{mir}} = 12$, no contact wings), with the output fiber position fixed off-center and the input fiber on-center and to either side of center (labeled + and -). The different strengths of the features in the + and - curves are likely due to unintentional drift of the fiber along the perpendicular axis

is relatively constant. Thus, we expected that the profile should "flip" as the fiber is brought down along the input coupler. Fig. 3-19 shows this behavior, indicating the role of the second order mode. It was important that the output fiber be fixed and off-center for this measurement – if on-center, the overlap of the second order guided mode with the single fundamental fiber mode would be 0 and no such interference would be seen, and when both fibers move together, by symmetry the sign of the effect is identical on either side of the couplers.

The strength of the asymmetry was also tunable by power, as shown in Fig. 3-20; simply raising the power input results in a larger stored energy on resonance, reducing the cavity Q and hence reducing the ratio u/P_{in}. Thus the ratio of light collected (scattering in this case) from the cavity mode and from the leaky second order mode changes as a function of power.

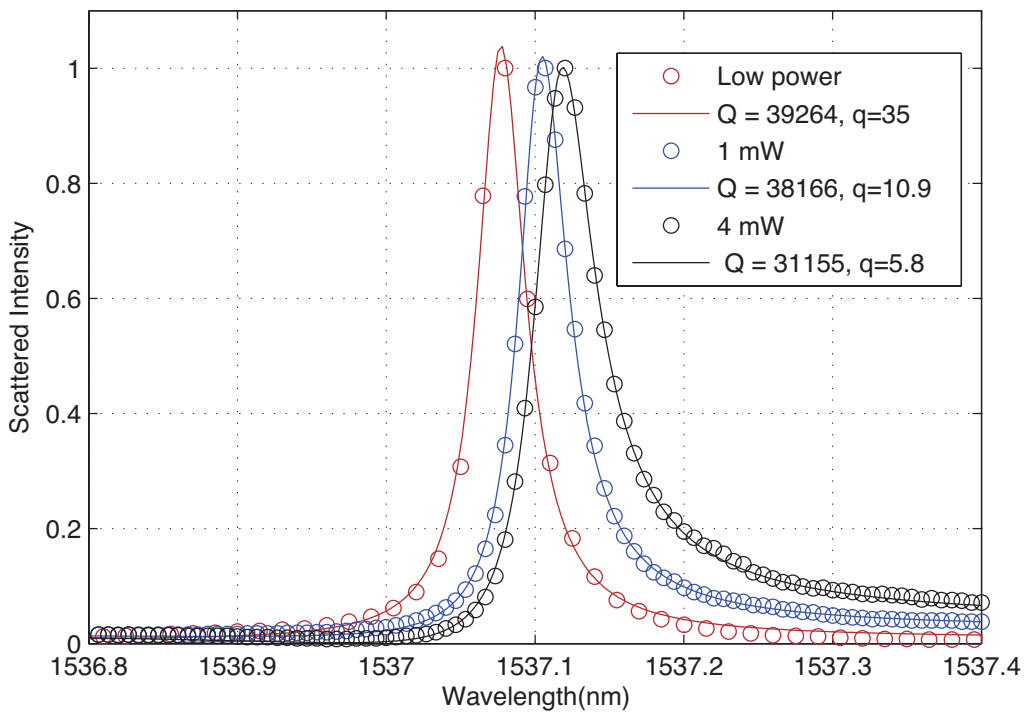

Figure 3-20: Scattered intensity from a 1D crystal for various input powers, and Fano fits. The lower case q-parameter reflects the degree of asymmetry.

2D cavities, and coupling analysis

The results from the three and five hole cavities had less new in them as compared to D0, and so I discuss them in less detail here. Three hole cavities with loaded Qs of about 8000, and 5-hole cavities with Qs of 23000 were measured; an important observation was made regarding the peak transmission through these cavities, though. On resonance, the transmission through a symmetrically loaded, lossy cavity is $Q_{\mathrm{tot}}^2/Q_{\mathrm{e}}^2$, where Q_{tot} is the measured loaded Q and Q_{e} characterizes the coupling into the bus waveguides. When the cavity Q is dominated by loading, transmission should be nearly unity (Fig. 3-17), but in the 3 and 5 hole cavities this was not the case.

Fig. 3-21 shows the transmissions through 4 different intrinsic cavities (a-d), each with three different coupling strengths. (e) plots the measured Q_{tot} against the peak transmission (with coupler loss, determined from a measurement on a straight waveguide, normalized out); the bold lines show the theoretical values for a particular Q_0, labeled in the legend. The 1D cavity transmissions match this trend well, but the 3- and 5-hole cavities each require some additional, uniform loss, around 8-13 dB, to fit the trend.

The couplers between the strip bus waveguides and the PCWGs are known to have low losses, only approximately 1 dB each, and thus this additional loss is most likely due to loss in the PCWG itself. The feeding length is only 10μm, so for even 3 dB, a propagation loss of 3000 dB/cm would be required to account for the observed loss, much higher than the measured loss around 10 dB/cm; however, the PCWGs can have group indices of many hundreds [VOHM05], making this plausible. The different excess losses for the 3 and 5 hole cavities may be explained by the fact that they sit at different frequencies, at different points on the PCWG dispersion; the lower frequency of the 5 hole resonance puts it closer to the guided mode's cutoff, where the group index is higher.

Finally, a number of width-modulated line defect cavities were included on the mask as well, but are less completely characterized at the time of writing. A measurement of one is shown in Fig. 3-22. This cavity had a lattice constant of 380 nm,

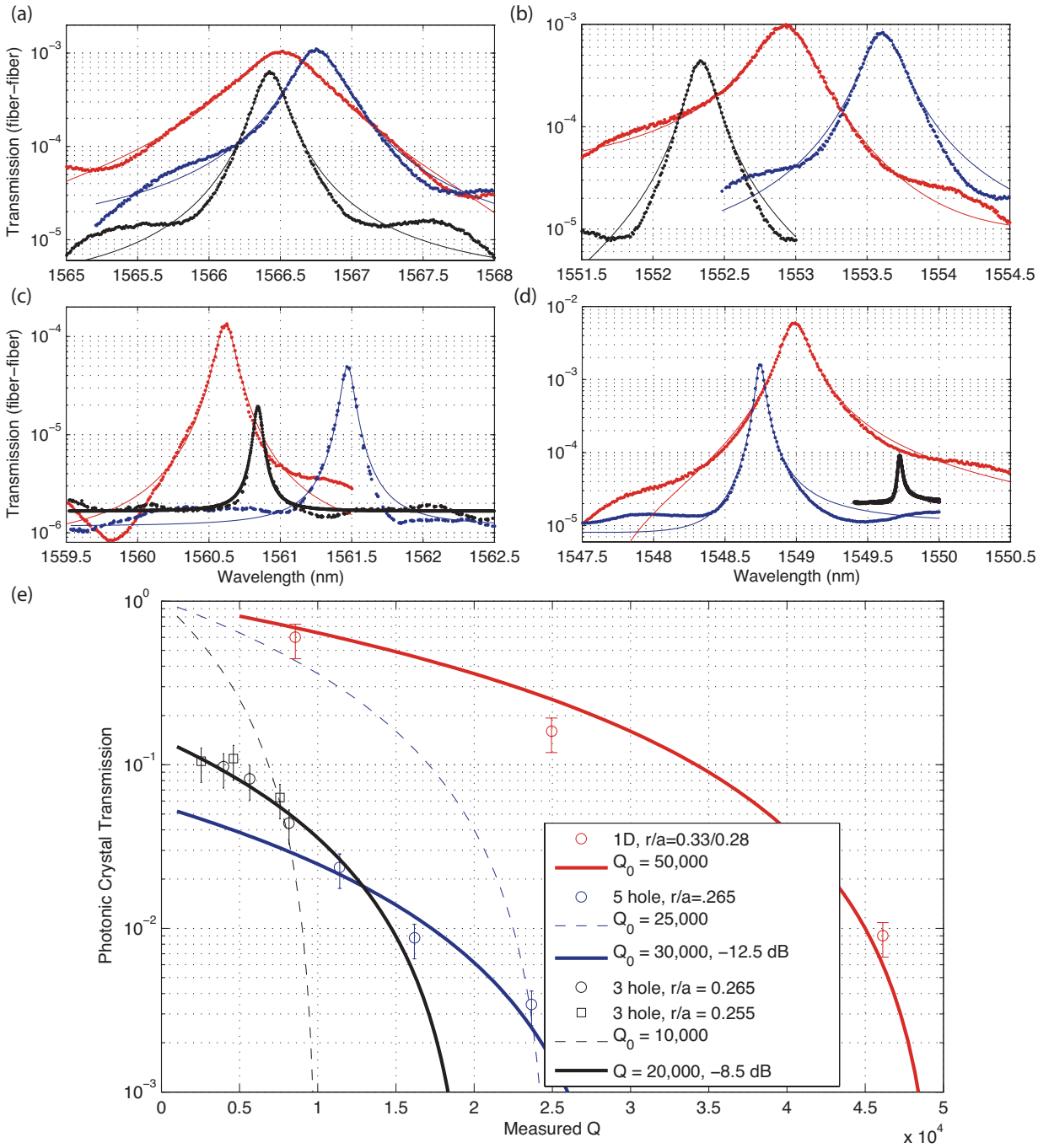

Figure 3-21: Each plot in (a)-(d) shows the transmission through a cavity of a one intrinsic design with three different couplings. (a) and (b) show transmissions through 3-hole cavities with $r = 0.255a$ (a) and $0.265a$ (b); the couplings are $n_{\text{coupl}} = 2$ (red), $n_{\text{coupl}} = 2/d_{\text{coupl}} = 76$ nm (red), and $n_{\text{coupl}} = 3$ (black). (c) shows traces for a 5-hole cavity with $r = 0.265a$, with $n_{\text{coupl}} = 2$ (red), $n_{\text{coupl}} = 2/d_{\text{coupl}} = 76$ nm (red), and $n_{\text{coupl}} = 3$ (black); and (d) shows the same for a 1D cavity with $n_{\text{mir}} = 8$ (red), 12 (blue), and 18 (black). (e) shows the peak transmission (with coupler loss removed) plotted against the fitted Q for each cavity in (a)-(d), and solid lines showing theory. The 3 and 5 hole cavities show excess loss corresponding to PCWG loss, as discussed in the text.

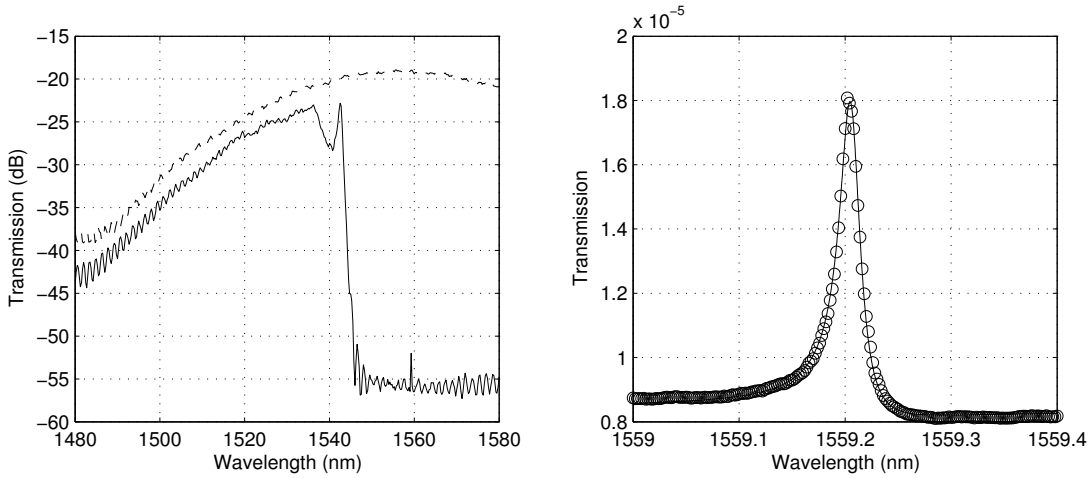

Figure 3-22: Left: fiber-fiber transmission over a broad range through a line defect cavity structure, with straight waveguide transmission shown in the dotted line. Right: fine scan over the resonance at 1560 nm, with a Fano fit (line) showing a Q of 65000.

hole radii $0.255a$, $\text{bar}_\text{l} = 8$, and hsh=30 nm. The 2D line defects are thus also able to approach the material loss limit on this chip.

To summarize the Qs achieved in the different designs included on this chip, Qs of about 70,000, near the material loss limit, were observed for both of the gradually confining designs (1D and width-modulated line defect cavities); the 3 and 5 hole cavities had, in the most weakly coupled variants included, measured Qs of 7,000 and 23,000, respectively, corresponding to estimated intrinsic quality factors of about 20,000 and 30,000.

Since all the 2D cavities suffered from the excess loss due to transmission through the PCWG, the subsequent electrical testing, to be discussed in the next chapter, focused on the 1D resonators on this chip.

3.4 First attempt: IBM EOS 8

The first attempt at photonic crystal fabrication was made in the IBM process, in which the silicon layer is only 80 nm thick. Attempts were made to design 3 and 5-hole defect cavities within this process, despite the knowledge that with such thin slabs, cavity Qs with these designs would be seriously limited, since the modes are not

well confined and thus lie near the cladding light-line, and hence very susceptible to radiative loss. Nevertheless, simulations indicated cavity Qs of a few thousands, and some basic devices were specified on the mask. Though I didn't realize it during the design, this can happen even when the PCWG does not support a guided mode – the slab was thin enough that the guided mode was actually cut-off, and so experimentally too little light reached the low-Q cavity to be measured. These measurements thus indicated little. Simulations have shown that 1D resonators are viable approaches to high-Q cavities in this platform, but a contact method without the partial etch has not been developed.

3.5 Conclusion and summary

Photonic crystal designs of various kinds proved versatile enough to implement within Micron's DRAM process, with no special accommodations made in the fabrication process. Though the 3- and 5-hole defect cavities were limited by radiative lifetime in the low index-contrast dielectric environment, the gradually confining approaches both achieved Qs limited by the material loss rate; these small mode-volume cavities are thus capable of the same Qs as microrings in this platform. The geometries for graded 1D cavities in this platform, due to the availability of a partial etch and doping implants, allowed demonstration of contactable cavities of this kind. Table 3.1 summarizes the various cavities measured optically, and their experimental resonant wavelengths and Qs. Having established generally the optical properties of the fabricated resonators, the next chapter proceeds to discuss electro-optic measurements made on these cavities.

Design Parameters (all lengths in nm)	$\lambda_0(nm)$	Q
(1D) a=330, r=0.33/0.28a, wgw=450, $n_{\text{mir}} = 12$, no wings	1526.8	37000
(1D) a=330, r=0.33/0.28a, wgw=450, $n_{\text{mir}} = 8$, $r_c = 0.3a$	1536.5	8700
(1D) a=330, r=0.33/0.28a, wgw=450, $n_{\text{mir}} = 12$, $r_c = 0.3a$	1535.9	33000
(1D) a=330, r=0.33/0.28a, wgw=450, $n_{\text{mir}} = 18$, $r_c = 0.3a$	1537.1	38900
(1D) a=330, r=0.33/0.28a, wgw=450, $n_{\text{mir}} = 21$, $r_c = 0.3a$	1534.2	70000
(1D) a=330, r=0.33/0.28a, wgw=470, $n_{\text{mir}} = 8$, $r_c = 0.3a$	1549.0	8600
(1D) a=330, r=0.33/0.28a, wgw=470, $n_{\text{mir}} = 12$, $r_c = 0.3a$	1548.8	24940
(1D) a=330, r=0.33/0.28a, wgw=470, $n_{\text{mir}} = 18$, $r_c = 0.3a$	1549.7	46130
(1D) a=320, r=0.33/0.3a, wgw=450, $n_{\text{mir}} = 8$, $r_c = 0.3a$	1505.3	5525
(1D) a=320, r=0.33/0.3a, wgw=450, $n_{\text{mir}} = 12$, $r_c = 0.3a$	1504.1	17350
(1D) a=320, r=0.33/0.3a, wgw=450, $n_{\text{mir}} = 18$, $r_c = 0.3a$	1504.8	33000
(1D) a=320, r=0.33/0.3a, wgw=450, $n_{\text{mir}} = 21$, $r_c = 0.3a$	1504.2	38000
(1D) a=320, r=0.33/0.3a, wgw=450, $n_{\text{mir}} = 12$, no wings	1510.6	14100
(1D) a=320, r=0.33/0.3a, wgw=450, $n_{\text{mir}} = 8$, $r_c = 0$	1552.1	2793
(1D) a=320, r=0.33/0.3a, wgw=450, $n_{\text{mir}} = 12$, $r_c = 0$	1551.3	6660
(1D) a=320, r=0.33/0.3a, wgw=450, $n_{\text{mir}} = 18$, $r_c = 0$	1551.3	18000
(1D) a=320, r=0.33/0.3a, wgw=450, $n_{\text{mir}} = 21$, $r_c = 0$	1552.9	26509
(1D) a=320, r=0.33/0.3a, wgw=450, $n_{\text{mir}} = 24$, $r_c = 0$	1551.7	29300
(3h) a=380, $r = 0.255a$, $d_Q = 91$, $d_{\text{coupl}} = 0$, n_c=2	1566.5	2550
(3h) a=380, $r = 0.255a$, $d_Q = 91$, $d_{\text{coupl}} = 76$, n_c=3	1566.7	4600
(3h) a=380, $r = 0.255a$, $d_Q = 91$, $d_{\text{coupl}} = 0$, n_c=3	1566.4	7455
(3h) a=380, $r = 0.265a$, $d_Q = 91$, $d_{\text{coupl}} = 0$, n_c=2	1552.8	3974
(3h) a=380, $r = 0.265a$, $d_Q = 91$, $d_{\text{coupl}} = 76$, n_c=3	1553.6	5650
(3h) a=380, $r = 0.265a$, $d_Q = 91$, $d_{\text{coupl}} = 0$, n_c=3	1552.3	8160
(5h) a=380, $r = 0.265a$, $d_Q = 91$, $d_{\text{coupl}} = 0$, n_c=2	1560.6	11400
(5h) a=380, $r = 0.265a$, $d_Q = 91$, $d_{\text{coupl}} = 76$, n_c=3	1561.5	16175
(5h) a=380, $r = 0.265a$, $d_Q = 91$, $d_{\text{coupl}} = 0$, n_c=3	1560.8	23550
(LD) a=380, $r = 0.255a$, hsh= 30, bar$_l$=8a	1559.2	55000
(D0, 3h) a=375, $r_{\text{spec}} = 107$, $d_Q = 91$, $d_{\text{coupl}} = 0$, n_c=3	1526	6240
(D0, 3h) a=375, $r_{\text{spec}} = 103$, $d_Q = 91$, $d_{\text{coupl}} = 0$, n_c=3	1543	3630
(D0, 3h) a=375, $r_{\text{spec}} = 99$, $d_Q = 91$, $d_{\text{coupl}} = 0$, n_c=3	1563	1860

Table 3.1: Resonator parameters, and optically measured resonant wavelengths λ_0 and Qs on short flow devices; devices are from D1S unless labeled D0, with 1D, 3h, 5h, and LD indicating 1-D graded hole, 3-hole, 5-hole, and line-defect designs.

Chapter 4

Optoelectronic measurements on contacted devices

Optoelectronic measurements on contacted resonators functioning as detectors are discussed in this chapter. Though the devices were designed with the intent of maximizing two-photon absorption, it happened that in the cases achieved so far, linear absorption has been strong enough that it is the dominant effect.

4.1 1D resonator measurements

Electronic testing of the D1S resonators focused on the 1D devices, which did not suffer from any excess PCWG loss into the resonators. Unfortunately, it seems no contacts were made successfully to the devices with holes in the contact wings; however, contacts were successfully made in devices with continuous wings. The reason for this is unclear, and may have to do with the formation of the holes in the partial-etched wings. Unfortunately, variants of only two cavity designs ($a = 320$ and $a = 300$, both with $r = 0.33/.3a$, wgw=450 nm) were included with continuous wings, limiting the options for electrical measurements.

Optical measurements on the $a = 320$ nm devices where shown in Ch. 3; electrical measurements were conducted on a different sample, which went through the full contact deposition process at Micron. Waveguide loss in this poly was measured

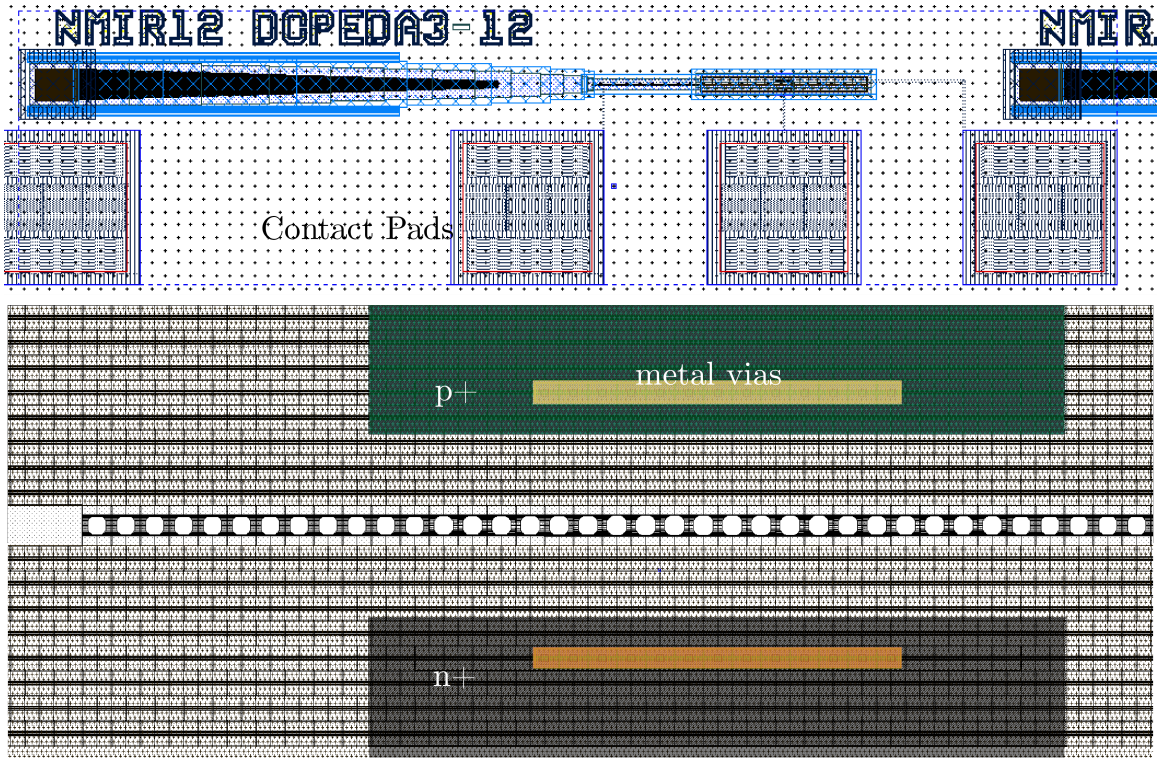

Figure 4-1: The upper image shows the mask layout of the 1D cavity studied here, in a detector configuration with only one input waveguide, including three contact pads, spaced to fit a 100 m GSG probe. The lower image shows a close-up of the cavity region. The region shaded with white crosses (immediately above and below the middle row of holes) is the partially etched contact wing region; the red area corresponds to the p+ source implant region, and the bottom white to the n+ (each of these are 960 nm from the thick poly cavity core). The blue area shows the first metal layer, which connects to the doped regions with 80×80 nm^2 vias.

to be approximately double that of the "short-flow" wafers, which didn't include the contacts, resulting from some of the additional processing steps and/or anneals (though the mechanism of this is unclear); however, Qs measured in these 1D variants with contacts were not observed to be significantly different from those shown in Fig. 3-16, for the $n_{\text{mir}} = 8$, 18, and 21 devices.

Almost all of the measurements were done on a 1D cavity in a detector configuration ($n_{\text{mir}} = 12$, no output waveguide), in which the dopant implant regions were separated from the waveguide edge by 960 nm, resulting in an intrinsic region length of $2 \times 960 + 450 = 2370$ nm; due to dopant diffusion, this is likely to be reduced by approximately 200 nm in reality. The width of the implant regions extended over

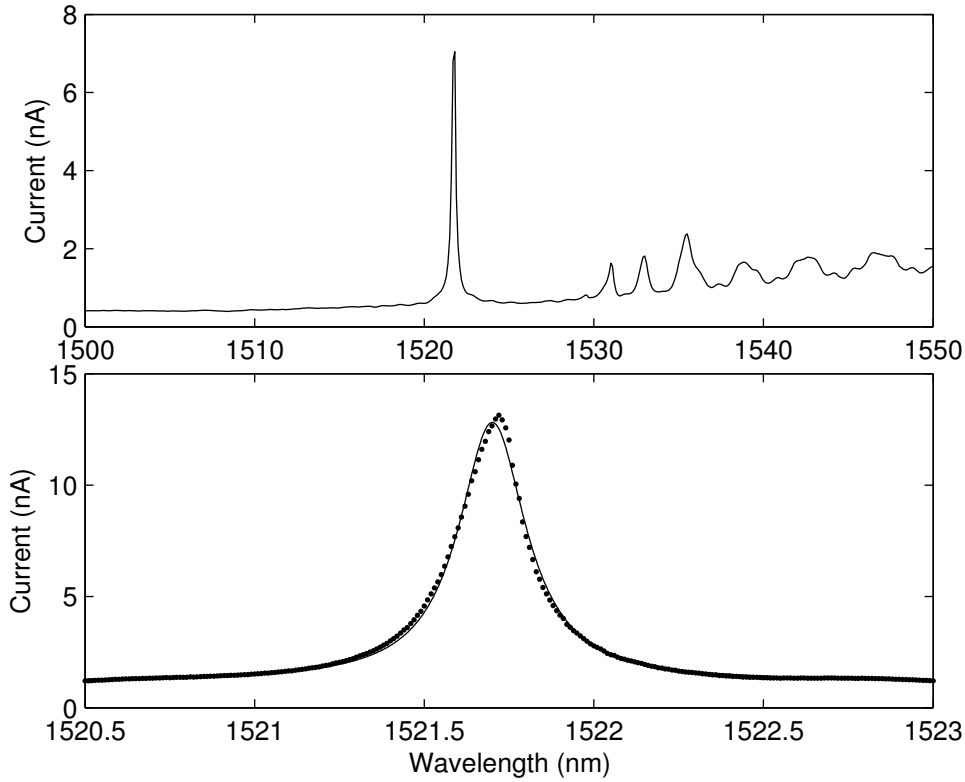

Figure 4-2: Photocurrent vs. illuminating wavelength over a broad wavelength range for the 1D cavity detector, biased at -1 V and with an input in-waveguide power of between 10 and 20 μW, showing a resonance at $\lambda = 1522$ nm; the finer plot shows a lorentzian fit with a Q of 6300.

24 lattice periods, corresponding to 7.68 μm in this device. Fig. 4-1 shows the mask layout of the device, including contact pads, as well as a close up view around the cavity, showing the doping implant regions. The implants used in these devices were the p+/n+ source/drain implants, which were targeted to 1×10^{20} cm^{-3} in this process.

The first part of this section discusses DC measurements on the diode, with and without illumination, to characterize its peak quantum efficiency (QE). The second addresses its operation speed via preliminary measurements of its frequency response.

4.1.1 DC Measurements

Fig. 4-2 shows the current through the diode at -1V applied, with 23 W entering the waveguide (after the grating coupler). The resonance at 1522 nm manifests itself

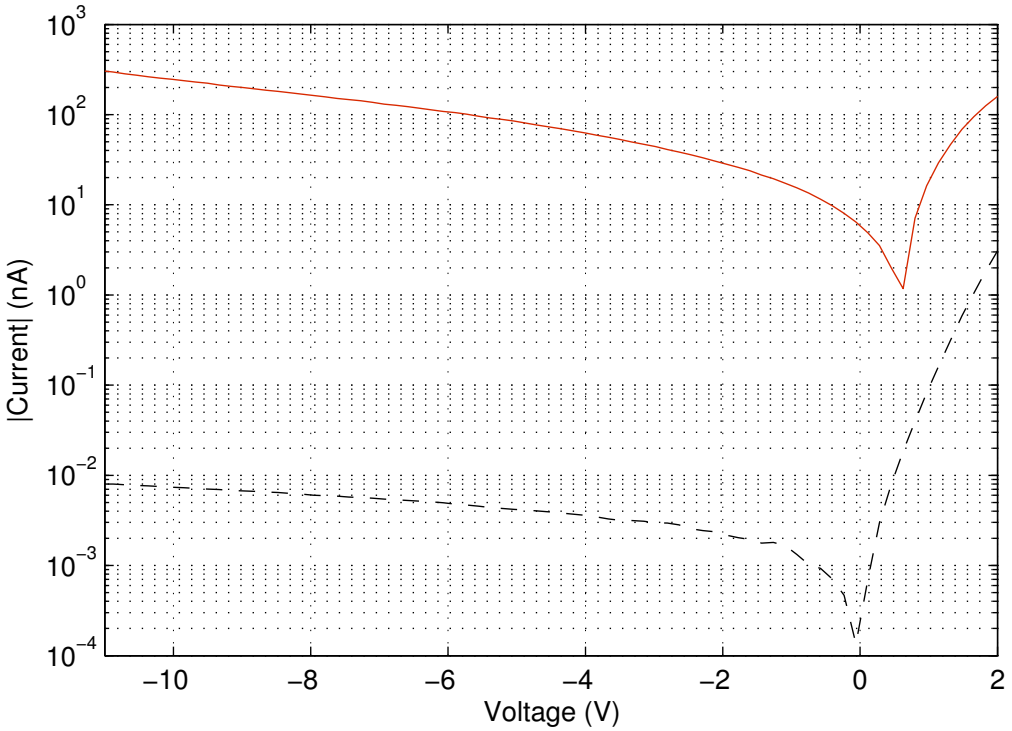

Figure 4-3: Current-voltage relations for the 1D resonator diode without any illumination (dotted black line), and with 92 μW on-resonance light input (red line).

as a clear and narrow peak in the current, when the intensity between the doped regions (and hence the linear absorption-generated photocarrier concentration) is maximum. From the fit to the fine wavelength sweep, the loaded Q is estimated to be 6300. This measurement, along with an estimate of the intrinsic $Q_0 \approx 30000$ from optical measurements on the symmetric resonators, puts the waveguide coupling $Q_\mathrm{e} = \left(\frac{1}{Q_l} - \frac{1}{Q_0}\right)^{-1} = 8000$. From the relations in Ch. 1, this implies a cavity reflectivity on resonance of $R = \left(\frac{Q_\mathrm{e}-Q_0}{Q_\mathrm{e}+Q_0}\right)^2 = 33\%$; this rough estimate indicates that approximately 66% of the input light power should be dropped into the cavity. This result does not account for the effect of doping on the intrinsic Q, and is not used in the estimates of QE below.

Fig. 4-3 shows a comparison of the dark current-voltage (I-V) relation, with no illumination, with that under illumination. That only a few nanoamperes flow under application of 2 V forward bias indicates a very large series resistance.

The subsequent measurements focused on characterizing the DC efficiency of detection as a function of voltage applied and optical power. The top plot in Fig. 4-4 shows the photocurrent measured as a function of wavelength, for various input powers between 1.1 μW and 82 μW, with the diode voltage held constant at -22 V. The curves show a clear resonance-pulling effect, due to heating of the device at large optical powers, which redshifts the resonance; for a given optical power, this effect became more pronounced as the voltage was increased, since the current (and hence the resistive heating resulting from sweepout of photocarriers) increased with voltage.

The peak responsitivity R_pk (A/W) is calculated as the maximum photocurrent i_pk divided by the input power P_in, and the QE is given by

$$\mathrm{QE}_\mathrm{pk} = R_\mathrm{pk} \times \frac{h\nu}{1.6 \times 10^{-19}\mathrm{C}} \approx R_\mathrm{pk} \times 0.82\mathrm{W/A}, \tag{4.1}$$

the latter approximation being for 1522 nm light. The fact that some of the power in the waveguide does not enter the cavity (is reflected) is not considered; this loss is included in the QE numbers presented here. The results are shown in the lower plot of Fig. 4-4, for reverse bias voltages increasing from 2 to 34 V in increments of 4V.

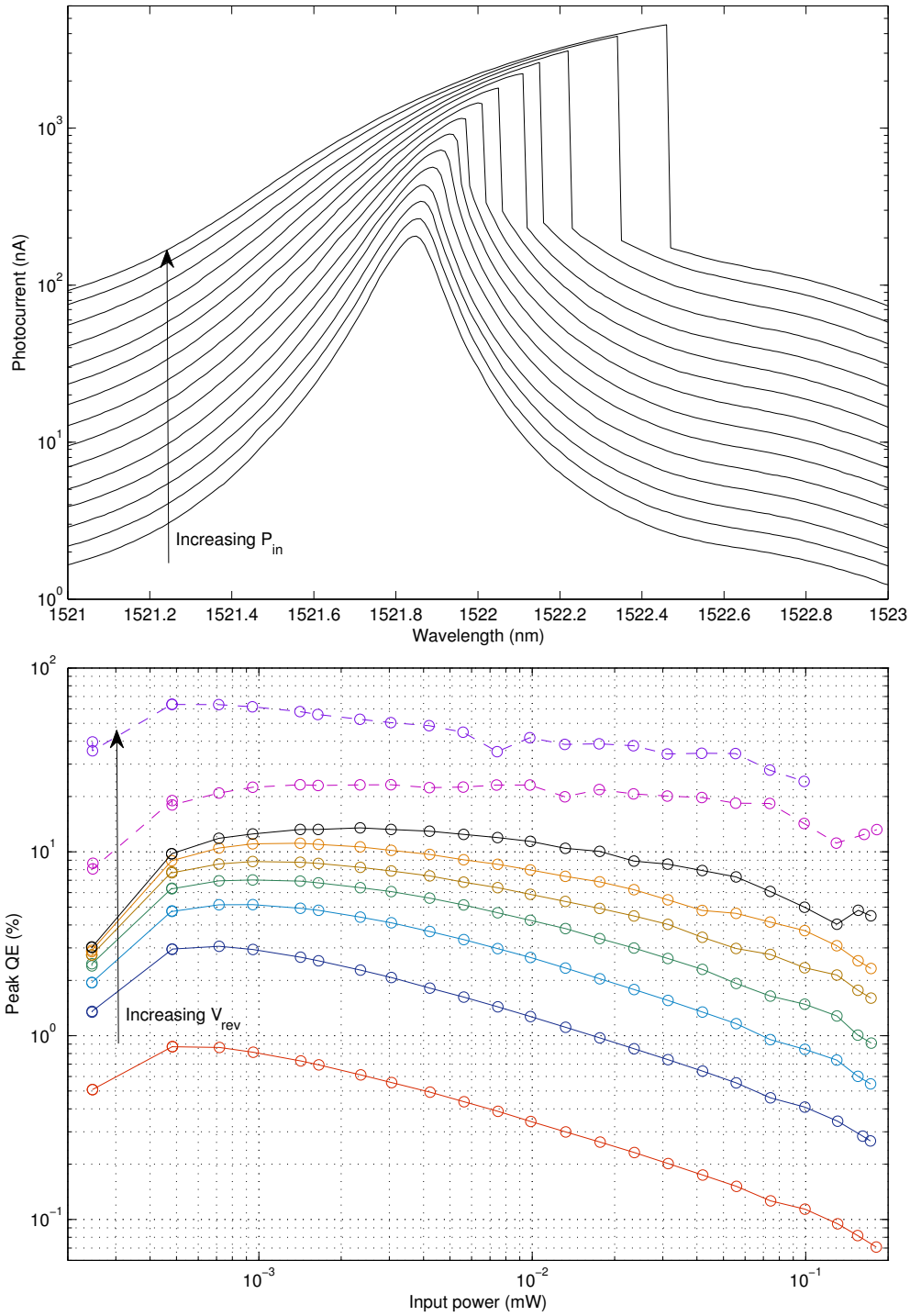

Figure 4-4: Detected photocurrents vs. wavelength for increasing input powers between 1 and 100 μW, with -22 V applied (top), and power-dependent measured peak QEs for voltages between -2 and -34 V (bottom).

The fact that, at a given input power, current increases steadily with voltage (without obvious avalanching), suggests that recombination in the intrinsic region limits the fraction of excited carriers extracted; at higher voltages, more rapid sweep-out lessens this loss of excited holes and electrons. The decrease in quantum efficiency with increasing power between 1 and 100 μW is a striking feature of this plot, and could result from a few contributions. One might expect free carrier absorption from the linearly generated carriers to reduce the overall Q of the cavity and hence limit the fraction of optical power absorbed at high powers; however, a rough calculation shows the loss rate from FCA should be much lower than the resonator's low-power Q of around 7500. Additionally, a similar decrease in pSi detector efficiency has been observed in a 50μm radius ring resonator [PLZL11], suggesting that at least some of this behavior is an intrinsic material response of polysilicon. For example, a density-dependent recombination rates, which have been indirectly observed in crystalline silicon optical devices [BSP05, LT04] could serve to decrease extraction efficiency with increasing optical power. This would also be consistent with the tendency of the curves to level off at higher voltages; as the extraction becomes more rapid, the differential increase in recombination rate due to carrier density-dependence has less of an effect on overall extraction.

Further measurements will be required to understand the dynamics that explain this behavior. The quantum efficiencies achievable here are promising; at -22 V, over 10% QE is observed; and, the highest QE measured is around 63%, with a bias of -34V. However, interpretation of this is somewhat complicated, as the electrical structure of the device changed after undergoing tests at -34V; as shown in Fig. 4-5, after the DC testing at -34 V, a drastic increase in dark current was observed. This effect was not irreversible, though, and the same current was somewhat reduced after a few days sitting at room temperature. That time at room-temperature would result in a reversal of the increase would suggest that dopant diffusion is not the contributor here; perhaps some long-lived or metastable defect-state, somehow "activated" by the large voltage, contributes to the dark current. Related, long-term alterations in the electrical characteristics of similar devices have been observed, but not explained, in

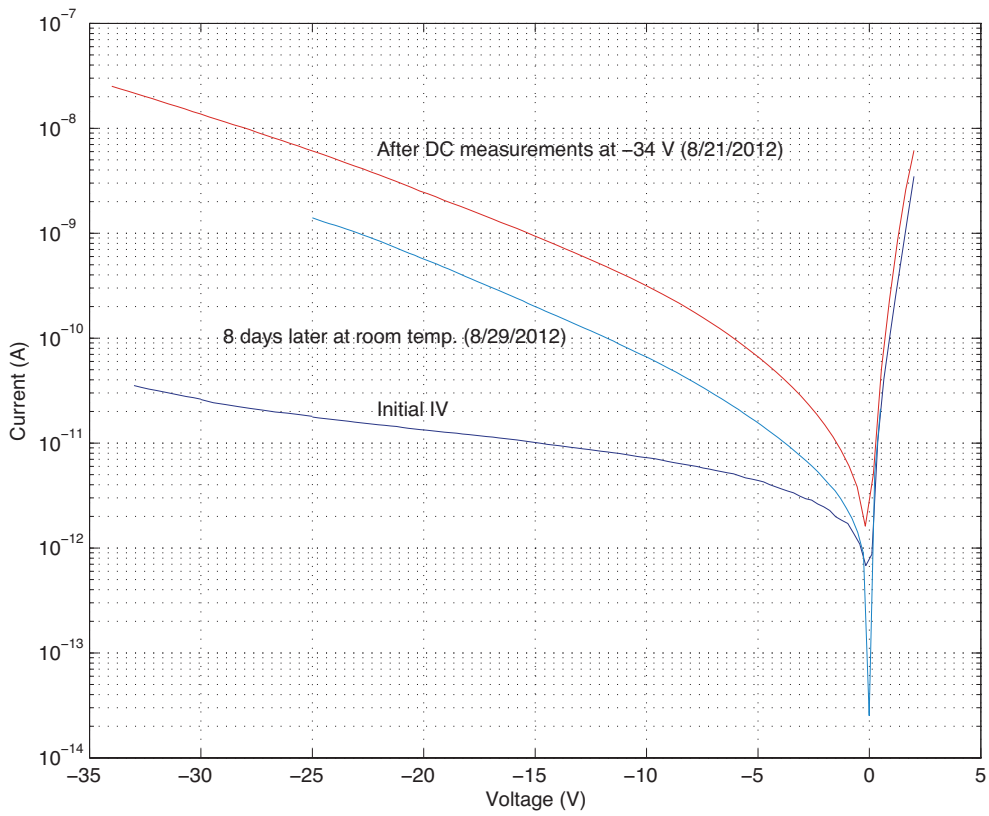

Figure 4-5: Changes in dark IV relations for the 1D cavity studied; a substantial increase in dark current was seen after DC testing at -34V, which lessened after a few days at room temperature during which no tests were done.

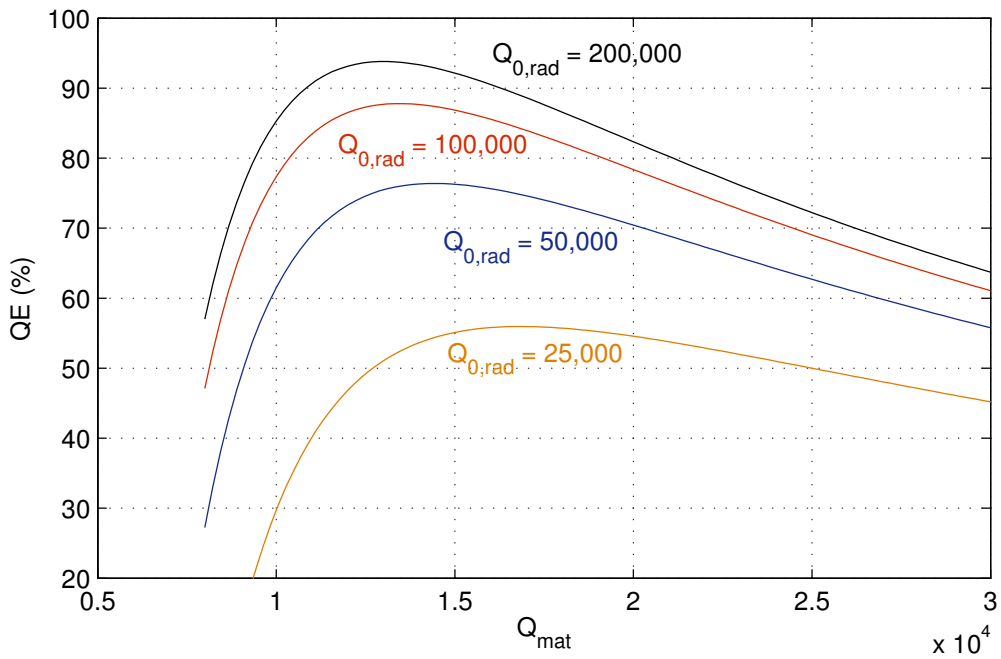

Figure 4-6: Theoretical maximum possible linear absorption QEs for a resonator for a total loaded $Q_l = 6300$ (as measured) with various radiative Qs (accounting for all loss rates other than linear absorption), as a function of the uncertain Q_{mat}.

other work, e.g. in ion-implanted crystalline silicon [GSG+07a].

A quick calculation based on the standard coupled mode analysis reviewed in Ch. 1 serves as a check for whether linear absorption could account for these QEs. For a resonator coupled to a feeding waveguide on one side, we had $U = \frac{\frac{2}{\tau_{\mathrm{e}}} P_{in}}{(1/\tau_0 + 1/\tau_{\mathrm{e}})^2}$, where to allow comparison with experiment we split the intrinsic loss rate, τ_0, into parts corresponding to material absorption and radiative loss (or any other loss not producing a free carrier): $\tau_0^{-1} = \tau_{\mathrm{rad},0}^{-1} + \tau_{\mathrm{mat}}^{-1}$. The linearly absorbed power is $P_{abs} = U \frac{2}{\tau_{\mathrm{mat}}}$, which gives for the efficiency,

$$\frac{P_{abs}}{P_{in}} = 4\left(Q_{\mathrm{e}} Q_{\mathrm{mat}}\right)^{-1} \left(\frac{1}{Q_{\mathrm{rad},0}} + \frac{1}{Q_{\mathrm{mat}}} + \frac{1}{Q_{\mathrm{e}}}\right)^{-2}. \tag{4.2}$$

This analysis naturally includes the incomplete coupling into the cavity when critical coupling is not satisfied. The loaded quality factor, including all loss rates, was measured to be 6300. Q_{mat} and Q_{rad} are the two unknown parameters (from which Q_{e} follows for the known Q_l) which determine the fraction of input power lost

to linear absorption in the detector. If each absorption event produces a free carrier that is swept out, this fraction equals the quantum efficiency. This maximum QE is plotted in Fig. 4-6, for a wide range of radiative Qs, as a function of the Q_{mat}, for the measured Q_l. The expected loss coefficient of 20 dB/cm in these samples would correspond to $Q_{\mathrm{mat}} \approx 17000$, which was in fact the highest Q observed in optical measurements on a symmetrically coupled structure of the same intrinsic resonator design with $n_{\mathrm{mir}} = 18$ on the same sample. This, along with the Qs measured in the lower-loss samples from Ch. 3, suggest that Q_{rad} is much larger, at least 50,000. Though they do not rule out some small contribution from nonlinear absorption, or electronic multiplication, the curves in Fig. 4-6 indicate that, for reasonable values of Q_{mat}, for a fairly wide range of Q_0, linear absorption on resonance can plausibly explain the QEs observed.

4.1.2 Frequency-response measurements

Preliminary measurements have also been taken to understand the device's operation bandwidth. These measurements are inputing on-resonance light, modulated at frequencies between 10 MHz and 20 GHz, via a microwave synthesizer signal supplied to an $LiNbO_3$ modulator. A bias tee was used to apply a DC bias to the device while filtering its RF output to a microwave spectrum analyzer (MSA), which measured the RF power output by the device as a function of the modulation frequency.

The aggregate frequency response of the optical modulator, as well as the electrical path through the bias tee and internal to the MSA was calibrated by first performing the measurement on a commercial photodiode known to have a flat frequency response out to over 20 GHz (Discovery Semiconductor, model DSC20S; 3 dB bandwidth = 40 GHz). This is shown in Fig. 4-7. The abrupt jump at 3 GHz is due to miscalibration between two modules within the MSA. This data was taken for a low average optical power into the photodetector (2.4 μW), so that the amount of RF power would be comparable to that output by the photonic crystal device.

The frequency response of the diode, for a few different voltages, is shown in Fig. 4-

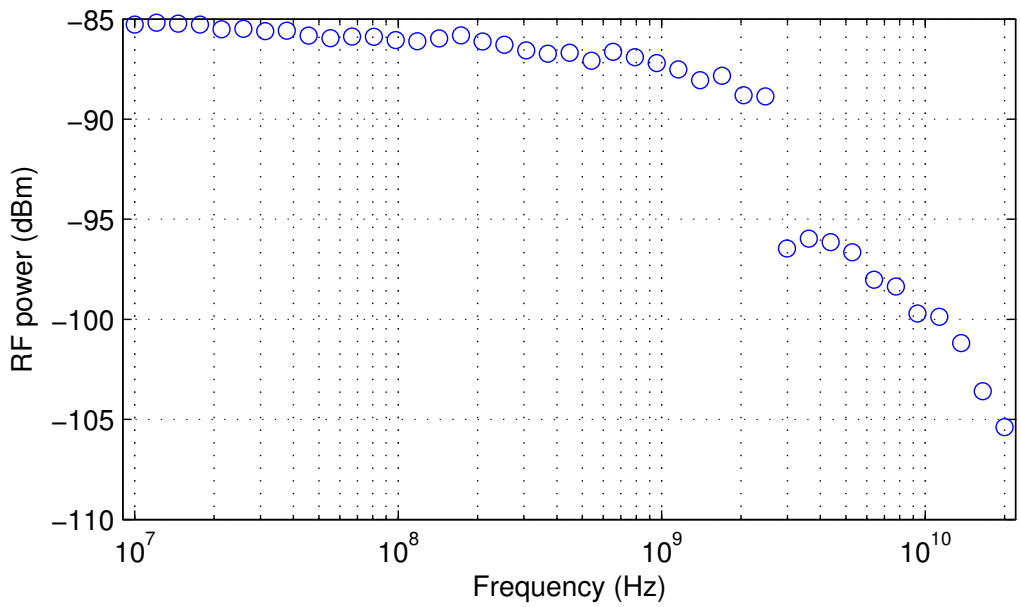

Figure 4-7: Frequency response of 40 GHz-bandwidth photodiode used as a calibration.

8, along with least-squares fits based on a first order filter's frequency response:

$$P_{\text{rec}} = A\left(1 + \frac{f^2}{f_0^2}\right)^{-1}, \tag{4.3}$$

f being the modulation frequency and f_0 being the -3 dB roll-off frequency. The photodiode response exhibits a roll-off at -22V of 360 MHz, though at higher voltages it increases to almost 600 MHz.

In Fig. 4-8, the optical power at -34 V was set to be lower than the 5.8μW used at the previous biases, because the frequency response was observed to abruptly drop off past about 100 MHz at the higher optical power, as shown in Fig. 4-9. This is near the level at which the cavity started to exhibit thermal bistability in the wavelength sweeps, and this drop-off is likely related to the thermal impedance and time constant of the device; i.e., past this frequency, the temperature of the cavity no longer follows the input signal, and the cavity is effectively off-resonance.

A few explanations for the relatively low bandwidth of the device are possible. The transit time across the junction, approximately $t_{\text{tr}} \approx d/v_{\text{dr}}$, where d is the intrinsic region length (2.4 μm in this device) and $v_{\text{dr}} = \phi\mu/d$ is the drift velocity with ϕ

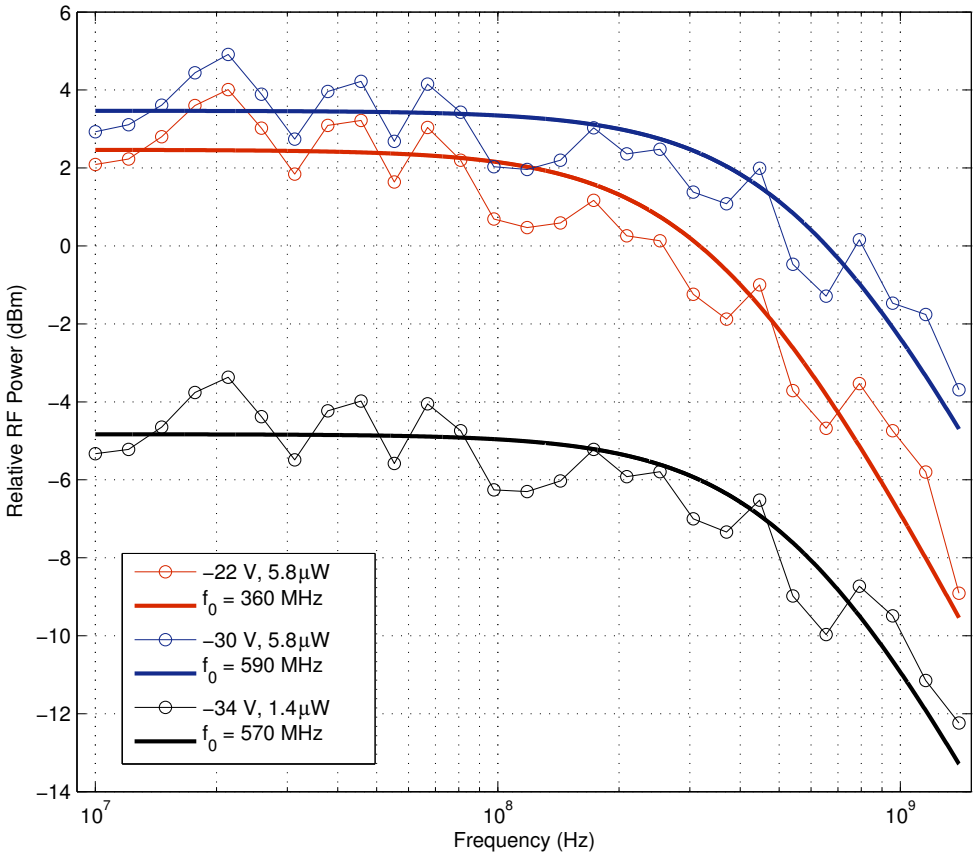

Figure 4-8: Frequency response 1D photonic crystal photodetector (relative to the calibration data shown above), for three different voltages. The -34V data is taken at a lower power to avoid bistability in the cavity (see Fig. 4-9).

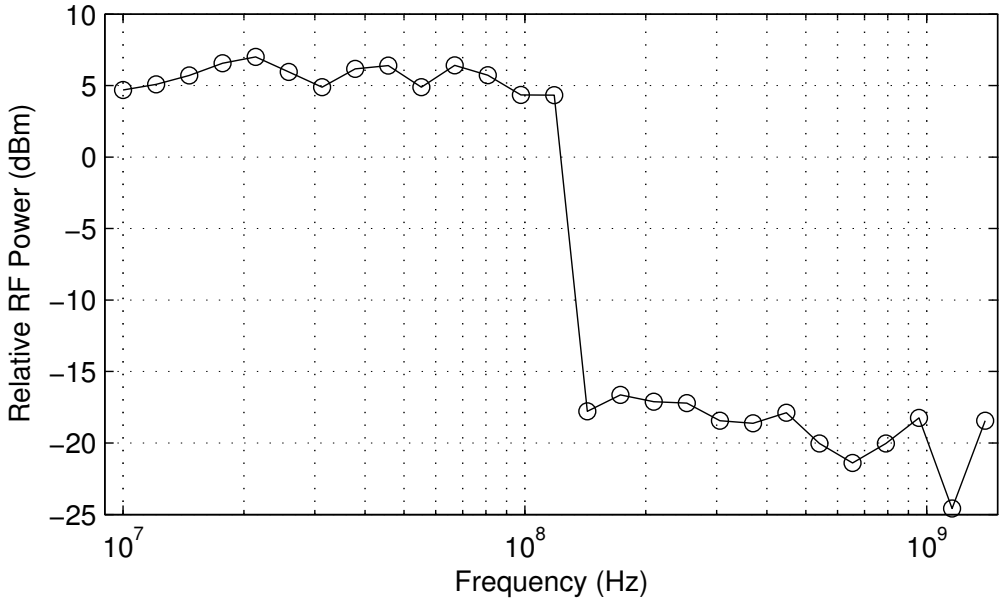

Figure 4-9: Frequency response 1D photonic crystal photodetector (relative to the calibration data shown above) at the same operating point as the black curve in Fig. 4-8, except with 5.8 μW instead of 1.4 μW input to the cavity.

volts applied. The mobility is known to be roughly between 0.2-0.5 that of crystalline silicon, so assuming a mobility of 200 cm^2/Vs, at -10V applied, $t_{\mathrm{tr}}^{-1} = \phi\mu/d^2 \approx 38$ GHz. Transit time is thus unlikely to be the limiting factor.

RC limitations also seem unlikely; differential series resistances of well under 100 kΩ have been observed under forward biases, and a very rough estimate of device capacitance $C = \epsilon_{\mathrm{Si}}A/d \approx 0.01$ fF, resulting in $f_0 = 1/2\pi\mathrm{RC} = 160$ GHz.

The bandwidth seems to thus be related to some defect-state related dynamics; the response to optical power may, for example rely on some slow equilibration of the defect states involved in each absorption event. Further testing and modeling should help illuminate the reason for this limitation.

4.2 Initial 3-hole measurements - D0

As discussed in the previous chapter, the electrical devices made in D0 suffered from fairly large optical loss rates due to the silicon nitride holes and overcladding, and thus showed much lower Qs, a substantial part of which is expected to have been

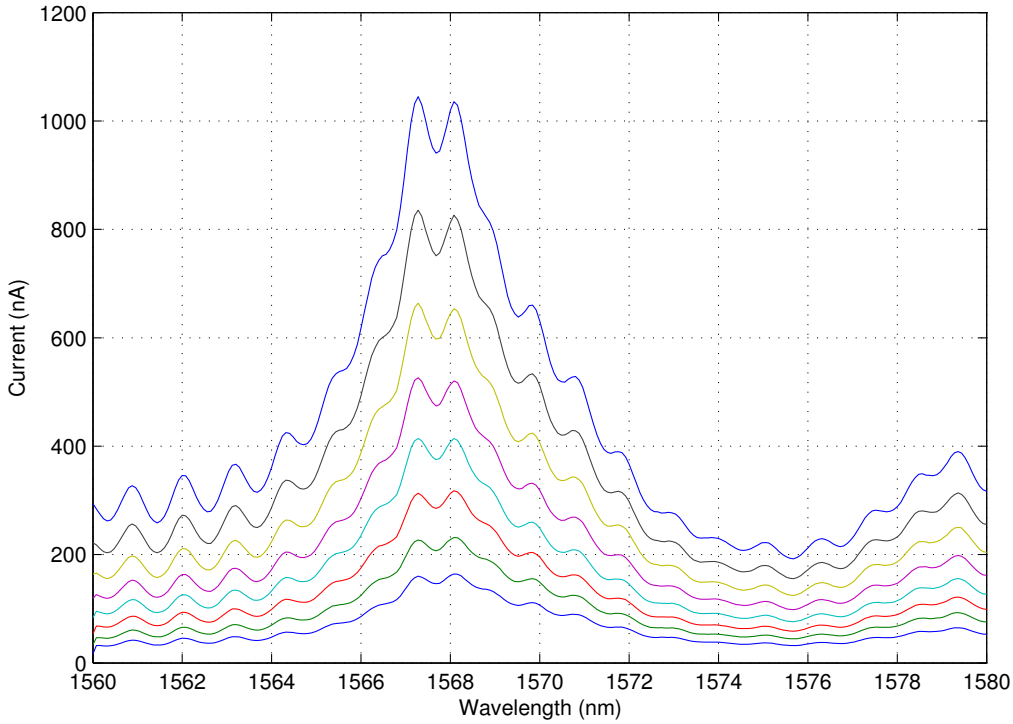

Figure 4-10: Detected current as a function of wavelength for applied voltages increasing in increments of 5 V from 5 to 40 V.

radiative. The intrinsic region in this device was 4.1 μm wide. Fig. 4-10 shows the current measured as a function of wavelength for voltages between -5 and -40 V, for an input power after the coupler between 150-300 μW (the coupling was not independently measured on this chip, resulting in the uncertainty in input power). The resonance did not shift with optical power. At -40 V, the current of about 1 μA corresponds to an efficiency of between 0.3-0.6%.

Fig. 4-11 shows the I-Vs measured on this device; at lower powers, a slight increase in efficiency is observed, to around 0.4-0.8%. in general, though, the much lower quantum efficiencies here (even at -40 V) are likely due predominantly to the fact that the Q is far from being material-loss limited, and most of the power dropped into the cavity never contributes to photocarrier generation.

These low efficiencies discouraged further tests, but did at least show that contacts to the 2D cavities formed correctly in this process.

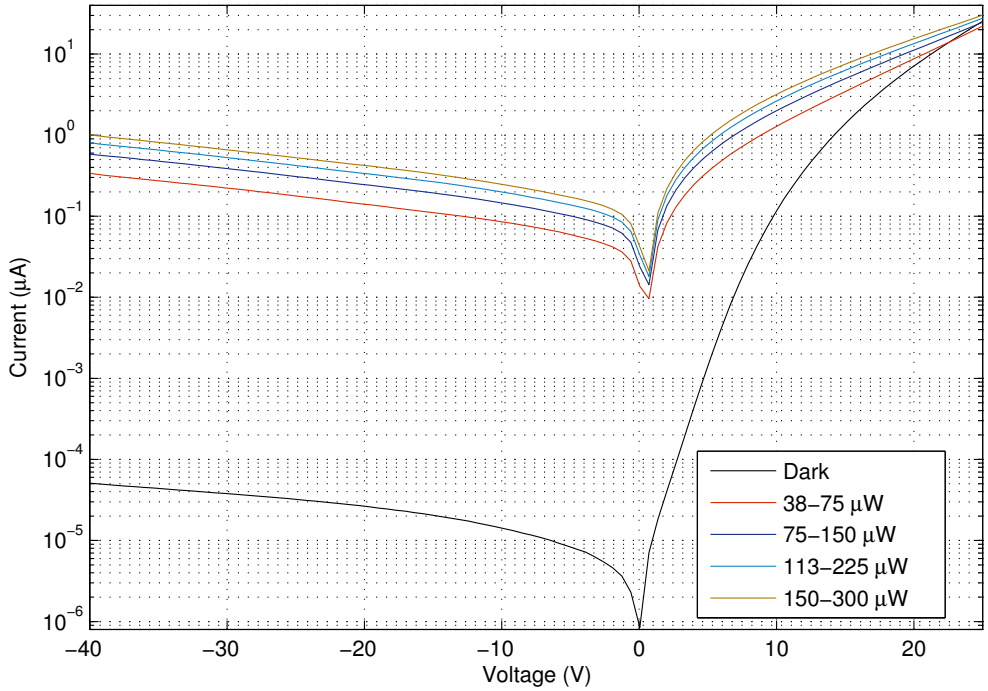

Figure 4-11: IVs for 3-hole cavity junction after full-flow processing with on-resonance light at various powers input to the chip.

4.3 Conclusion, summary

Linear absorption-generated photocarriers proved sufficient to achieve QEs of a few tens of percent in the photonic crystal cavities designed and fabricated (D1S); no increase in efficiency with input power, which would indicate some contribution fro TPA, was observed in the devices studied. The devices are currently limited to bandwidths of only a few hundred megahertz, and since both transit time and RC limitations should be much higher, we suspect this limitation is due to defect state dynamics. For many applications, high QEs at lower biases are also required, and here, contact geometry could play a significant role.

Chapter 5

Future work and conclusion

A number of directions seem worthwhile at the conclusion of this work. This chapter briefly discusses potential directions for improving the characteristics of the detector devices made, more accurate measurements of the TPA in pSi, and potential uses of the Fano effects seen in the 1D photonic crystals in modulator devices.

5.1 Improvements to the detectors

This work has demonstrated high-Q photonic crystal cavities within a commercial DRAM process, and shown that the absorption in the poly (despite the weak loss and short device length) is capable of generating photocurrents corresponding to quantum efficiencies of tens of percent. From the perspective of the practical devices, the most pressing question is how the operating voltage can be decreased to just a few volts, and how the bandwidth can be increased.

Simply understanding why contacts did not form in the 1D resonators with patterned wings is important to ensure future devices with lower radiative loss rates are possible to create and contact. Improvements to the electrical design can certainly help reduce the required biases, which can be reduced by decreasing the size of the intrinsic region. Devices with p+ and n+ regions closer to the cavity center remain to be studied, and the addition of lower concentration implants, to form a p+/p/i/n/n+ structure, should allow for closer electrical contact with minimum additional optical

loss. Some techniques developed for Si modulators could apply here as well; low doping profiles extending into the core and producing vertical junctions, as have been used for depletion-mode modulators [WZT+] would enable significant improvement.

These modifications would reduce the device's series resistance as well, although since RC limitations already do not seem to limit bandwidth this reduction may not increase bandwidth. More experimental work is needed on the current devices to understand possible contributions from defect state dynamics; measurements of temperature, power, and bias-dependence of the bandwidth could reveal much about the particular processes limiting the speed, and potential avenues to improvement by electrical design.

5.2 pSi nonlinearity measurements

As discussed in Ch.2, ultrafast measurements of nonlinear absorption in waveguides overcome many of the challenges faced in the attempts to understand nonlinear absorption in polysilicon in this work [MNK+12]. By allowing clear separation of these two effects, such measurements should allow for conclusive comparison between TPA and FCA in pSi samples vs. crystalline silicon. The waveguide measurements here indicate that β, the the FCA cross section, or both to some degree are likely to be different from crystalline silicon, which would be valuable to understand fully.

5.3 Fano-resonance modulators

The asymmetric lineshapes observed in transmission through the 1D resonators could be interesting to study in greater detail from the perspective of modulator design. For a given resonator Q, such profiles allow for much steeper features in transmission profiles than a simple Lorentzian, allowing a small index change, as achieved through carrier injection or depletion, to induce stronger extinction. This advantage can be significant, especially since a specified bandwidth always limits the usable Q; Fano resonances allow increasing feature steepness without increasing the response time of

the intracavity power.

A few different approaches can be taken to achieving this effect; in our devices, the interference was with the fundamental mode and a higher order waveguide mode, though a similar effect has been proposed and observed with a ring nested in one arm of a Mach-Zehnder interferometer [DLD+]. The use of photonic crystal resonators instead of rings, as well as a second-order mode in the feeding waveguide itself rather than a split-off branch, could be beneficial in eliminating the insertion losses of the splitters required in the latter approach, total device size, as well as resonator volume; the resonator volume is directly related to the required switching energy. The observation of this effect via multi-mode interference in small and electrically tunable structures might enable interesting approaches to high-performance modulators.

The demonstrated ability to fabricate high-Q, wavelength-scale resonators photolithographically in scaled CMOS processes and despite the suboptimal dielectric environments raises questions of how general a building block such resonators can be; even for passive components, such as filter banks, the small size of these resonators could make them advantageous over larger ring resonators as system densities, or layer thicknesses scale.

Bibliography

[AASN03] Y Akahane, T Asano, B Song, and S Noda. High-Q photonic nanocavity in a two-dimensional photonic crystal. *Nature*, January 2003. 21, 59

[AHL+07] Donghwan Ahn, Ching-Yin Hong, Jifeng Liu, Wojciech Giziewicz, Mark Beals, Lionel C Kimerling, Jurgen Michel, Jian Chen, and Franz X Kärtner. High performance, waveguide integrated Ge photodetectors. *Optics Express*, 15(7):3916–3921, April 2007. 24

[AXV10] Solomon Assefa, Fengnian Xia, and Yurii A Vlasov. Reinventing germanium avalanche photodetector for nanophotonic on-chip optical interconnects. *Nature*, 464(7285):80–84, March 2010. 24

[BAIS09] J Bravo-Abad, E P Ippen, and M Soljačić. Ultrafast photodetection in an all-silicon chip enabled by two-photon absorption. *Applied Physics Letters*, 94(24):241103, January 2009. 11, 26, 27

[BCLY63] W L Bond, B G Cohen, R C C Leite, and A Yariv. Observation of the dielectric-waveguide mode of light propagation in p-n junctions. *Applied Physics Letters*, 2(3):57, 1963. 16

[BJHS08] T Baehr-Jones, M Hochberg, and A Scherer. Photodetection in silicon beyond the band edge with surface states. *Optics Express*, 16(3):1659–1668, 2008. 25

[BJK05] J Bradley, P Jessop, and A Knights. Silicon waveguide-integrated optical power monitor with enhanced sensitivity at 1550 nm. *Applied Physics Letters*, January 2005. 25

[BJO+09] Christopher Batten, Ajay Joshi, Jason Orcutt, Anatol Khilo, Benjamin Moss, Charles W Holzwarth, Milos A Popović, Hanqing Li, Henry I Smith, Judy L. Hoyt, Franz X. Kaertner, Rajeev J Ram, Vladimir Stojanović, and Krste Asanovic. Building Many-Core Processor-to-DRAM Networks with Monolithic CMOS Silicon Photonics. *IEEE Micro*, 29(4):8–21, 2009. 17

[BL74] JE Bjorkholm and PF Liao. Resonant enhancement of two-photon absorption in sodium vapor. *Physical Review Letters*, 33(3):128–131, 1974. 38

[BRvD07] AD Bristow, N Rotenberg, and HM van Driel. Two-photon absorption and Kerr coefficients of silicon for 850–2200 nm. *Applied Physics Letters*, 90:191104, 2007. 34

[BSP05] P Barclay, K Srinivasan, and OJ Painter. Nonlinear response of silicon photonic crystal microresonators excited via an integrated waveguide and fiber taper. *Optics Express*, 13(3):801–820, 2005. 54, 93

[CECP09] Jasper Chan, Matt Eichenfield, Ryan Camacho, and Oskar Painter. Optical and mechanical design of a "zipper" photonic crystal optomechanical cavity. *Optics Express*, 17(5):3802–3817, 2009. 60

[CISZ97] A Cutolo, M Iodice, P Spirito, and L Zeni. Silicon electro-optic modulator based on a three terminal device integrated in a low-loss single-mode SOI waveguide. *J. Lightwave Technol*, 15(3):505–518, 1997. 16

[CP10] Hui Chen and Andrew W Poon. Two-photon absorption photocurrent in p-i-n diode embedded silicon microdisk resonators. *Applied Physics Letters*, 96(19):191106, January 2010. 26

[Din03] M Dinu. Dispersion of phonon-assisted nonresonant third-order nonlinearities. *Quantum Electronics, IEEE Journal of*, 39(11):1498–1503, January 2003. 33

[DJK10] J Doylend, P Jessop, and A Knights. Silicon photonic resonator-enhanced defect-mediated photodiode for sub-bandgap detection. *Optics Express*, January 2010. 25

[DLD+] S Darmawan, Y M Landobasa, P Dumon, R Baets, and M K Chin. Nested-Ring Mach-Zehnder Interferometer in Silicon-on-Insulator. *IEEE Photonics Technology Letters*, 20(1):9–11. 105

[DQG03] M Dinu, F Quochi, and H Garcia. Third-order nonlinearities in silicon at telecom wavelengths. *Applied Physics Letters*, 82(18):2954, 2003. 49

[FR59] HY Fan and AK Ramdas. Infrared Absorption and Photoconductivity in Irradiated Silicon. *Journal of Applied Physics*, 30(8):1127–1134, 1959. 25

[GPB+09] M Galli, S L Portalupi, M Belotti, L C Andreani, L O'Faolain, and T F Krauss. Light scattering and Fano resonances in high-Q photonic crystal nanocavities. *Applied Physics Letters*, 94(7):071101, 2009. 59

[GSG+07a] M W Geis, S J Spector, M E Grein, R J Schulein, J U Yoon, D M Lennon, C M Wynn, S T Palmacci, F Gan, F X Käertner, and T M Lyszczarz. All silicon infrared photodiodes: photo response and effects of processing temperature. *Optics Express*, 15(25):16886–16895, December 2007. 25, 95

[GSG+07b] MW Geis, SJ Spector, ME Grein, RT Schulein, JU Yoon, DM Lennon, S Deneault, F Gan, FX Kaertner, and TM Lyszczarz. CMOS-compatible all-Si high-speed waveguide photodiodes with high responsivity in near-infrared communication band. *IEEE Photonics Technology Letters*, 19(3):152–154, 2007. 25

[Hal70] David Hall. Observation of propagation cutoff and its control in thin optical waveguides. *Applied Physics Letters*, 17(3):127, 1970. 16

[Hau84] Hermann Haus. *Waves and Fields in Optoelectronics*. Prentice-Hall, 1984. 29

[HCH+10] L.D Haret, X Checoury, Z Han, P Boucaud, S Combrié, and A De Rossi. All-silicon photonic crystal photoconductor on silicon-on-insulator at telecom wavelength. *Optics Express*, 18(23):23965–23972, 2010. 26

[HYG70] D Hall, A Yariv, and E. Garmire. Optical Guiding and electro-optic modulation in GaAs epitaxial layers. *Optics Communications*, 1(9):403–405, 1970. 16

[ISF07] K Ikeda, Y Shen, and Y Fainman. Enhanced optical nonlinearity in amorphous silicon and its application to waveguide devices. *Optics Express*, 15(26):17761–17771, 2007. 38

[JJB83] WB Jackson, NM Johnson, and DK Biegelsen. Density of gap states of silicon grain boundaries determined by optical absorption. *Applied Physics Letters*, 43(2):195–197, 1983. 35, 37

[KBG06] A Knights, J Bradley, and S Gou. Silicon-on-insulator waveguide photodetector with self-ion-implantation-engineered-enhanced infrared response. *Journal of Vacuum Science and Technology*, January 2006. 25

[KJP+07] C Koos, L Jacome, C Poulton, J Leuthold, and W Freude. Nonlinear silicon-on-insulator waveguides for all-optical signal processing. *Optics Express*, 15(10):5976–5990, 2007. 40

[KLM+09] Yimin Kang, Han-Din Liu, Mike Morse, Mario J Paniccia, Moshe Zadka, Stas Litski, Gadi Sarid, Alexandre Pauchard, Ying-Hao Kuo, Hui-Wen Chen, Wissem Sfar Zaoui, John E Bowers, Andreas Beling, Dion C Mcintosh, Xiaoguang Zheng, and Joe C Campbell. Monolithic germanium/sil-

icon avalanche photodiodes with 340 GHz gain–bandwidth product. *Nature Photonics*, 3(1):59–63, January 2009. 24

[KNM+06] E Kuramochi, Masaya Notomi, S Mitsugi, A Shinya, T Tanabe, and T Watanabe. Ultrahigh-Q photonic crystal nanocavities realized by the local width modulation of a line defect. *Applied Physics Letters*, 88:041112, 2006. 19, 59

[LC00] B.E. Little and S.T. Chu. Toward very large-scale integrated photonics. *Optics and photonics news*, 11(11):24, 2000. 17, 23

[LCH+97] BE Little, ST Chu, HA Haus, J Foresi, and JP Laine. Microring resonator channel dropping filters. *J. Lightwave Technol*, 15(6):998–1005, 1997. 17

[LMG+05] Jifeng Liu, Jurgen Michel, Wojciech Giziewicz, Dong Pan, Kazumi Wada, Douglas D Cannon, Samerkhae Jongthammanurak, David T Danielson, Lionel C Kimerling, Jian Chen, F Ömer Ilday, Franz X Kärtner, and John Yasaitis. High-performance, tensile-strained Ge p-i-n photodetectors on a Si platform. *Applied Physics Letters*, 87(10):103501, 2005. 24

[LPA07] Q Lin, OJ Painter, and GP Agrawal. Nonlinear optical phenomena in silicon waveguides: modeling and applications. *Opt. Express*, 15:16604–16644, 2007. 34, 44

[LT04] T K Liang and H K Tsang. Role of free carriers from two-photon absorption in Raman amplification in silicon-on-insulator waveguides. *Applied Physics Letters*, 84(15):2745, 2004. 93

[MB03] N Moll and G L Bona. Comparison of three-dimensional photonic crystal slab waveguides with two-dimensional photonic crystal waveguides: Efficient butt coupling into these photonic crystal waveguides. *Journal of Applied Physics*, 93(9):4986, 2003. 63

[MFK10] Andrey Miroshnichenko, Sergej Flach, and Yuri Kivshar. Fano resonances in nanoscale structures. *Reviews of Modern Physics*, 82(3):2257–2298, August 2010. 78

[MMV03] S McNab, N Moll, and Y Vlasov. Ultra-low loss photonic integrated circuit with membrane-type photonic crystal waveguides. *Optics Express*, 11(22):2927–2939, 2003. 63

[MNK+12] Ali R Motamedi, Amir H Nejadmalayeri, Anatol Khilo, Franz X Kärtner, and Erich P Ippen. Ultrafast nonlinear optical studies of silicon nanowaveguides. *Optics Express*, 20(4):4085–4101, February 2012. 34, 40, 53, 104

[MOR11] K K Mehta, J S Orcutt, and R J Ram. Enhanced Two-Photon Absorption in Polycrystalline Silicon. *Conference on Lasers and Electro-Optics (CLEO)/Quantum Electronics and Laser Science (QELS)*, 2011. 48

[MT97] Vladimir A Mandelshtam and Howard S Taylor. Harmonic inversion of time signals and its applications. *The Journal of Chemical Physics*, 107(17):6756, 1997. 61

[NKT08a] Masaya Notomi, E Kuramochi, and H Taniyama. Ultrahigh-Q nanocavity with 1D photonic gap. *Optics Express*, January 2008. 19

[NKT08b] Masaya Notomi, Eiichi Kuramochi, and Takasumi Tanabe. Large-scale arrays of ultrahigh-Q coupled nanocavities. *Nature Photonics*, 2(12):741–747, November 2008. 19

[OKH+11] Jason S Orcutt, Anatol Khilo, Charles W Holzwarth, Milos A Popović, Hanqing Li, Jie Sun, Thomas Bonifield, Randy Hollingsworth, Franz X Kärtner, Henry I Smith, Vladimir Stojanović, and Rajeev J Ram. Nanophotonic integration in state-of-the-art CMOS foundries. *Optics Express*, 19(3):2335–2346, January 2011. 17

[OR10] Jason S Orcutt and Rajeev J Ram. Photonic Device Layout Within the Foundry CMOS Design Environment. *IEEE Photonics Technology Letters*, 22(8):544–546, 2010. 17

[ORI+10] Ardavan F. Oskooi, David Roundy, Mihai Ibanescu, Peter Bermel, J. D. Joannopoulos, and Steven G. Johnson. MEEP: A flexible free-software package for electromagnetic simulations by the FDTD method. *Computer Physics Communications*, 181:687–702, January 2010. 61

[OTK+12] Jason S Orcutt, Sanh D Tang, Steve Kramer, Karan Mehta, Hanqing Li, Vladimir Stojanović, and Rajeev J Ram. Low-loss polysilicon waveguides fabricated in an emulated high-volume electronics process. *Optics Express*, 20(7):7243–7254, March 2012. 38

[PLZL11] K Preston, Y.H.D Lee, M Zhang, and M Lipson. Waveguide-integrated telecom-wavelength photodiode in deposited silicon. *Optics Letters*, 36(1):52–54, 2011. 26, 93

[QL11] Qimin Quan and Marko Lončar. Deterministic design of wavelength scale, ultra-high Q photonic crystal nanobeam cavities. *Optics Express*, 19(19):18529–18542, 2011. 61, 71

[SB87] R Soref and B Bennett. Electrooptical effects in silicon. *Quantum Electronics, IEEE Journal of*, 23(1):123–129, 1987. 16

[SBSW04] M Sheik-Bahae, A Said, and T Wei. Sensitive measurement of optical nonlinearities using a single beam. *IEEE Journal of Quantum Electronics*, pages 1–10, April 2004. 48, 50

[Sea85] CH Seager. Grain-Boundaries in Polycrystalline Silicon. *Annual Review of Materials Science*, 15:271–302, 1985. 35

[SL85] R. A. Soref and J. P. Lorenzo. Single-crystal silicon: a new material for 1.3 and 1.6 μm integrated-optical components. *Electronics Letters*, 21(21):26–27, 1985. 16

[SL86] R Soref and J. Larenzo. All-silicon active and passive guided-wave components for 1.3 and 1.6 μm. *Quantum Electronics, IEEE Journal of*, 22(6):873–879, 1986. 16

[Tie71] P K Tien. Light waves in thin films and integrated optics. *Applied Optics*, 10(11):2395–2413, November 1971. 16

[TNK+06] Takasumi Tanabe, Masaya Notomi, Eiichi Kuramochi, Akihiko Shinya, and Hideaki Taniyama. Trapping and delaying photons for one nanosecond in an ultrasmall high-Q photonic-crystal nanocavity. *Nature Photonics*, 1(1):49, December 2006. 59

[TRWR94] CK Tang, GT Reed, AJ Walton, and AG Rickman. Low-Loss, Single-Mode, Optical-Phase Modulator in Simox Material. *J. Lightwave Technol*, 12(8):1394–1400, 1994. 16

[TST+10] Takasumi Tanabe, Hisashi Sumikura, Hideaki Taniyama, Akihiko Shinya, and Masaya Notomi. All-silicon sub-gb/s telecom detector with low dark current and high quantum efficiency on chip. *Applied Physics Letters*, 96(101103), 2010. 11, 26, 27, 53

[VOHM05] Yurii A Vlasov, Martin O'Boyle, Hendrik F Hamann, and Sharee J McNab. Active control of slow light on a chip with photonic crystal waveguides. *Nature*, 438(7064):65–69, November 2005. 23, 81

[WZT+] M.R Watts, W.A Zortman, D.C Trotter, R.W Young, and A.L Lentine. Low-Voltage, Compact, Depletion-Mode, Silicon Mach-Zehnder Modulator. *IEEE Journal of Selected Topics in Quantum Electronics*, 16(1):159–164. 104

[XSPL05] Qianfan Xu, Bradley Schmidt, Sameer Pradhan, and Michal Lipson. Micrometre-scale silicon electro-optic modulator. *Nature*, 435(7040):325, May 2005. 17

[Yar84] A Yariv. The Beginning of Integrated Optoelectronic Circuits. *IEEE Transactions on Electron Devices*, 31(11):1656–1661, 1984. 15

[YN77] A Yariv and M Nakamura. Periodic Structures for Integrated-Optics. *IEEE Journal of Quantum Electronics*, 13(4):233–253, 1977. 17